

AD-A205 191

4

DTIC FILE COPY

EXPERIMENTAL OBSERVATION OF THE
NONLINEAR RESPONSE OF SINGLE BUBBLES
TO AN APPLIED ACOUSTIC FIELD

National Center
for
Physical Acoustics

DTIC
UNCLASSIFIED
DEC 20 1988
S E D



The University
of Mississippi



Institute for
Technology
Development

A joint venture

This document has been approved
for public release and sales in
distribution is unlimited.

88 12 20 088

EXPERIMENTAL OBSERVATION OF THE
NONLINEAR RESPONSE OF SINGLE BUBBLES
TO AN APPLIED ACOUSTIC FIELD

BY

R. GLYNN HOLT
and
LAWRENCE A. CRUM

National Center for Physical Acoustics
University, MS 38677

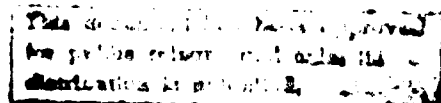
December 1988

Technical Report
prepared for:

Office of Naval Research
Physics Division
Contract # N00014-86-K-0134



NCPA LC.02 1988



UNCLASSIFIED

SECURITY CLASSIFICATION OF THIS PAGE (When Data Entered)

For spherical bubbles, the scattered intensity I as a function of radius R and angle θ is calculated theoretically by solving the boundary value problem (Mie theory) for the water/bubble interface. The inverse transfer function $R(I)$ is obtained by integrating over the solid angle centered at some constant θ . Using $R(I)$ as a look-up table, the radius vs time ($R(t)$) response is calculated from the measured intensity vs time ($I_{exp}(R,t)$). Fourier and phase space analyses are applied to individual $R(t)$ curves. Resonance response curves are also constructed from the $R(t)$ curves for equilibrium radii ranging from 20 to 90 microns, and harmonic resonances are observed. Comparisons are made to a model for bubble oscillations developed by Prosperetti, et al. [A. Prosperetti, L.A. Crum and K. Commander, J. Acoust. Soc. Am. 83, 502 (1988)].

Complex $I_{exp}(t)$ behavior is also measured, with subharmonics and broad-band noise apparent in the Fourier spectra. This behavior is shown to exhibit high (greater than 2) correlation dimension, indicating the presence of more than one degree of freedom in the motion. Possible explanations for this phenomenon are discussed, including shape oscillations and chaos.

Approved For	
By	
Date	
Project/Activity/Notes	
Initials	
A-1	



UNCLASSIFIED

SECURITY CLASSIFICATION OF THIS PAGE (When Data Entered)

EXPERIMENTAL OBSERVATION OF THE NONLINEAR RESPONSE
OF SINGLE BUBBLES TO AN APPLIED ACOUSTIC FIELD

BY

R. GLYNN HOLT
and
LAWRENCE A. CRUM

National Center for Physical Acoustics
University, MS 38677

December 1988

Technical Report
prepared for:

Office of Naval Research
Physics Division
Contract # N00014-86-K-0134

NCPA LC.02 1988

ACKNOWLEDGEMENTS

I wish to express my indebtedness to those individuals and organizations whose direct and indirect contributions have facilitated the successful completion of this work:

To L. A. Crum, for getting me started in Physics, for moral and financial support, for the occasional pep talk, and for the willingness to take a chance on an independent cuss like myself.

To the members of my committee, for their patience and their helpful comments and suggestions.

To the members of the acoustic cavitation group C. Church, B. Fowlkes, F. Gaitan, S. Horsburgh, H. Pumphrey, R. Roy, for many hours of discussions, and for help in every other way.

To former members A. Atchley, K. Commander, and G. Hansen, for helpful discussions.

To W. Lauterborn and his former students A. Cramer, W. Hentschel, J. Holzfuss, U. Parlitz, E. Suchla, and H. Zarschizky, for getting me started in chaos (theory, not personal habits).

To P. Marston, A. Prosperetti, and I. Schwartz, for discussions and suggestions.

To J. Theiler and F. Gaitan, for letting me use their programs.

To S. Horsburgh, for computational support *par excellence*.

To M. Lundien, for assistance in data acquisition.

To M. Gaitan, S. Smith and L. Weddington, for technical support and assistance in preparation of this document.

To the German Academic Exchange Service, the Office of Naval Research, and the American Society for Engineering Education, whose fellowship programs enabled me to get my graduate education.

To the Office of Naval Research, and the National Center for Physical Acoustics, for support of this work.

TABLE OF CONTENTS

	Page
LIST OF FIGURES.....	vi
INTRODUCTION.....	1
CHAPTER	
I. Theory.....	5
A. Bubble oscillations	5
1. Introduction.....	5
2. Radial oscillations.....	7
B. Optical scattering	12
1. Introduction.....	12
2. Mie theory.....	13
3. Calculations.....	16
II. Experiment.....	22
A. Method.....	22
B. Apparatus.....	25
1. Base equipment	25
2. Detection schemes.....	26
a. RCA photodiode/lens combination	26
b. Thorn/EMI photomultiplier tube.....	27
c. Oriol photodiode	29
C. Calibration.....	33
1. Cell pressure.....	33
2. Photodetector current.....	37
D. Procedure.....	42
1. Introduction.....	42
2. I(t) curves	42
3. Response curves	43

CHAPTER	Page
III. Results.....	45
A. Radial motion	45
1. Response curves	45
2. R(t) analysis	54
a. Graphical representation	54
b. Radial oscillations.....	54
B. Complex motion.....	70
1. Introduction.....	70
2. Fourier analysis.....	71
3. Phase space analysis.....	76
IV. Discussion	94
REFERENCES	103

LIST OF FIGURES

1.	Theoretical resonance curves	10
2.	Theoretical scattered intensity vs. scattering angle	17
3.	Theoretical scattered intensity vs. radius at $\theta = 66^\circ$	18
4.	Theoretical scattered intensity vs. radius at $\theta = 70^\circ$	19
5.	Theoretical scattered intensity vs. radius at $\theta = 80^\circ$	20
6.	Generalized schematic of experiment	24
7.	Solid angle integration of theoretical scattered intensity vs. radius at $\theta = 70^\circ$.	28
8.	Solid angle integration of theoretical scattered intensity vs. radius at $\theta = 66^\circ$ plus calibration data	30
9.	Solid angle integration of theoretical scattered intensity vs. radius at $\theta = 80^\circ$.	32
10.	Photodiode calibration	40
11.	Calibration data including nonlinear bubble oscillations	41
12.	Experimental resonance data for pressures $P = 0.14, 0.20,$ and 0.24 atm. . . .	46
13.	Resonance data for pressure $P = 0.12$	47
14.	Resonance data for pressure $P = 0.13$	48
15.	Resonance data for pressure $P = 0.14$	49
16.	Resonance data for pressure $P = 0.15$	50
17.	Resonance data for pressure $P = 0.20$	51
18.	Resonance data for pressure $P = 0.21$	52
19.	Resonance data for pressure $P = 0.24$	53
20.	Experimental $R(t)$ analysis, $R_0 = 51.5 \mu\text{m}$	56
21.	Experimental $R(t)$ analysis, $R_0 = 61 \mu\text{m}$	57

22.	Experimental $R(t)$ analysis, $R_0 = 64.2 \mu\text{m}$	58
23.	Experimental $R(t)$ analysis, $R_0 = 70 \mu\text{m}$	59
24.	Experimental $R(t)$ analysis, $R_0 = 89 \mu\text{m}$	60
25.	Theoretical $R(t)$ analysis, $R_0 = 51.5 \mu\text{m}$	62
26.	Theoretical $R(t)$ analysis, $R_0 = 61 \mu\text{m}$	63
27.	Theoretical $R(t)$ analysis, $R_0 = 64.2 \mu\text{m}$	64
28.	Theoretical $R(t)$ analysis, $R_0 = 70 \mu\text{m}$	65
29.	Theoretical $R(t)$ analysis, $R_0 = 89 \mu\text{m}$	66
30.	Experimental subharmonic $R(t)$ response, $R_0 = 88.5 \mu\text{m}$	67
31.	Experimental subharmonic $R(t)$ response, $R_0 = 87.5 \mu\text{m}$	68
32.	Period-2 intensity vs. time, $R_0 = 70 \mu\text{m}$	72
33.	Period-4 intensity vs. time, $R_0 = 80 \mu\text{m}$	73
34.	Period-16 intensity vs. time, $R_0 = 80 \mu\text{m}$	74
35.	Complex $I(t)$ response, $R_0 = 90 \mu\text{m}$	75
36.	Complex $I(t)$ response, $R_0 = 90 \mu\text{m}$	77
37.	Phase space analysis for $I(t)$ in Fig. 36.....	78
38.	Correlation integral vs. cube edge length for data in Fig. 36.....	82
39.	Expansion of scaling region in Fig. 38.....	83
40.	Correlation dimension vs. embedding dimension from Fig. 39.....	84
41.	Complex $I(t)$ response, $R_0 = 90 \mu\text{m}$	85
42.	Phase space analysis for $I(t)$ in Fig. 41.....	86
43.	Correlation integral vs. cube edge length for data in Fig. 41.....	87
44.	Complex $I(t)$ response, $R_0 = 90 \mu\text{m}$	88
45.	Correlation integral vs. cube edge length for data in Fig. 44.....	89

46. Complex $I(t)$ response exhibiting intermittency, $R_0 = 90\mu\text{m}$	91
47. Blow-up of region A in Fig. 46.....	92
48. Blow-up of region B in Fig. 46.....	93

INTRODUCTION

Cavitation bubbles in liquids have been of interest to scientists since 1754, when Leonhard Euler [1] first suggested the possibility of cavitation in connection with his study of turbine theory. With the recognition of cavitation as the chief mechanism of erosion damage in ship propellers, turbines, pumps and other hydraulic machinery in the early 1900's came an increase in both experimental and theoretical studies of the phenomenon. Perhaps the first significant theoretical work dealing with the dynamics of bubbles was that of Lord Rayleigh [2] in 1917 describing the collapse of a spherical cavity.

Beginning in the 1950's, the response of such bubbles to applied acoustic fields was the subject of much theoretical work. Papers by Hsieh [3], Plesset [4], Noltingk and Neppiras [5,6], Poritsky [7], and Hickling [8] greatly advanced the theory, resulting in a description of the radius of a bubble as a function of time involving a single, second-order nonlinear differential equation. A more refined treatment of the problem [9] has led to still more complicated expressions involving partial differential equations describing the internal pressure and temperature of the bubble coupled to the radial equation of motion. However, the most important variable (upon which most of the observable effects of cavitation depend) remains the radius as a function of time. There is a plethora of numerically generated radius vs. time ($R(t)$) curves from different models, but, until now, there has been no direct experimental verification of any of these predictions for single, stably oscillating bubbles.

There are a number of other groups whose interest in bubble dynamics is increasing. These include: ship wake researchers [10], who study the persistence of bubbles in wakes and their passive and active contributions to underwater sound propagation; ocean ambient noise researchers [11], who have recently presented evidence of the significant role of oscillating bubbles as an ambient noise source; and biomedical researchers [12,23], who are currently debating the possible side-effects (both harmful and helpful) of acoustic cavitation in the use of diagnostic and therapeutic ultrasound. Each of the phenomena studied by these researchers depends directly on the response of a bubble to an applied pressure; i.e., the $R(t)$ curve for the particular driving pressure.

A third community sharing an interest is the nonlinear dynamics community [13,14], which includes mathematicians, physicists, economists, biologists, engineers, and others. They share a basic interest in the time-evolution of nonlinear systems, and the wide variety of (sometimes unexpected) responses exhibited by driven, dissipative systems, whose time-evolution can be modeled by ordinary (ODE's) and partial (PDE's) differential equations. Most of the research in the field is theoretical and numerical, and relatively few experimental systems have been found to verify the predictions of chaotic responses which are elicited from the computer. A pressure-forced bubble is a highly nonlinear system, and there are numerical and analytical results for some bubble models which exhibit the universal features of nonlinear dynamical systems [18,29-32]. There are also some experimental results indicating chaotic behavior for cavitation bubble fields [30,33], but none for single bubbles.

Thus, the motivation for this study was the need to experimentally produce the radial response of a single bubble to an applied acoustic field. This has been done, and the focus of this dissertation will be the experimental method employed to accomplish the task.

Along the way, however, I observed what I call "complex" bubble motion, which may not necessarily be radial in nature, and may well have one or more chaotic components. Although the scattering method breaks down in terms of providing a direct relationship between the scattered intensity and the radius, the intensity $I(t)$ still contains, in principle, all the dynamical information about the bubble's motion. Thus, some results are presented which exceed the reach of current bubble dynamics models, and provide a stimulus for further research.

Chapter I contains the theoretical aspects of the problem. Part A introduces (without derivation) theoretical models for radial bubble oscillations. Numerical results are presented for comparison with the experimental results presented in Chapter III. Part B describes the theory of optical scattering from a dielectric sphere for the relevant size parameter (ka) range, usually known as Mie scattering [15]. Numerical results for the scattered intensity as a function of both the scattering angle and the radius of the scattering bubble are presented.

Chapter II contains the details of the experiment. Part A describes the general method used, independent of specific apparatus. Part B describes the particular apparatus used in each phase of the experiment. Part C describes the methods of calibrating (1) the pressure in the center of the cylindrical transducer cell, and (2) the output current of (and hence the scattered light intensity incident on) the photodetector. Calibration data are presented for the pressure in the cell and the scattered light intensity. Part D describes the experimental procedure followed in order to obtain $I(t)$ curves and response curves as a function of equilibrium bubble radius.

Chapter III contains the results. Part A presents the results for purely radial motion, containing both $R(t)$ curves and response curves over a range of equilibrium radii.

Part B details complex bubble motion, and describes some of the methods of analysis used for such cases.

Chapter IV concludes the dissertation with a discussion of the results, their validity, and a comparison with numerical results for the equations presented in Chapter I. Ideas for further work, both experimental and theoretical, are also presented.

Chapter I

Theory

A. Bubble oscillations

1. Introduction

It may be argued that the ultimate aim of any theoretical treatment of acoustic cavitation is the attainment of an equation of motion describing the oscillations of the cavity volume, or, more specifically, the motion of the gas/liquid interface. The general problem is to find the pressure and velocity fields of the two phase medium. The starting point for any such undertaking must be the solution of the conservation equations for mass, momentum and energy, subject to suitable boundary conditions at the bubble interface.

For the most general case when no symmetry is invoked, the problem can be almost intractable in terms of obtaining any useful information about the motion. An excellent treatment of this more general problem can be found in Hsieh's 1965 work [3], and the interested reader is referred to his paper for more details.

The imposition of spherical symmetry reduces the complexity of the problem somewhat. Although this is the next logical step, it is not typically the next step in theoretical studies, since it includes shape oscillations of all sorts. What is normally done is to obtain an equation of motion for a purely spherical interface, and then express the

solution as a superposition of spherical harmonics. For details of the stability analysis, see [34-36]. If the driving pressure field is isotropic over the length scale associated with the bubble, then surface modes can only be excited parametrically, and hence should only appear as a threshold dependent quantity. Eller and Crum [37] give an interesting treatment of the threshold calculation for different modes in the pressure-radius plane, and also present data for the onset of "dancing" motion of single bubbles. Perhaps the most important information for the purposes of this study is the presence of a very low (0.05 atm) theoretical pressure threshold for the existence of shape oscillations for bubbles with $R_0 = 75 \mu\text{m}$ and driving frequency $f = 26 \text{ kHz}$ [37-39]. The frequency of this shape oscillation is $f/2$. The implications of this behavior as regards the appearance of subharmonics in the Fourier spectra and the phase space will be discussed later.

Finally, if one requires the shape of the interface to remain purely spherical, one can then obtain a single, second-order, nonlinear ordinary differential equation describing the motion of the bubble wall, with the radius R as the dependent variable and time t as the independent variable. The crux of the problem then becomes that of determining the internal pressure p of the gas inside the bubble, which is a function of both R and t .

There are two ways of dealing with the internal pressure. The first and most widely used [5,6,16-22] method is the polytropic relation,

$$p = p_0 \left(\frac{R_0}{R} \right)^{3\kappa} \quad (1)$$

where p is the pressure of the gas in the bubble, R is the radius, κ is the polytropic index, and the subscript zero refers to equilibrium values. The index κ can range from 1 (isothermal oscillations) to the ratio of specific heats γ (adiabatic oscillations).

There are a few problems associated with the use of the approximation (1). First, appropriate criteria governing the proper value of κ exist only for small-amplitude, linear oscillations [24,25]. Second, for nonlinear oscillations, it is shown in an *ad hoc* fashion [26] that κ itself must vary nonlinearly. Third, the integral over a cycle of $p dv$ vanishes, resulting in no net energy loss associated with the heating and cooling of the gas [9]. Since thermal damping has been shown to be the dominant form of dissipation for a wide range of equilibrium radii and frequencies [21], this is, as it were, the third strike for (1). Attempts to incorporate an effective thermal damping coefficient into the viscosity term to remedy the situation [21] have met with only limited success.

The second method of modeling the internal pressure consists of applying the conservation laws to the interior of the bubble. This has been done by Flynn [27], Hickling [28], and Prosperetti *et al.* [9] in different fashions. For comparison with the radial results presented here, the formulation of Prosperetti *et al.* is used.

I. A. 2. Radial oscillations

For a detailed derivation and description of the equations of motion, along with some numerical results, the interested reader is referred to [9]. For the motion of the bubble wall, Prosperetti *et al.* use an equation of motion originally derived by Keller [20]:

$$\left(1 - \frac{R}{c}\right) R \ddot{R} + \frac{3}{2} \dot{R}^2 \left(1 - \frac{R}{3c}\right) = \left(1 + \frac{R}{c}\right) \frac{1}{\rho_L} \left[p_g(t) - p_f \left(1 + \frac{R}{c}\right) - p_\infty \right] + \frac{R}{\rho_L c} \frac{dp_g(t)}{dt} \quad (2)$$

where R is the radius of the bubble, c is the speed of sound in the liquid, ρ_L is the density of the liquid, and p_S is the time-varying driving pressure. Dots denote time derivatives. The liquid pressure outside the bubble, $p_B(t)$, is related to the internal bubble pressure $p(t)$ by

$$p(t) = p_B(R, t) + \frac{2\sigma}{R} + \frac{4\mu_L \dot{R}}{R} \quad (3)$$

where μ_L is the viscosity of the liquid, and σ is the surface tension of the liquid.

To describe the pressure of the gas inside the bubble as a function of time, one has

$$\dot{p} = \left[\frac{3}{R} (\gamma - 1) K \frac{\partial T}{\partial r} \Big|_{r=R} - \gamma p \dot{R} \right] \quad (4)$$

where γ is the ratio of specific heats of the gas (assumed perfect) inside the bubble, K is the thermal conductivity of the gas, T is the temperature, and the expression is evaluated at $r = R$.

The conservation of energy is expressed by

$$\frac{\partial \tau}{\partial t} + \frac{\gamma - 1}{\gamma p R^2} \left(\frac{\partial \tau}{\partial y} - \frac{\partial \tau}{\partial y} \Big|_{y=1} \right) - \gamma \left(\frac{\partial \tau}{\partial y} - Dp \right) = \frac{D}{R^2} \nabla^2 \tau \quad (5)$$

where the variable τ is defined by

$$\tau = \int_{T_\infty}^T K(\theta) d\theta \quad (6)$$

and a moving boundary is used by defining $y = r/R(t)$. The Laplacian is taken with respect to the variable y , and the thermal diffusivity D for a perfect gas is given by

$$D(p,T) = \frac{K(T)}{C_p \rho(p,T)} = \frac{\gamma - 1}{\gamma} \frac{K(T)T}{P} \quad (7)$$

Of the major assumptions used to derive these equations [9], two seem especially important: (a) The pressure is spatially uniform inside the bubble; (b) There is no mass diffusion across the bubble wall.

The first assumption requires the Mach number of the bubble wall (calculated with respect to the speed of sound in the gas) to be small. Care must be taken when calculating violent collapse cases which occur in some subharmonic oscillations and transient events. This can become complicated, since the heating of the gas during the collapse changes the speed of sound in the gas. The second assumption is only a problem if one is interested in time scales much greater than the typical oscillatory period of a bubble, such as would be needed to study chaotic oscillations [14,29-31].

Using a program written by Gaitan [41] following the methods outlined in [9], I have obtained numerical results for comparison with the data in chapter III. As an overview of the expected response of bubbles driven at different pressures as a function of their equilibrium radius, Fig. 1 plots a family of theoretical resonance curves for pressures 0.03, 0.05, ... up to 0.37 atmospheres, with a driving frequency f of 24.4 kHz. In addition to the main resonance expected for linear oscillators, there are also peaks at $R_0/R_{res} = 0.5$ and 0.33, corresponding to harmonic resonances with frequencies of $2f$ and $3f$, respectively. R_{res} is defined in this case as the equilibrium radius of a bubble whose linear

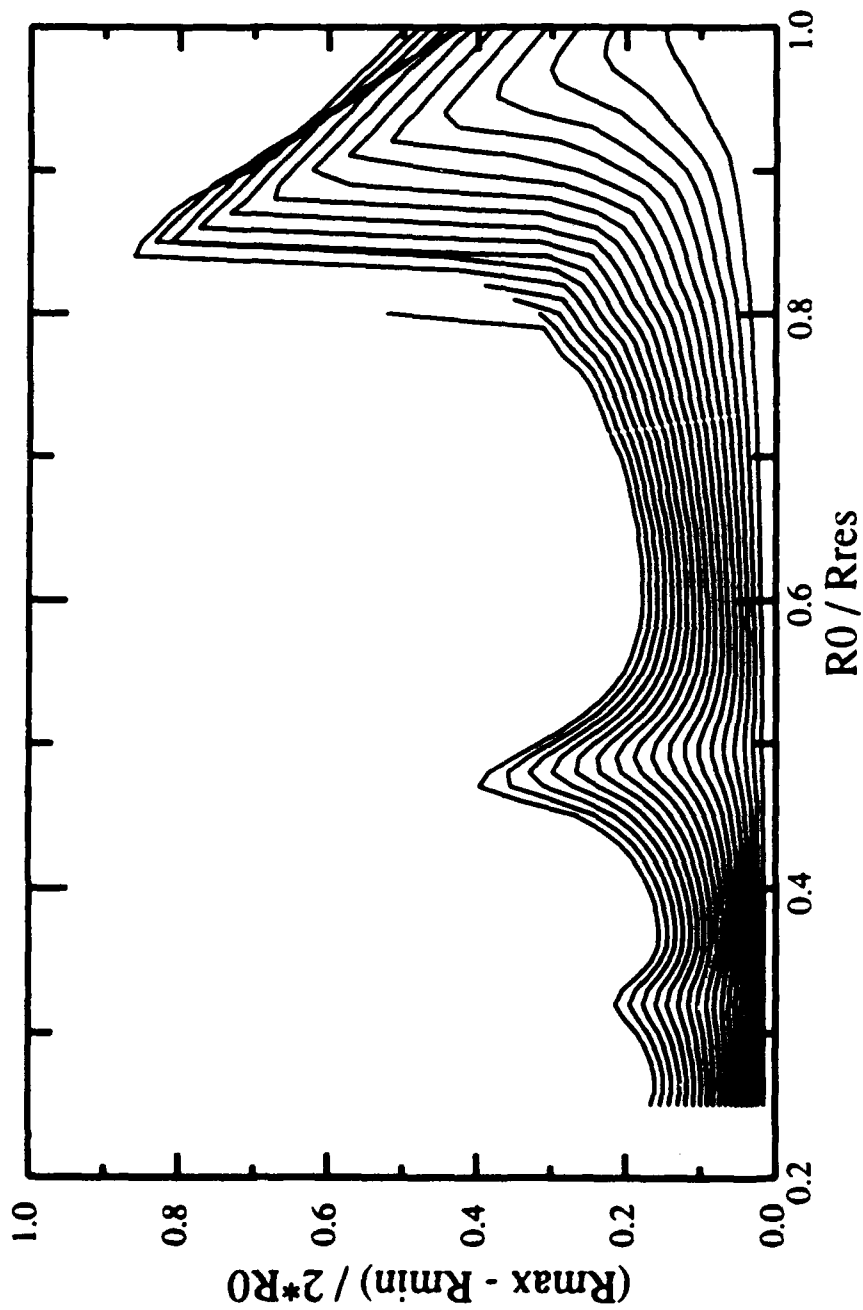


FIGURE 1

Theoretical resonance curves for $P = 0.03, 0.05, \dots, 0.33$ atm, obtained by numerically integrating the equations (2), (4) and (5). $f = 24.4$ kHz.

resonance frequency f_0 equals the driving frequency f . Also apparent is a bending of the peaks towards lower values of R_0/R_{res} , typical of a "softening" nonlinearity. A final feature of this figure is the appearance at sufficiently high (> 0.15 atm.) pressures of a discontinuity in the main resonance curve. The resonance peak has doubled over, so that for a given value R_0/R_{res} in this region, the solution will be triple-valued, with the middle value corresponding to an asymptotically unstable oscillation. Which solution one attains depends on the initial conditions. For sufficiently high pressures, each resonance peak will show this hysteresis phenomenon. This has important implications for attempts to measure such a family of curves, for it implies different results depending on which direction R_0/R_{res} is varied if the pressure is sufficiently high. In Chapter III, experimental resonance curves are presented for different pressures and compared to these numerically generated curves.

Equations (2), (4), and (5) are solved numerically in [9], and some typical oscillatory solutions are presented for the particular numerical implementation outlined in the appendix of [9]. Recently, Kamath and Prosperetti have introduced a more time-efficient and stable method for solving the system [40] utilizing a spectral technique. Initial results indicate that this method could be more useful for long-time integrations. In addition, Fowlkes has recently incorporated rectified diffusion into the equations (2), (4), and (5) [87], using a method proposed by Eller and Flynn [95]. This method was also incorporated into Flynn's bubble model [27] by Church [88]. These developments should greatly aid the attempts to model the (possibly chaotic) large-amplitude oscillations for large driving pressures and long times.

Radius-time curves have also been numerically generated with parameters specific to particular data sets, and they are presented in chapter III for comparison with the data.

I. B. Optical Scattering

1. Introduction

Optical scattering of one form or another has been the only successful technique for obtaining experimentally the time-varying size of a bubble in a liquid. In the past, however, this approach has been limited to high-speed photography [42,43], holography and holo-cinematography [44-49] by Lauterborn *et al.*, with no work done on single periodically-driven gas bubbles, but rather on transient cavities or bubble fields. An interesting light-transmission experiment on a bubble field was also performed [57], eliciting, however, only the spectral characteristics of the motion.

Recently, Hansen [50] used laser scattering on single, stably oscillating bubbles as a means of sizing such bubbles. His work, along with some work by Marston [51,52], suggested the possibility of using laser scattering to observe the time-dependent behavior of a bubble. This section presents the theoretical aspects of the scattering of monochromatic, linearly polarized plane light-waves incident on a spherical gas bubble in a liquid. The numerical technique used to solve for the scattering amplitudes, and some numerical results for relevant cases are also presented.

The question of scattering in the presence of shape oscillations is not theoretically treated, largely because of the lack of any comprehensive treatment of the problem of optical scattering from a dynamically oscillating shape. Arnott and Marston [89] have looked at time-averaged backscattering to ascertain spherical asymmetry (oblateness) in freely rising bubbles, but the method is not suitable for instantaneous observation. In practice, the scattered intensity, even at a single angle, will be dynamically modulated by

the shape oscillations. Model-independent analyses should thus be expected to yield some information, and the results of applying such methods are presented in chapter III.

I. B. 2. Mie theory

The problem at hand is determining the scattered intensity as a function of spatial coordinates for the case of plane, monochromatic, linearly polarized light waves incident on a dielectric sphere. An excellent textbook treatment of the problem is given in Kerker [53], chapters 3-5, and I will use his notation in this section. No derivation of the scattering amplitudes will be given here. For a complete derivation beginning with Maxwell's equations, see [54].

If one defines the scattering plane ($\phi = 0$ plane) as that plane containing the incident ($\theta = 0$) direction and the direction of the scattered wave vector, then the scattered intensity is given by

$$I_{\theta} = \frac{\lambda^2}{4\pi^2 r^2} |S_2|^2 \cos^2 \phi \quad (8)$$

$$I_{\phi} = \frac{\lambda^2}{4\pi^2 r^2} |S_1|^2 \sin^2 \phi \quad (9)$$

where I_{θ} is the component of the scattered intensity parallel to the scattering plane, I_{ϕ} is the component perpendicular to the scattering plane, r is the distance from the bubble center ($r \gg R$), ϕ is the azimuthal angle, and λ is the wavelength of the light in the surrounding medium. The scattering amplitudes S_1 and S_2 are given by

$$S_1 = \sum_{n=1}^{\infty} \frac{2n+1}{n(n+1)} \left[a_n \pi_n(\cos\theta) + b_n \tau_n(\cos\theta) \right] \quad (10)$$

$$S_2 = \sum_{n=1}^{\infty} \frac{2n+1}{n(n+1)} \left[a_n \tau_n(\cos\theta) + b_n \pi_n(\cos\theta) \right] \quad (11)$$

where θ is the scattering angle, and forward scattering corresponds to $\theta = 0$. The angular functions are given by

$$\pi_n(\cos\theta) = \frac{P_n^{(1)}(\cos\theta)}{\sin\theta} \quad (12)$$

$$\tau_n(\cos\theta) = \frac{dP_n^{(1)}(\cos\theta)}{d\theta} \quad (13)$$

and the $P_n^{(1)}(\cos\theta)$ are the associated Legendre functions. The coefficients a_n and b_n are found from

$$a_n = \frac{\psi_n(\alpha)\psi_n(\beta) - m\psi_n(\beta)\psi_n(\alpha)}{\zeta_n(\alpha)\psi_n(\beta) - m\psi_n(\beta)\zeta_n(\alpha)} \quad (14)$$

$$b_n = \frac{m\psi_n(\alpha)\psi_n(\beta) - \psi_n(\beta)\psi_n(\alpha)}{m\zeta_n(\alpha)\psi_n(\beta) - \psi_n(\beta)\zeta_n(\alpha)} \quad (15)$$

where $m = k_1/k_2 = m_1/m_2$ is the relative index of refraction. Subscript 1 refers to the bubble interior, while subscript 2 refers to the medium surrounding the bubble, k is the wave number, m_1 and m_2 are the indices of refraction, $\alpha = 2\pi m_2 R/\lambda_0$ is the size

parameter, λ_0 is the wavelength of the incident light in vacuum, $\beta = \alpha m$, and primes denote differentiation with respect to arguments. The functions

$$\psi_n(\alpha) = \alpha j_n'(\alpha), \quad (16)$$

$$\zeta_n(\alpha) = \alpha h_n^{(2)}(\alpha), \quad (17)$$

are the Riccati-Bessel functions with $j_n(\alpha)$ and $h_n^{(2)}(\alpha)$ the ordinary spherical Bessel functions of the first and third kind, respectively.

For comparison with the current experiment, the incident beam is now restricted to being polarized with the electric field vector parallel to the $\phi = 0$ plane, thus restricting interest to I_θ . Further, the relative intensity I_{rel} is defined as

$$I_{rel} = \frac{4\pi^2 r^2 I_\theta}{\lambda^2} = |S_2|^2 \cos^2 \phi \quad (18)$$

For the rest of the paper, the calculations refer to $n_1 = 1.00$, $n_2 = 1.33$, and $m = 0.75$, these being the relevant parameters for an air bubble in water. λ_0 will be either the red He-Ne line (632.8 nm), or the green Ar-I line (488.0 nm), depending primarily on the chronology of the data set.

I. B. 3. Calculations

Numerical calculations to obtain I_{rel} were carried out using a modification of a program developed by Wiscombe [55]. Several checks of the numerical accuracy were made against results found in [50-53,56]. All of the theoretical results were obtained on a DEC Microvax II running in single precision Fortran. Typical run times ranged from 30 minutes for an I_{rel} vs θ curve to 15 hours for a solid-angle integration calculating $\iint I_{rel} d\theta d\phi$ vs R .

Figure 2 is a plot of I_{rel} vs θ for 0 to 180 degrees for a size parameter of 661, corresponding to a bubble of radius 50 μm for $\lambda_0 = 632.8$ nm, and 38 μm for $\lambda_0 = 488.0$ nm. It is not immediately obvious from this graph where the optimal angular location, in terms of maximum intensity and minimum diffraction structure, for a photodetector should lie, if indeed there is an optimal choice. It is at least clear that one would like to be at some $\theta < 90$ degrees, since the intensity drops an order of magnitude from 70 to 100.

Figures 3 and 4 show I_{rel} vs R for $\theta = 66$ and 70 degrees respectively, for $\lambda_0 = 632.8$ nm. These angles were chosen corresponding to the locations for various photodetector combinations used in the experiments. At face value, neither of these is very desirable as a transfer function, since the inverse transfer function $R(I)$ is multiple-valued. On the suggestion of Marston [58], and following the example of Hansen [54], calculations were made at $\theta = 80$ degrees, close to the critical angle [56]. Fig. 5 shows I_{rel} vs R for $\theta = 80^\circ$, with $\lambda_0 = 488.0$ nm. Ignoring fine structure, the intensity rises regularly with increasing radius, and $R(I)$ is single-valued.

The general form of Figs. 3-5 is explicable in terms of the physical optics approximations in [51,56]. The coarse structure in Figs. 3 and 4 is due mainly to the

Relative Intensity

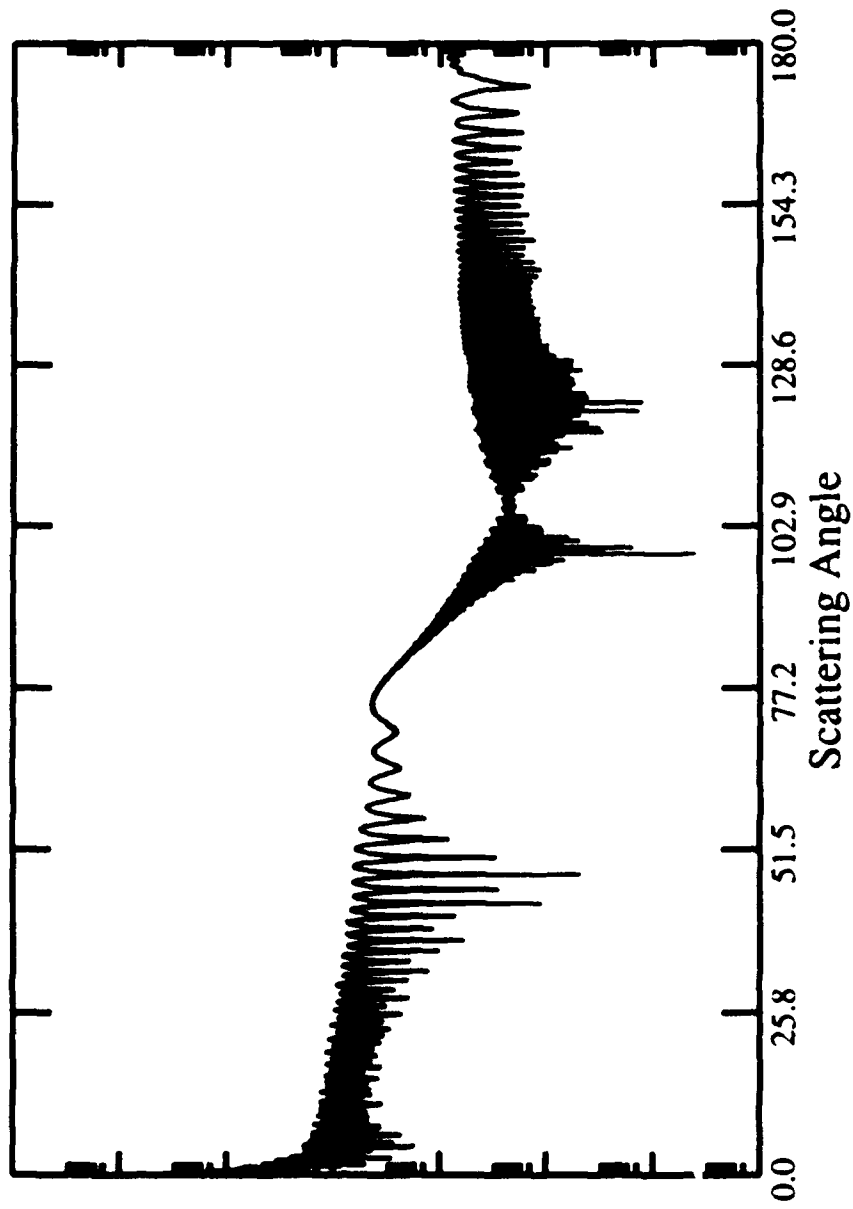


FIGURE 2

Theoretical scattered intensity as a function of scattering angle (0 is forward) for a size parameter of 661 . This corresponds to a radius of 50 microns with respect to an incident He-Ne beam (632.8 nm in the bubble), or 38.6 microns with respect to the Ar-I 488.0 nm line. Only the parallel polarized component S_2 is shown.

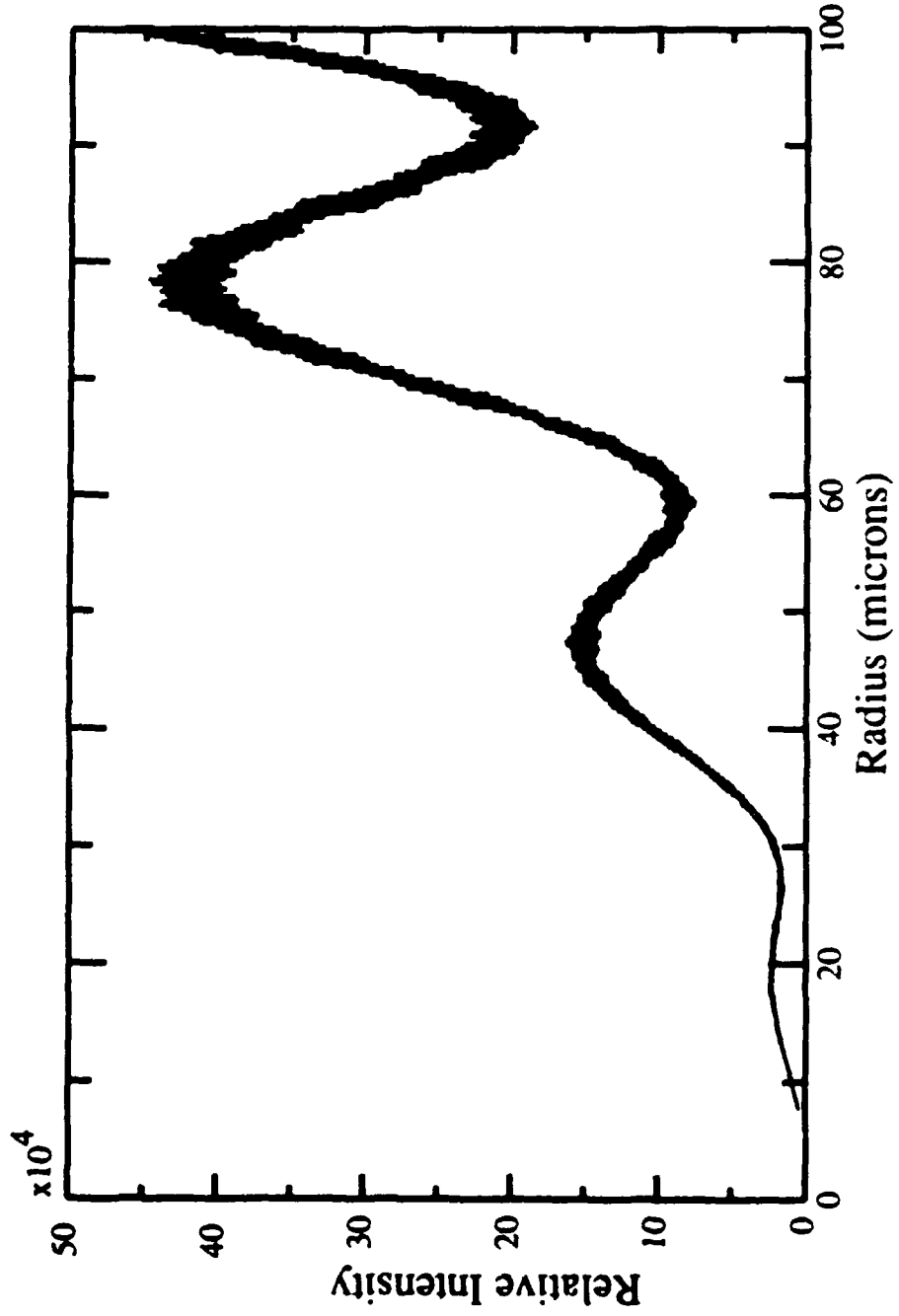


FIGURE 3

Theoretical scattered intensity at 66 degrees for the He-Ne 632.8 line. Only the component S2 is shown, corresponding to polarization of the incident beam parallel to the scattering plane.

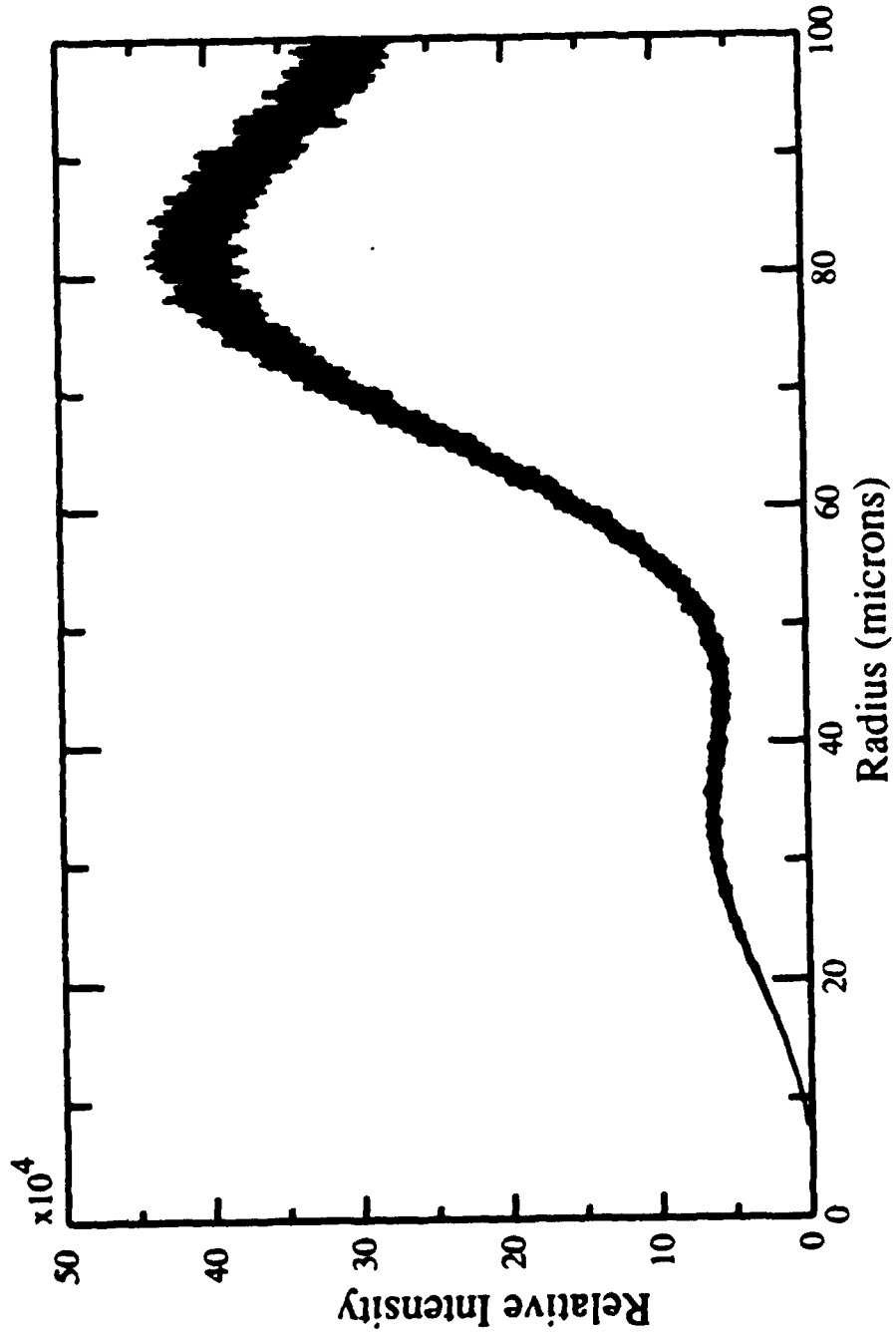


FIGURE 4

Theoretical scattered intensity at 70 degrees for the He-Ne 632.8 line. Only the component S2 is shown, corresponding to polarization of the incident beam parallel to the scattering plane.

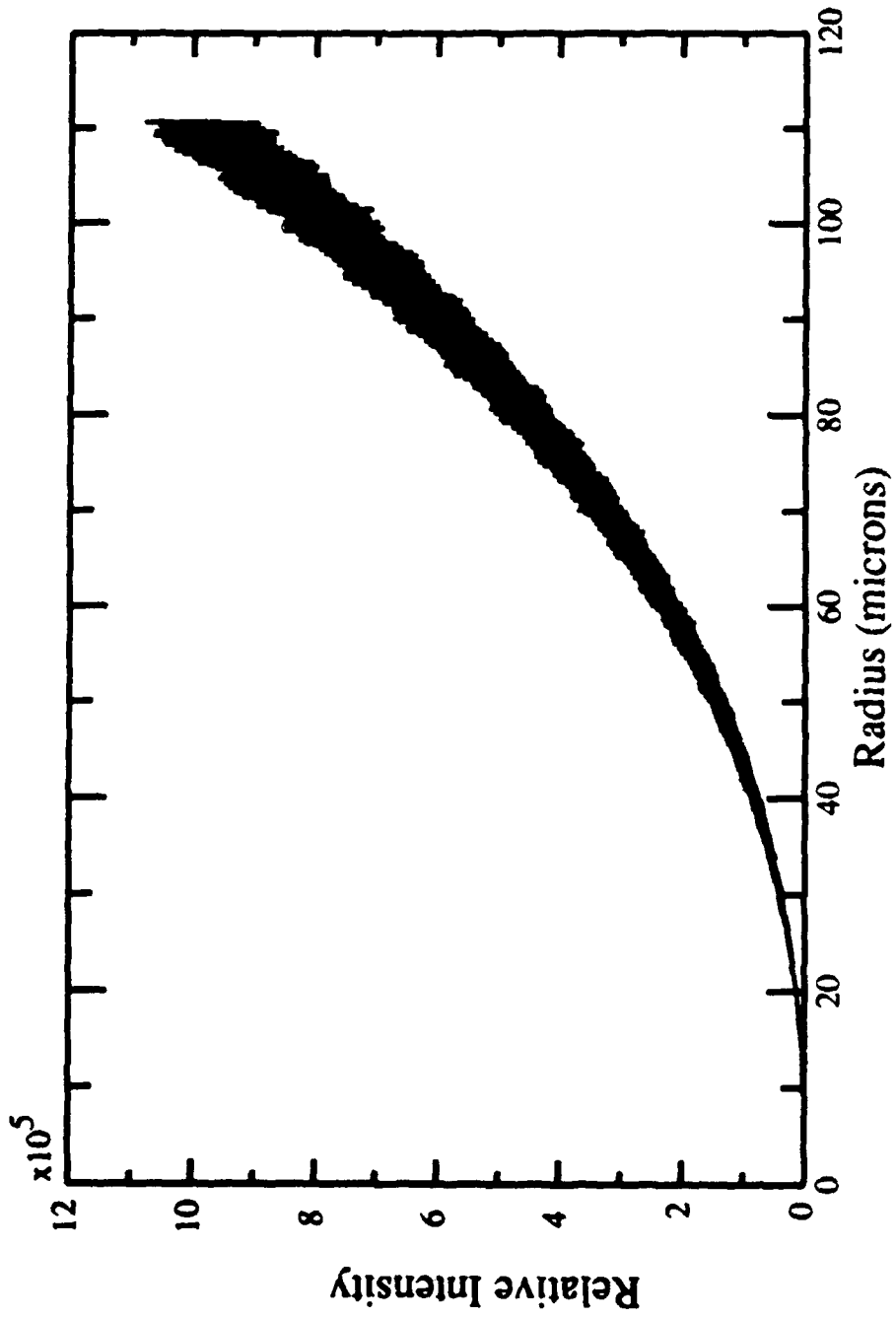


FIGURE 5

Theoretical scattered intensity as a function of the radius of the spherical scatterer (bubble). The wavelength in the bubble is 488.0 nm, and the scattering angle is 80 degrees from the forward. S_2 is plotted, corresponding to polarization of the incident beam parallel to the scattering plane.

interference of the reflected and refracted rays with an optical path length difference that is small compared to R , resulting in an interference pattern that varies slowly with radius. The fine structure, evident in Figs. 3-5, is due to the interference of the refracted, internally reflected ray and the coarse structure pattern. These rays have optical path length differences which are on the order of the bubble diameter, and hence the interference pattern is very sensitive to changes in the bubble size. At 80° , the reflected ray dominates the coarse structure as edge diffraction [50].

For a given photodetector combination, the finite solid angle subtended by the apparatus will have to be taken into account by an integration over the appropriate limits in θ and ϕ . In general, this will have the effect of eliminating the fine structure and mitigating the coarse structure, depending of course on the size of the angle. These calculations, which are detector-specific, will be presented in Chapter II in conjunction with the particular experimental arrangement.

Chapter II

Experiment

A. Method

To a large extent, this dissertation is a report of the success of an optical scattering method in obtaining $R(t)$ for a driven, stably oscillating bubble. As previously indicated, this is, though a significant step in bubble dynamics, merely a natural extension of Hansen's work in bubble sizing [54]. Although a variety of detection schemes have been employed, the method has remained constant throughout the course of the experiments. Figure 6 is a generalized schematic of the apparatus used in the experimental measurements, and serves as a guide for the discussion throughout this chapter.

An acoustic levitation technique [59-62] was used to obtain a single, stably oscillating air bubble in water contained in a resonating cell. Only bubbles with $R_0 < R_{cc}$ could be obtained by this technique. In practice, this meant that bubbles ranging from about 20 to 100 μm could be obtained.

Once a suitable bubble was obtained, a linearly polarized laser beam was scattered from the bubble, whose position in the beam was maintained by pressure adjustment and micropositioner stages upon which the levitation cell was mounted. For purely radial bubble motion, the scattered intensity $I(t)$ at some angle from the forward is related to the radius $R(t)$ in a nonlinear fashion for which a transfer function $I(R)$ is calculable from Mie theory. For other symmetric motions (shape oscillations), $I(t)$ is related to the motion of

the interface in some more complicated fashion; nevertheless, suitable methods of analysis of $I(t)$ should elicit information about the motion.

The scattered intensity $I(t)$ was measured using three different detection schemes which are described in the next section. Each of these detection schemes converts the incident light intensity to a photocurrent $i_p(t)$ which is linearly proportional to the input intensity $I_{exp}(t)$, and this current is converted to a voltage which is recorded for later analysis and graphical output. The next section describes in detail the different apparatus used in each phase of the experiment.

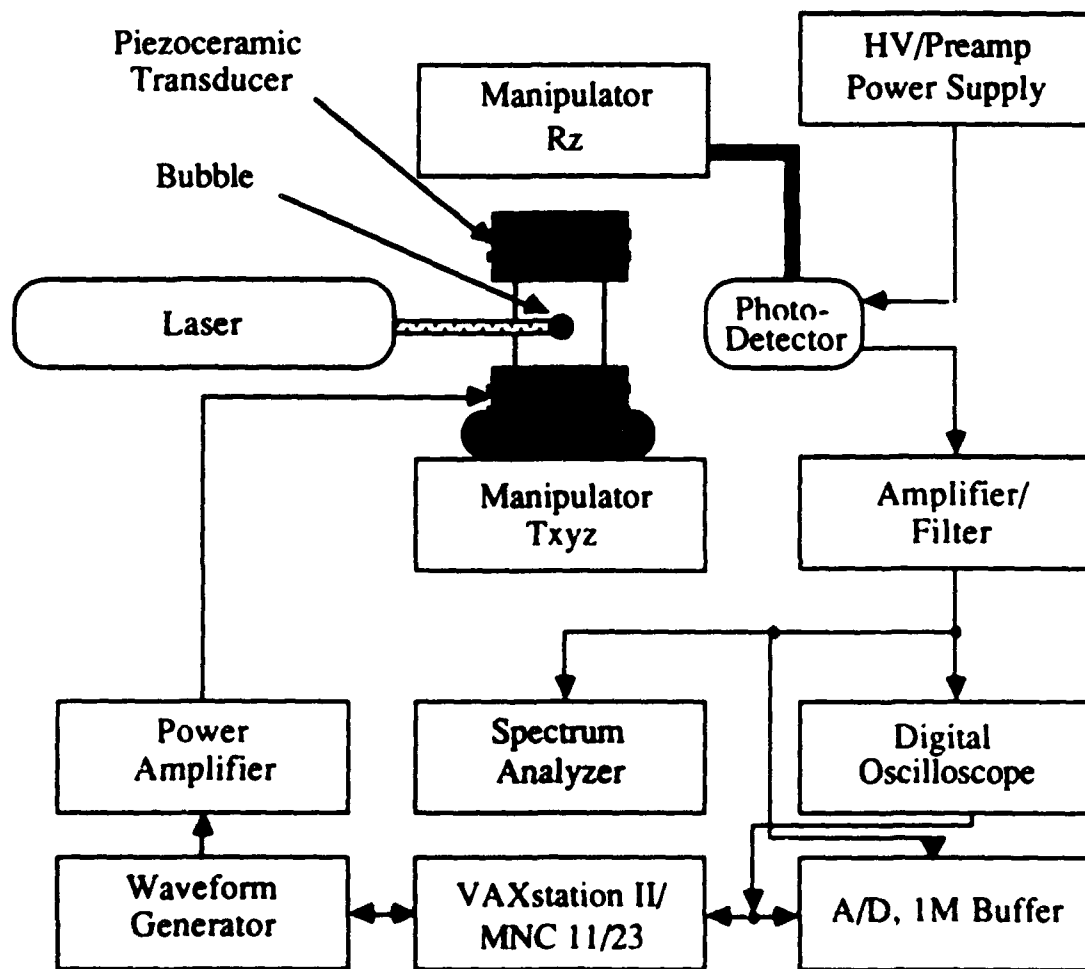


FIGURE 6

Generalized schematic of the experimental apparatus. Shading indicates a variable component of the system.

II. B. Apparatus

1. Base equipment

The unshaded components of Fig. 6 comprise the basic apparatus needed to levitate a bubble and analyze the data. This section describes these basic components.

In the center is the levitation cell. It consists of two 3" diameter, cylindrical piezoceramic (PZT-4) transducers, poled to be driven primarily in the thickness mode. The transducers are joined concentrically by a 3" long glass tube. Watertight coupling is ensured by the use of a silicone glue. A Plexiglas disc is glued to the bottom transducer, and the resulting container is filled to a specified level with distilled, filtered (1.0 μm particulate filter) water.

The cell is mounted on a three degree of freedom translation stage, providing 0.001" resolution and 1" travel in each direction with the use of manual micrometer drives. This arrangement allowed the positioning of the bubble anywhere in the plane perpendicular to the laser's axis of propagation. In addition, a 360° rotation stage with 0.01° resolution was mounted independent of, but concentric with the cell. This stage provided a variable, calibrated mount for the photodetectors. The entire apparatus, including the laser head and necessary optics, was mounted on a 4' x 6' optical table with self-leveling pneumatic supports for vibration isolation.

A frequency synthesizer/function generator coupled into a 75-watt power amplifier was used to drive the levitation cell with a periodic, sinusoidally-varying voltage. The driving frequency f was determined by the desired resonant mode of oscillation of the cell [64]. For all of the calibrated experiments, an (r, θ, z) mode of (1,0,1) was used, with $f =$

24.4 kHz. Additionally, some of the complex $I(t)$ traces were taken using a different cell operating in the (1,0,3) mode. The amplitude and frequency of the function generator were manually modulated.

Once the data were collected and stored in some buffer memory, they were transferred to a DEC VAXstation II for analysis and plotting using GGPLUS_V3 [63]. Completed graphs were stored to disk as Postscript files, and output to a laser printer.

II. B. 2. Detection schemes

a. RCA avalanche photodiode/lens combination

This first detection scheme utilized a 7 mW He-Ne laser operating at 632.8 nm in the TEM₀₀ mode. The output had a 500:1 linear polarization ratio and $1/e^2$ beam waist of 1.0 mm. The laser was mounted so that the electric field vector was parallel to the scattering plane defined by $\phi = 0$, and chosen parallel to the plane of the optical table.

The photodetector was a combination of a RCA model C30957E silicon avalanche photodiode and a 1.5" diameter, +14D fused silica lens placed such that the bubble was located at $+2f$, and the active area of the photodiode at $-2f$. The photodiode was reverse-biased at $V_r = 217$ volts, and a $1\text{M}\Omega$ load resistor was placed in series with the photodiode to convert the photocurrent i_p to a voltage measured across R_L . The output voltage was then amplified 40 dB and passed through a 100 Hz-200 kHz bandpass filter to improve the signal-to-noise ratio. The signal was split, with one terminus being an analog oscilloscope, and the other a KSC digitizer/memory module sampling at 1 MHz with 10-bit resolution and 1 M-word record length buffer. A MNC PDP 11/23 was used to control the CAMAC

crate in which the digitizer resided, and to retrieve the data from the buffer and transfer it to the VAXstation II.

All components were situated so that their center axis lay in the $\phi = 0$ plane, with $\theta = 70.0^\circ$. Fig. 4 shows the theoretical scattered relative intensity I_{rel} vs R at $\theta = 70.0^\circ$. Only the S_2 component is shown, corresponding to polarization of the incident electric field vector parallel to the scattering plane.

Although the active area of the photodiode was small ($\approx 1.0 \text{ mm}^2$), the lens subtended a large ($\theta_{acc} = \pm 10^\circ$) solid angle. To match this experimental condition, the integral $\iint I_{rel}(R) d\theta d\phi$ was performed for the limits $60^\circ \leq \theta \leq 80^\circ$, and $-10^\circ \leq \phi \leq 10^\circ$. The θ integration was performed by Gaussian quadrature after subdividing the 20° θ interval into 500 partitions and calculating $I_{rel}(R)$ for each partition. The ϕ integral was evaluated directly. Fig. 7 shows the results of the integration. The fine structure apparent in Fig. 4 has been eliminated, and the coarse structure has been diminished to such an extent that the inverse transfer function $R(I)$ is single-valued.

II. B. 2. b. Thorn/EMI photomultiplier tube

The second detection scheme also utilized the 7 mW He-Ne laser, but the detector employed was a Thorn/EMI model 9956KB photomultiplier tube (pmt). Negative high voltage (300 volts) was supplied to a standard voltage divider network located in the base of the pmt. A 100-kHz load resistor was placed just before the anode output, converting the anode current i_p into an output voltage. Negative supply voltage was chosen so that there was no need for an isolation capacitor at the output anode, thus enabling the observation of DC output voltage due to the constant light intensity associated with the

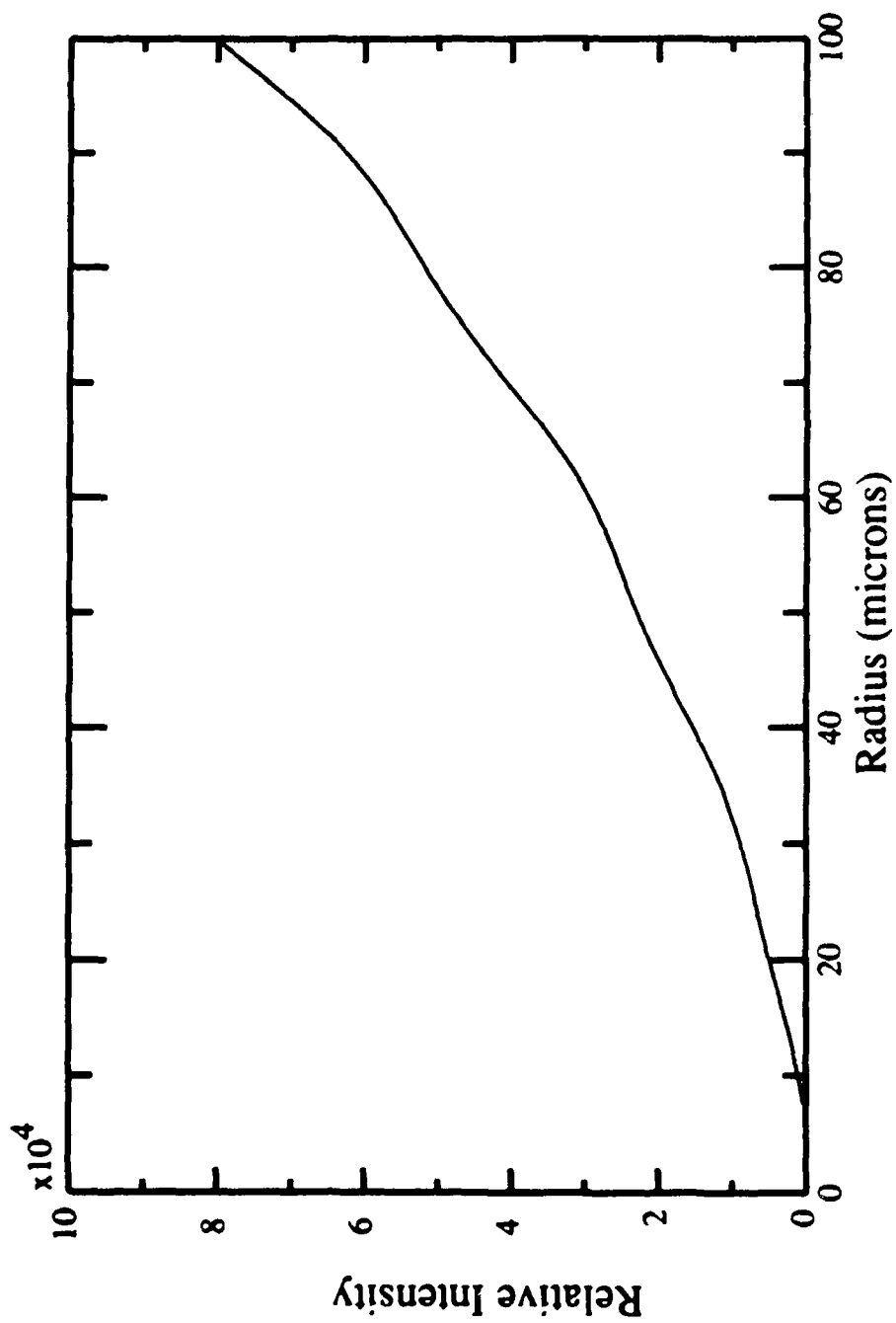


FIGURE 7

Results of integrating the theoretical scattered intensity over the solid angle (+/- 10 degrees) subtended by the RCA photodiode/lens combination centered at 70 degrees. The HeNe 632.8 nm line was used.

time-averaged scatter from the bubble. For linear oscillations, this time-averaged scattered intensity (and hence the DC voltage component) corresponds to the bubble's equilibrium radius R_0 ; i.e., $\langle I_{exp}(R,t) \rangle = I_{exp}(R_0)$.

For some data sets, the output voltage was sampled and stored by the KSC crate described in section B.2.a. of this chapter. For others, the output voltage was fed directly into a LeCroy 9400 digital oscilloscope with a variable sampling rate, and 8-bit resolution. The pmt was sensitive enough even at the relatively low supply voltage to detect optical noise in the form of light from the bubble which was multiply-reflected from the cell walls. This noise dominated the signal for small-amplitude oscillations. Due to its origin, the noise was modulated at the driving frequency, and therefore frequency filtering techniques were useless. However, the phase of the noise with respect to the bubble oscillation was random, and simple continuous averaging of the signal resulted in an increase in the signal-noise ratio of 2-3 orders of magnitude. These averaged data sets were stored in local memory buffers, and then were transferred to the computer via an IEEE-488 interface.

The window of the pmt covered a large ($\theta_{acc} = \pm 23^\circ$) solid angle centered at 66° from the forward direction. Fig. 3 shows I_{rel} vs R at 66° , and the solid curve in Fig. 8 shows the results of integrating I_{rel} over the limits $43^\circ \leq \theta \leq 89^\circ$, and $-23^\circ \leq \phi \leq 23^\circ$. The calibration data points were obtained by a method to be described in section C. of this chapter.

II. B. 2. c. Oriel photodiode

The final detection scheme, and the one which proved easiest to calibrate, used a 3 W Ar-I laser operating at 488.0 nm with a single line power of 440 mW in the TEM₀₀

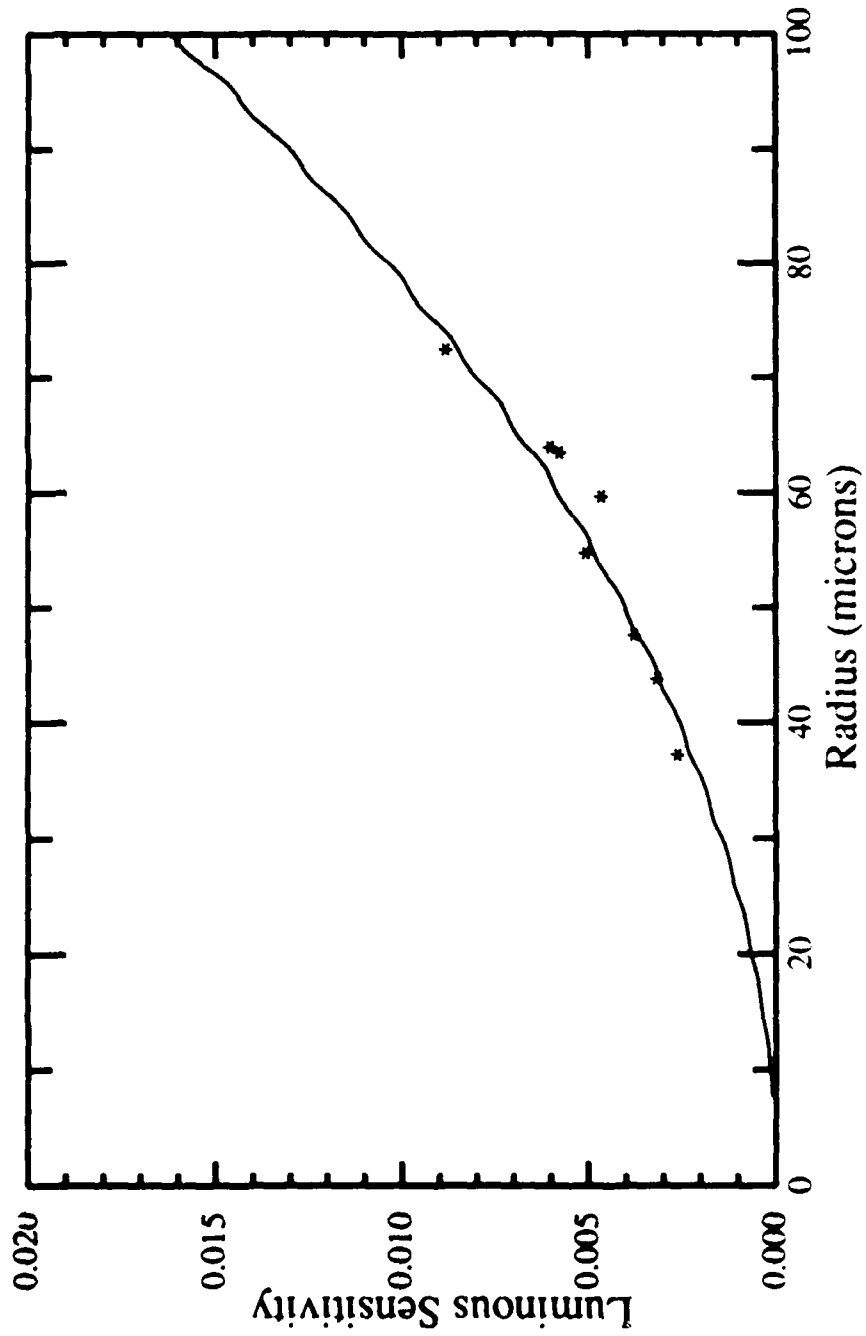


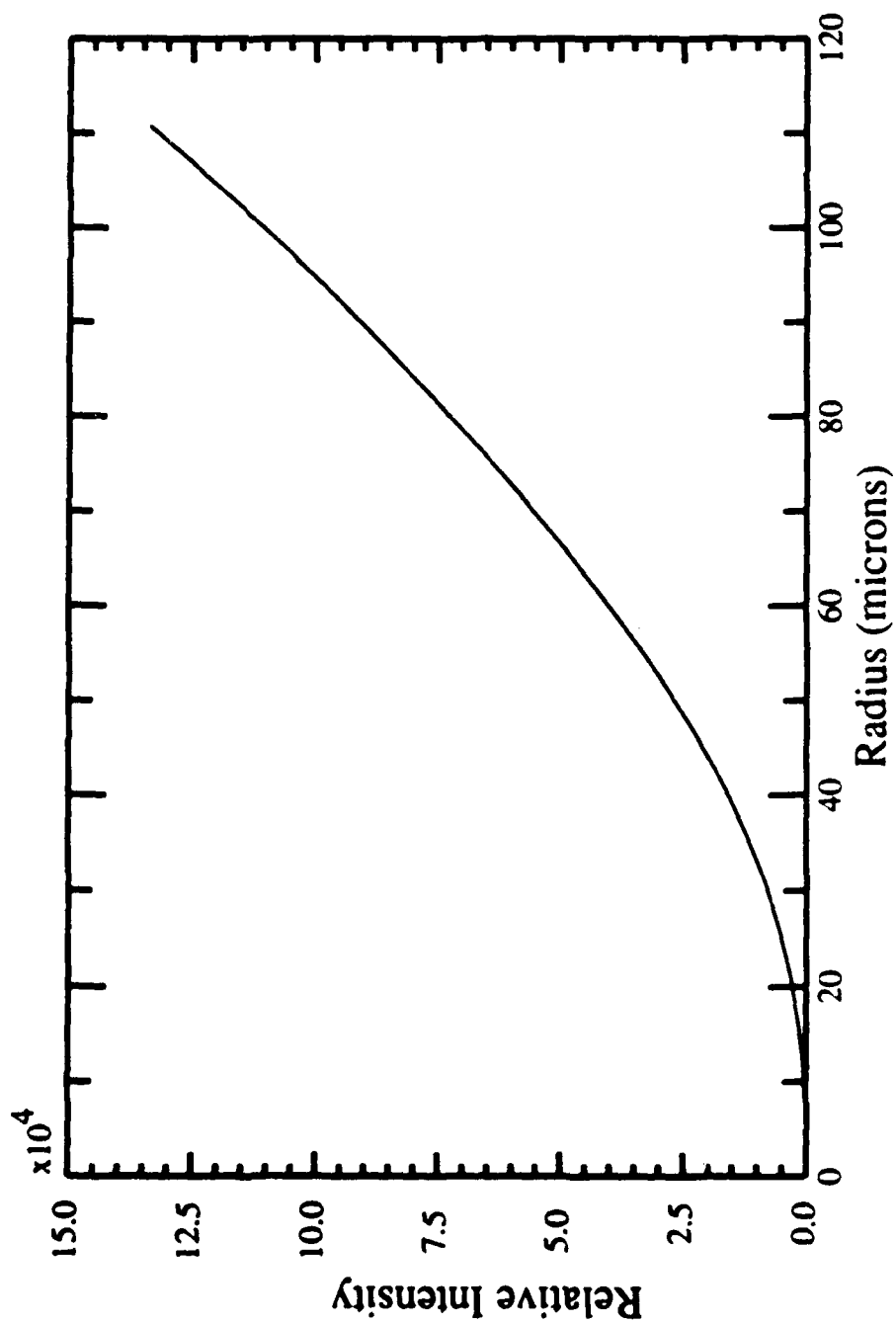
FIGURE 8

Calibration data for Thaw/EMI photomultiplier tube centered at 66 degrees and subtending a scattering angle of +/- 23 degrees. Wavelength in the bubble is 632.8 nm. Radius values are obtained using a msec-time technique.

mode. A rotating polarizer mounted on the laser ensured a 1200:1 linear polarization ratio, and the beam had a $1/e^2$ width of 1.0 mm nominal. The water-cooled head and power supply required a filtered flow rate of 2 gallons/minute, and the plasma tube current at 440 mW output was 18 A nominal in light-control mode. The polarizer was rotated so that the electric field vector was parallel to the scattering plane, which was also chosen parallel to the surface of the optical table.

The detector used was an Oriel model 7080-1 photodiode/preamp module with an integral optical transmission filter for the 488.0 nm line (Oriel model 52630) to reduce random light noise. The semiconductor active surface was very large (100 mm²), and for this reason a lens was not needed to get adequate light input. The trade-off was a rather large rise-time (1100 ns) which limited the bandwidth to \approx 1 MHz. The photodiode was operated in the photoconductive mode [65], with the resulting photocurrent i_p input to the inverting input of the integral preamp. A feedback resistor $R_f = 100$ k Ω connected the preamp output to the inverting input, and thus the output voltage of the preamp was $V_o(t) = i_p(t)R_f$. This voltage was fed into the 1 M Ω DC input of the LeCroy 9400 for observation and temporary storage before being transferred to the VAXstation II.

The photodetector was placed at a center angle of 80°. Fig. 5 shows I_{rel} vs R for $\theta = 80^\circ$, $\lambda_0 = 488.0$ nm. Fig. 9 shows the results of integrating over the solid angle subtended by the photodetector, $\theta_{acc} = \pm 4.81^\circ$. The functional form is approximately R^2 , as one would expect from physical optics approximations [51]. All of the calibrated $R(t)$ results in Chapter III are made with this detection scheme.

**FIGURE 2**

Results of integrating the theoretical scattered intensity over the solid angle subtended by, in this case, the Ortel photodiode, for which the spread in the scattering angle was ± 4.81 degrees. The wavelength in the bubble was 488.0 nm, and the center angle was 80 degrees.

II. C. Calibration

1. Cell pressure

The method used to calibrate the cell pressure is outlined in [26,66]. Since it necessarily involves some assumptions about the bubble motion, a brief description of the theoretical derivation of the condition for equilibrium of the bubble position is presented here. The procedure followed is then described. The technique involves levitating a bubble in the cell, measuring its equilibrium position with respect to the measured pressure gradient in the cell, measuring the equilibrium radius, and using the equation expressing the balance of the acoustic force and the buoyant force to solve for the pressure. It is a null method, and should be very sensitive to small changes in pressure.

The acoustic radiation force on a bubble in a standing wave field is given by

$$F_A(r,t) = - \langle V(t) \nabla P(r,t) \rangle, \quad (19)$$

where angle brackets denote time average, $V(t)$ is the instantaneous volume of the bubble and $P(r,t)$ is the pressure field. For the cell used in Fig. 6, the pressure is given by

$$P(r,t) = P_{\infty} - A \sin(kz) \cos(\omega t), \quad (20)$$

where P_{∞} is the ambient pressure, ω is the angular driving frequency, z is the vertical coordinate along the axis of the cell, and $k = 2\pi/\lambda$ is the experimentally determined wavenumber of the standing wave field (k is not ω/c since ω is below the cutoff frequency

of the cell). The wavelength λ is determined experimentally by measuring the distance from node to node of the stationary pressure field using a probe hydrophone constrained to move along the z axis, with a spatial resolution of 0.01 mm. For a spherical bubble of equilibrium radius R_0 and instantaneous radius $R(t)$, the magnitude of the acoustic force is

$$F_A = \frac{4}{3} \pi R_0^3 |A k \cos(kz)| \left\langle \left(\frac{R(t)}{R_0} \right)^3 \cos(\omega t) \right\rangle \quad (21)$$

Equation (21) is the levitation force which balances the buoyancy force

$$F_B = \frac{4}{3} \pi R_0^3 \rho g \left\langle \left(\frac{R(t)}{R_0} \right)^3 \right\rangle \quad (22)$$

where ρ is the liquid density and g the acceleration of gravity.

For calibration purposes, only bubbles oscillating linearly were used. Monitoring the uncalibrated output of the photodetector on an oscilloscope and a spectrum analyzer was sufficient to ascertain the linearity of the oscillation, and bubbles which exhibited any significant harmonic or subharmonic component were not used for calibration. Thus, to evaluate the time averaged quantities in (21) and (22), we can use a linearized treatment of the bubble oscillations, following Prosperetti [21]. The pressure in the bubble is treated with the polytropic relation, equation (1), and the radial equation is linearized by writing $R = R_0[1 + x(t)]$, and expanding x in a power series, retaining only linear terms.

The condition for equilibrium is the equality of (21) and (22). Using the above assumptions, the expression for the amplitude of the driving pressure A is

$$A = \frac{\rho g}{3k \cos(kz) \langle x \rangle}, \quad (23)$$

where all the quantities on the right-hand-side can be evaluated experimentally. In the absence of a calibrated light detection system, the quantity $\langle x \rangle$ must be determined theoretically, and the result is given in [26].

The procedure is straightforward. First, the pressure gradient is obtained via an external hydrophone probe mounted on a micropositioner with 50 mm vertical travel and 0.01mm travel resolution. This measurement also gives k , the wavenumber. For $f = \omega/2\pi = 24.4$ kHz, and the (1,0,1) resonant mode, $k = 0.6 \text{ cm}^{-1}$. Next, a bubble was levitated and monitored via the scattered light to ensure linear oscillations. The position of levitation and the equilibrium radius R_0 were measured for a range of input cell voltages. R_0 was measured via a rise-time technique [54]. The data were entered into the computer to calculate the calibration constant in volts_{rms} / atm for the input driving voltage as read from the frequency synthesizer. The value $\langle x \rangle$ was calculated theoretically. The calibration constant thus determined was $1.7 \pm .05$ volts_{rms} / atm. The precision of the constant was determined by the standard deviation of the estimated values of the constant for each data point. Typical pressure values determined using this constant and the driving voltage as recorded for average data runs were on the order of 0.05 atm.

Unfortunately, numerical results calculated using the experimentally determined pressure values for particular data sets gave an unrealistically low oscillation response. Comparison with previous results for a similar cell with $f = 23$ kHz indicated that typical pressures should be around 0.2 atm, and numerical results calculated with the higher

pressures gave reasonably good fits. Accordingly, the pressures given for the graphs in chapter III are the results of fitting experimental response curves with numerically generated response curves using the model in [9]. The choice of the best fit was determined by the goodness of fit in the off-resonance regions, since the height of the resonance peaks is critically dependent on the nonlinear damping, and hence the resonances would be the first places where any discrepancies between theory and experiment should show up.

In previous studies [25,26,62], and in an early version of this experiment, the pressure was calibrated with respect to the voltage output of a pill transducer mounted on the outside of the glass cylinder. The glass was assumed to oscillate in phase with the liquid. The output impedance of such a transducer is $> 10 \text{ M}\Omega$, and this caused loading of the signal when attempts were made to measure the output of one such transducer with the KSC digitizer. To remedy this situation, it was determined to calibrate with respect to the driving voltage, using the $50 \text{ }\Omega$ parallel output of the driving oscillator as a signal source.

The problem with this approach, and the apparent reason for the failure of the calibration results, is that the input voltage is an inaccurate measure of the power delivered to the cell. Recall that the levitation cell is itself a resonant system, and is sensitive to temperature and frequency changes. Although the cell was maintained at resonance, tuning was accomplished only at sporadic (between data points, for example) time intervals, and discrete frequency intervals, since a digital frequency synthesizer/function generator was used. To determine the value for the resonance frequency, the position of the bubble as measured in a microscope was minimized (and hence the acoustic radiation pressure was maximized) by varying the frequency with a preset resolution, always 0.1 kHz . Although this was more than adequate frequency resolution with respect to the ratio R_0/R_{res} , which

was limited by the accuracy of the rise-time measurements, it was not accurate enough to sufficiently resolve the resonance peak of the cell, which was a weakly damped system.

Therefore, measurements of the driving voltage were made assuming a resonant condition. If indeed this was not the case, then, although the driving voltage would remain constant, the power delivered to the cell would be less than at resonance, since the impedance of the cell would increase away from resonance. Additionally, the ratio of the pressure output to the power input would decrease, since the stationary wave resonance condition would not be fully realized. The calibration constant thus obtained would be too large, and the pressures calculated with it too small, and this inaccuracy is apparently the reason for the disparate values for the pressure obtained. For future measurements, plans call for either the reintroduction of an external transducer combined with a suitable impedance buffer, or the use of a power meter between the amplifier and the cell, as the reference signal for the pressure calibration.

II. C. 2. Photodetector current

The method used for calibrating the photodetector current was the same for each photodetector. The general method will be outlined here.

The electric signal to be measured is $V_{exp}(R,t) = G i_p(R,t) R_L$, where G is the total gain factor of the intermediate electronics, R_L is the load or feedback resistance, and i_p is the photocurrent. The photocurrent $i_p(R,t) = A \mathcal{R} I_{exp}(R,t)$, where \mathcal{R} is the total responsivity of the photodetector in amps/watt, and A is the area of the photo-sensitive surface. Finally, $I_{exp}(R,t) = I_0 \iint I_{rel}(R(t)) d\theta d\phi$, where the limits on the integral are determined by the particular photodetection scheme used. Thus, $V_{exp}(R,t) = \Phi \iint I_{rel}(R(t))$

$d\theta d\phi$, where $\Phi = GR_L A \mathcal{R} I_0$ is an apparatus-dependent constant to be determined empirically.

First, a stably oscillating bubble is obtained in the cell and moved into the beam. The output voltage $V_{exp}(R, t)$ is monitored on an oscilloscope. The time average $V_{exp}(R_0) = \langle V_{exp}(R, t) \rangle$ is recorded. Only linearly oscillating bubbles are used, since $R_0 = \langle R(t) \rangle$ only for linear oscillations, and hence $\langle I_{exp}(R, t) \rangle = I_{exp}(R_0)$ only for linear oscillations. As $V_{exp}(R_0)$ is being recorded, an independent measurement of R_0 is made using a rise-time technique similar to that used by Crum [25] and Hansen [50]. In this fashion a set of calibration data points is accumulated spanning the widest possible range of equilibrium radii. The data were also taken for a range of driving pressures to ensure there were no spurious effects due to rf noise. The calibration constant Φ was then determined by taking the unweighted average over all data points (and hence a wide range of R_0) of the ratio of the experimental voltage to the relative intensity, *i.e.*,

$$\Phi = \frac{\sum_i^N \phi_{exp,i} = \frac{V_{exp,i}(R_0)}{\iint I_{rel}(R = R_0) d\theta d\phi}}{N} \quad (24)$$

where N is the number of data points. Multiplying Φ by the photodiode output $V_{exp}(R, t)$ gives the experimental relative intensity, which can then be used to find the radius $R(t)$.

Multiplying Φ by the calibration data $V_{exp}(R_0)$ and plotting these data on the same graph as the theoretical integrated relative intensity $\iint I_{rel}(R) d\theta d\phi$ gives an indication of the accuracy of the calibration. The data points in Fig. 8 are an example of this method of calibration applied to the pmt. The units for the y-axis are lumens, and represent the actual,

not relative intensity. The reason for this is that \mathcal{R} was supplied by the manufacturer in units of amps/lumen.

Fig. 10 shows the calibration data versus radius for the Oriel photodiode described in section B.2.c. of this chapter. These data were taken over a period of two weeks, with a temperature variance of $\pm 1^\circ \text{C}$ maximum between any two runs. The solid curve is the integrated relative intensity obtained in Fig. 9. The increased scatter for large bubble sizes is attributable to two factors. First, the rise-time measurements become more difficult to make with larger bubbles due to the speed of their ascent. Thus the spread in the value of R becomes greater. Second, larger bubbles are harder to center in the laser beam, causing some variance in the value of the intensity. A maximum estimate for the error in a radius value determined using this calibration is about 9% for large bubbles ($R > 80 \mu\text{m}$), and about 4% for small ($R < 40 \mu\text{m}$) bubbles.

As an indication of the error introduced by taking calibration data for nonlinearly oscillating bubbles, Fig. 11 shows $\langle V_{exp}(R,t) \rangle$ for all data sets taken with the Oriel photodiode. The x-axis is plotted as a ratio of the equilibrium radius to the resonance radius. This is done to illustrate the fact that one expects deviations due to nonlinearities in the response to be greatest at the resonances (see the family of resonances in Fig. 1). As expected, a noticeable variation occurs at $R_0/R_{res} = 0.5$, the second harmonic resonance.

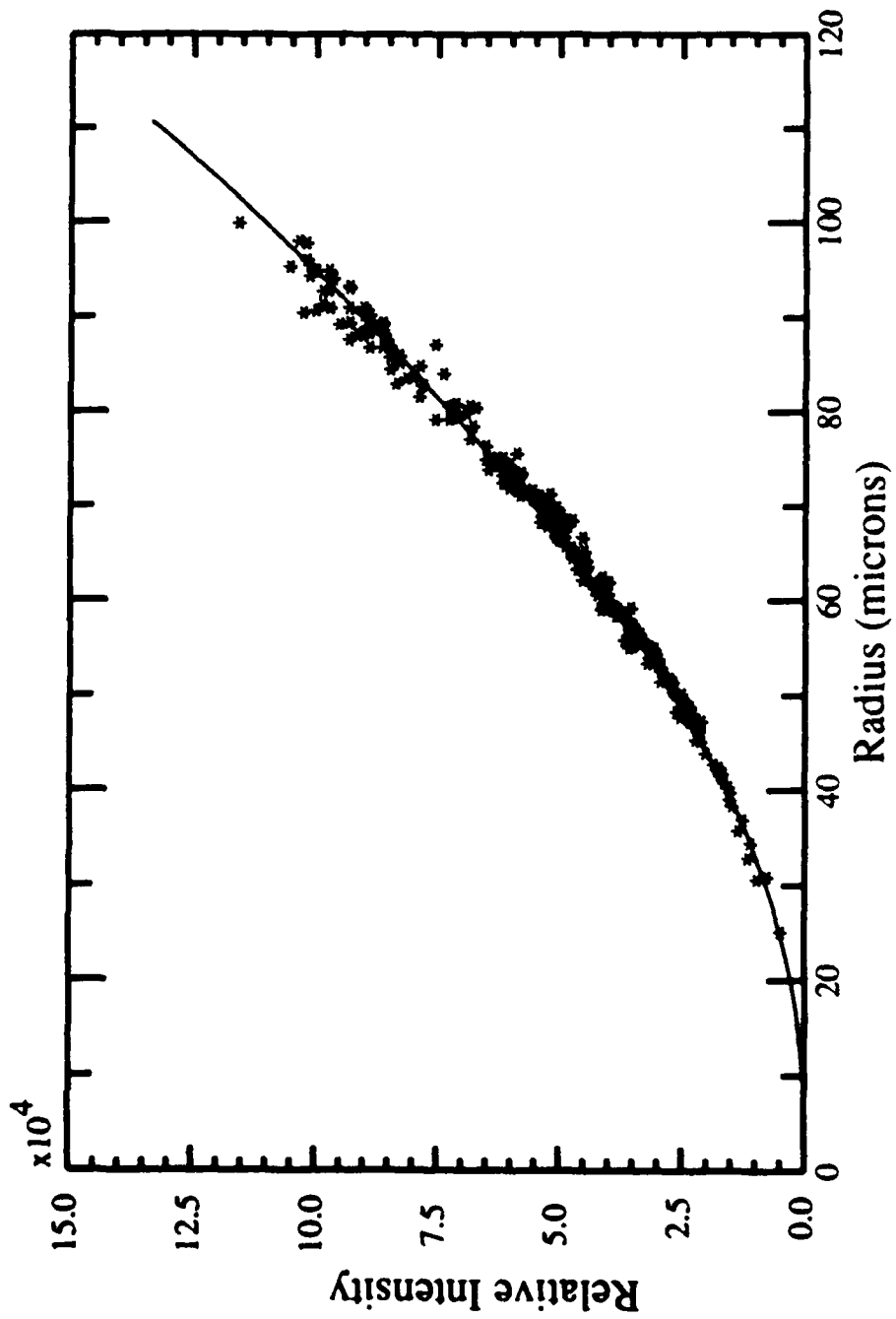


FIGURE 10

Data and theory for the photodiode with solid angle of ± 4.81 degrees centered at 80 degrees. Wavelength in the bubble is 488.0 nm. The radii were obtained by a rise-time technique.

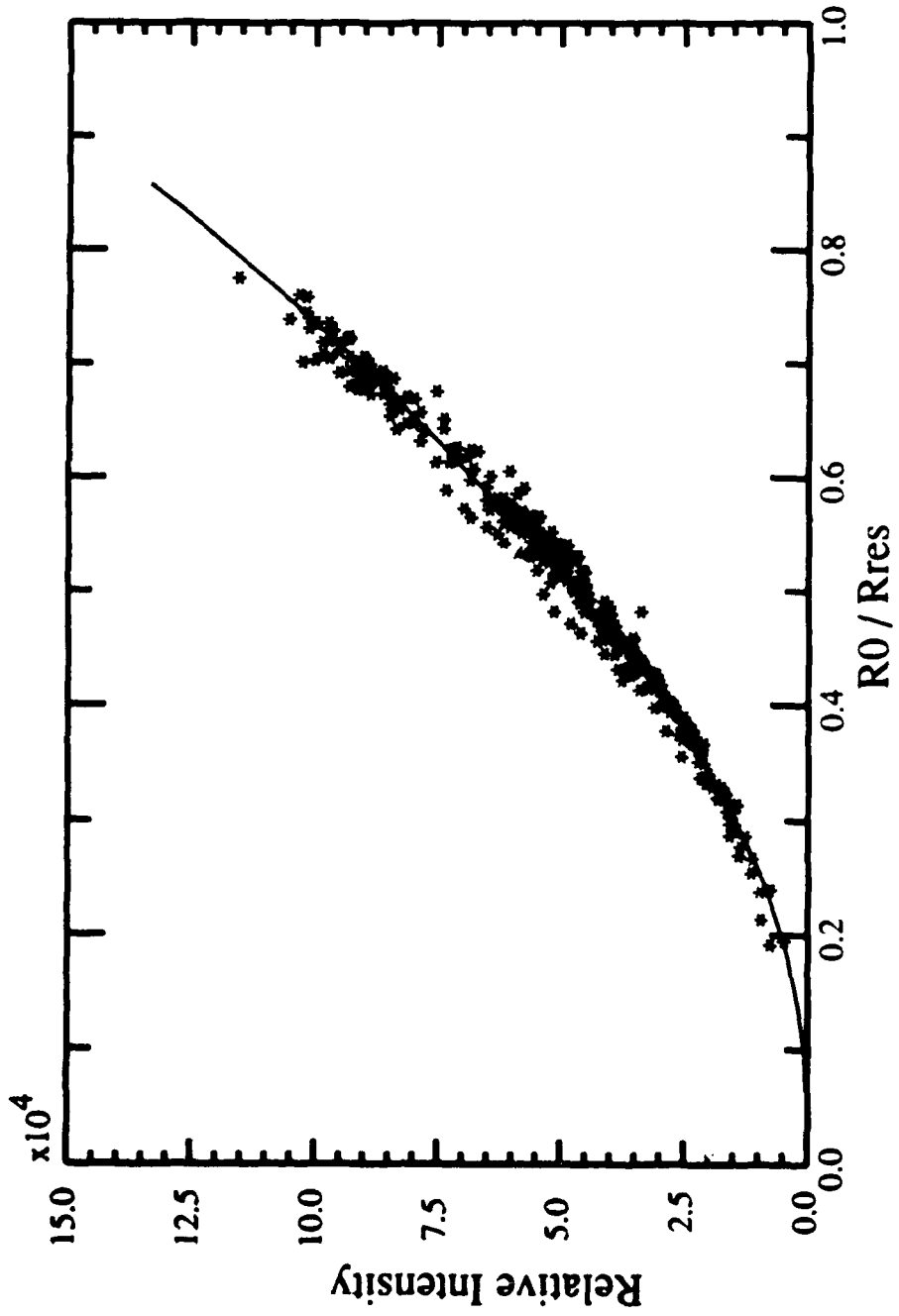


FIGURE 11

All data taken with Ornel photodiode centered at 80 degrees, wavelength = 488.0nm, plotted as a function of the ratio of the equilibrium radius to the resonance radius at 24.38 kHz.

II. D. Procedure

1. Introduction

This section will describe briefly the procedures used to obtain the data presented in chapter III. In all cases, distilled, filtered ($0.1 \mu\text{m}$) water was introduced to the cell. A pre-set height of the water in the cell was maintained, determining the resonance frequency f . An initial bubble was obtained by increasing the pressure amplitude until cavitation occurred, and decreasing the pressure until the bubble was stably levitated. The cell was then tuned, *i.e.*, the driving frequency was swept while monitoring the bubble's levitation position to find the resonance frequency. This was determined as described in II.C.1. by minimizing the bubble's position in the z-direction. In this fashion, the resonance frequency was maintained to within ± 0.1 kHz for all the data sets.

Using the micropositioners, the levitation cell was moved relative to the laser beam until the bubble was centered in the beam. This position was determined by monitoring the maximum DC component of $V_{exp}(R,t)$ on an oscilloscope. With the bubble in the beam center, the system was ready for data acquisition.

II. D. 2. $I(t)$ curves

Once a record length was established, the bubble was observed until an event or region of interest was attained. The digitizers were then manually triggered, typically (though not always) sampling at a rate of 1 Msample/sec, depending of course on the particular detection system employed. With the RCA photodiode/lens combination, the

filtered, amplified signal was directly digitized by the KSC system. With the pmt, small-amplitude oscillations were continuously summed and averaged to eliminate random optical noise, and the averaged signal was stored on the digital oscilloscope. For large-amplitude oscillations, the pmt output was fed directly into the KSC system. With the Oriel photodiode, voltages were continuously averaged to uncover the signal buried in the random electrical noise, then the averaged signal was stored.

The stored $V_{exp}(R,t)$ data were input into a program which multiplied the voltage by Φ to obtain $I_{exp}(R,t)$. The I_{exp} values were then compared with the contents of a two-dimensional array containing the pairs $(\iint I_{rel}(R) d\theta d\phi, R)$. If $I_{exp}(t_i)$ matched a tabulated value, then $R(t_i)$ was written. If not, then linear interpolation was performed to find a suitable $R(t_i)$. Analysis and plotting, to be discussed in chapter III, were then performed. If the behavior was sufficiently complex, then V_{exp} was left as a relative intensity for analysis.

II. D. 3. Response curves

For the response data, once a suitable bubble was in the beam, then three data values were recorded: V_{max} , V_{min} , and either V_{ave} or t_r , the rise time, for determining R_0 . R_0 was varied in one of two ways. The first, applied if the driving pressure was low and the gas concentration in the liquid was undersaturated, was to start with a large bubble and let it dissolve, taking data as it dissolves. It took approximately 1-2 hours to obtain a range of data from $R_0 = 80$ to $R_0 = 30 \mu\text{m}$. The second, applied if the driving pressure exceeded the threshold for rectified diffusion [61,67], was to start with a small bubble and let it grow towards resonance size. This took about 30 min to 1 hour. The three voltages were

then converted to radii using the look-up table described above, and a response measure $(R_{max} - R_{min})/2R_0$ was plotted against R_0/R_{res} .

Chapter III

Results

A. Radial motion

1. Response curves

To compare with Fig. 1, Fig. 12 plots a family of resonance curves for three different driving pressures. The discrete points are experimental data, and the solid curves are numerical results generated using equations (2), (4), and (5) for best-fit pressures of 0.14, 0.2 and 0.24 atm, in ascending order. The data, though sparse, show good agreement with the theory. The salient feature is the presence of the second harmonic resonance (corresponding to a response with a frequency component of $2f$), which has been seen indirectly by Crum *et al.* [25,26,61], but never before measured.

Figs. 13 through 19 show resonance curves for increasing values of the driving pressure, from 0.12 to 0.24 atm. All show, to a greater or lesser extent, the second harmonic resonance. For some data sets, notably Figs. 14 and 16, an inexplicable difference in the height of the peak is seen. Also, Fig. 13 shows an anomalous data point well above the top of the second harmonic peak. The point corresponds to a subharmonic oscillation of periodicity 2, that is, of basic frequency $f/2$, where f is the driving frequency. These differences in data and theory are also seen in the $R(t)$ results of the next section, and a full attempt at explanation follows in chapter IV.

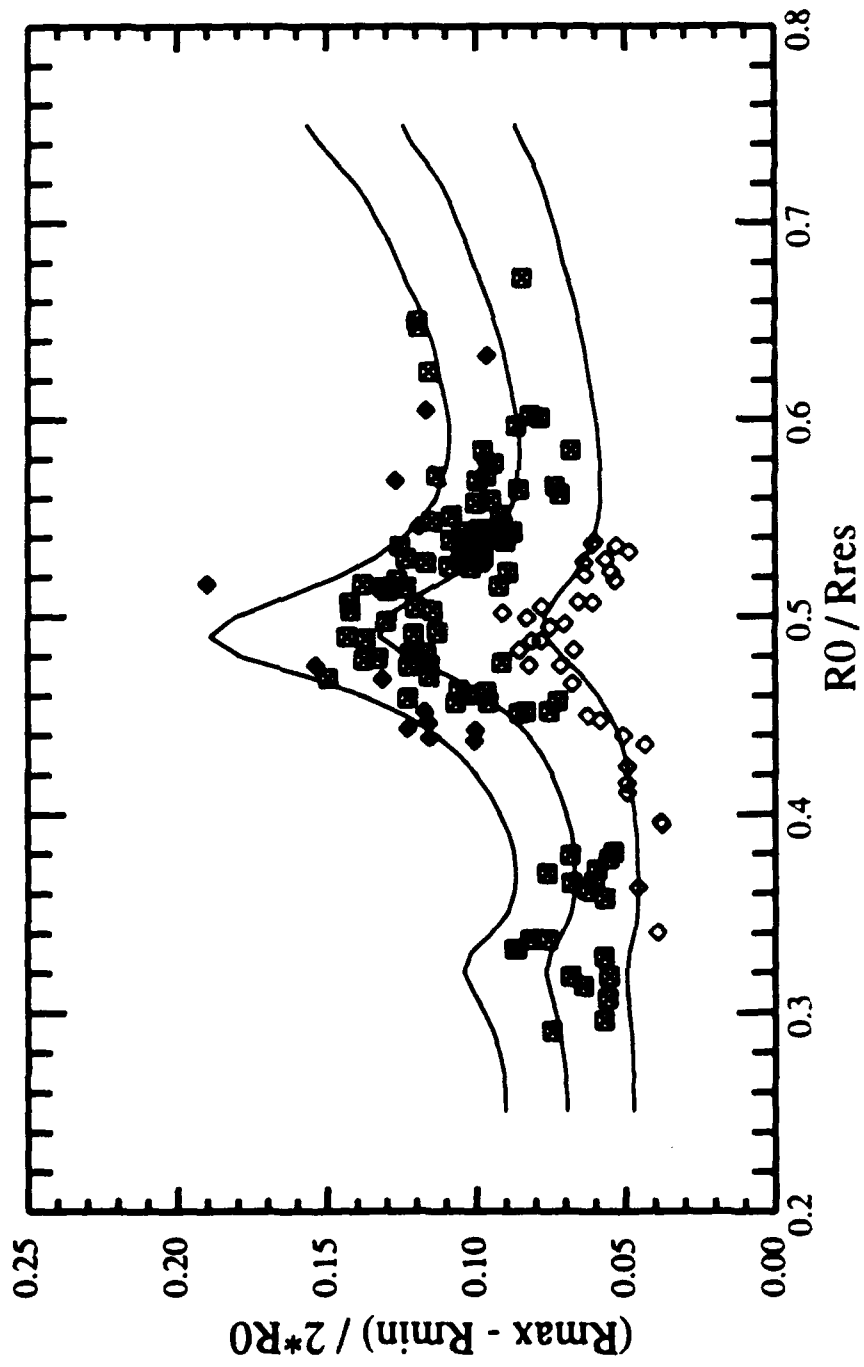


FIGURE 12

Data and theory for (in ascending order) $P = 0.14, 0.20,$ and 0.24 atm. Data are taken with Ortel photodiode, with $f = 24.4$ kHz.

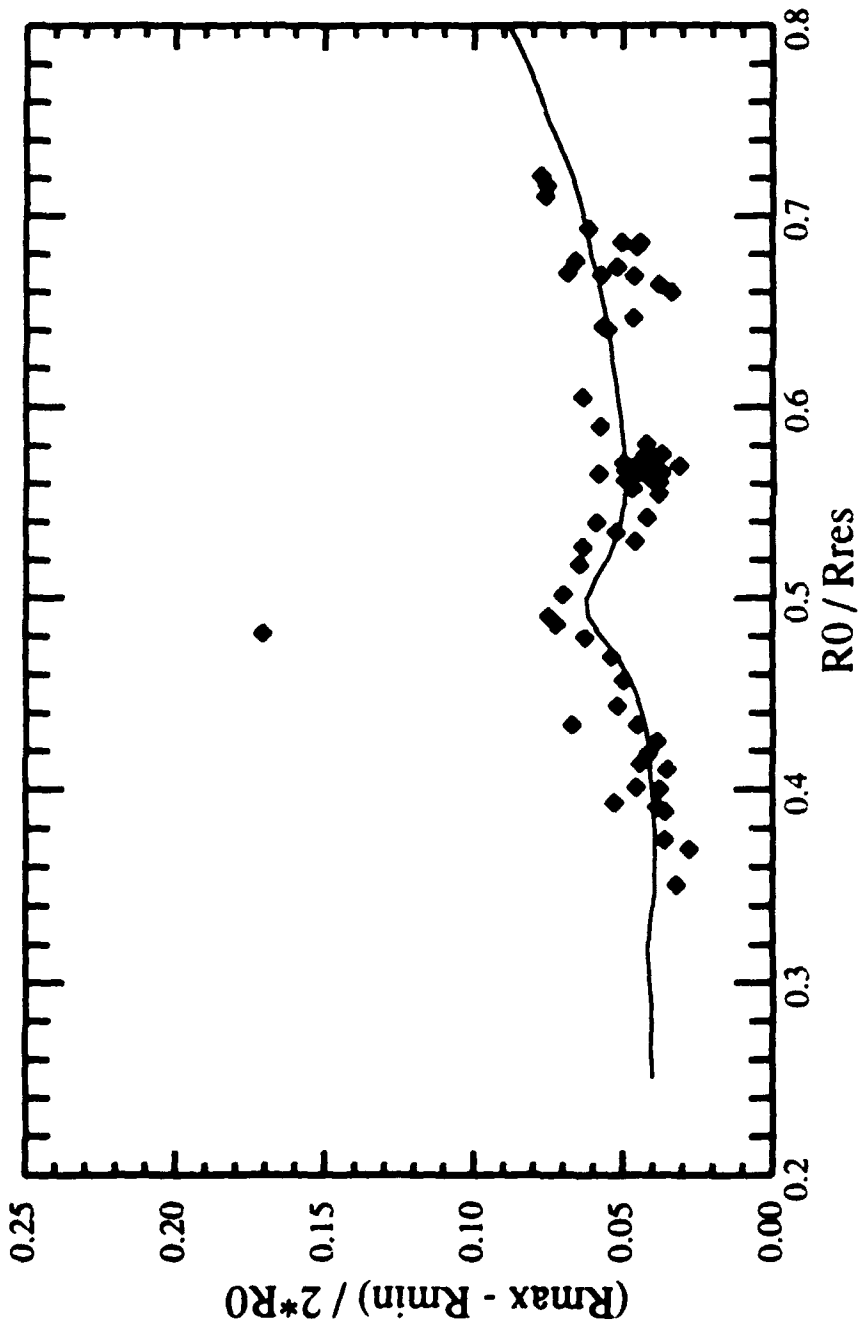


FIGURE 13

Resonance data and theory for $P = 0.12$ atm, $f = 24.4$ kHz. Anomalous data point corresponds to a period-2 subharmonic oscillation.

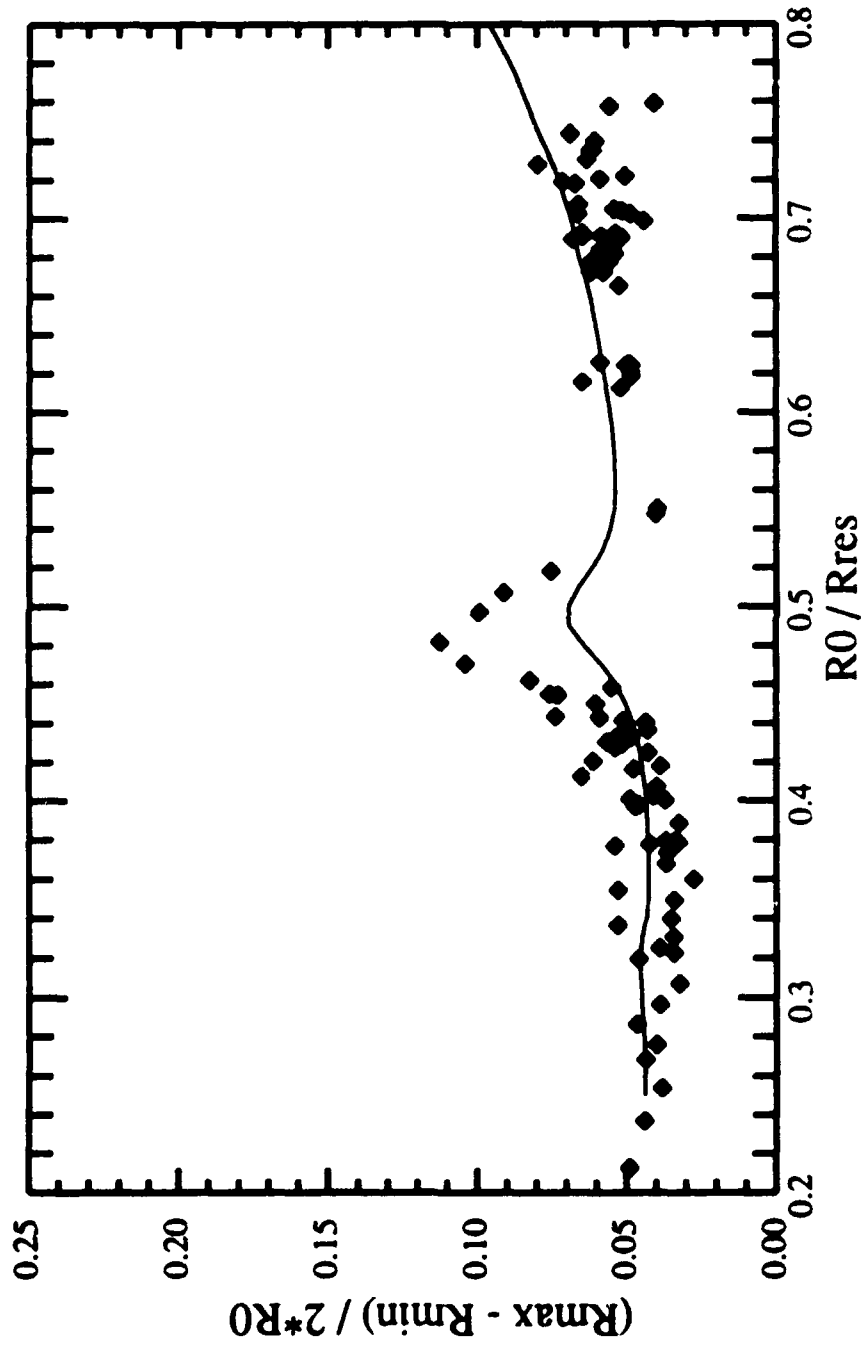


FIGURE 14

Resonance data and theory for $P = 0.13$ atm, $f = 24.4$ kHz.

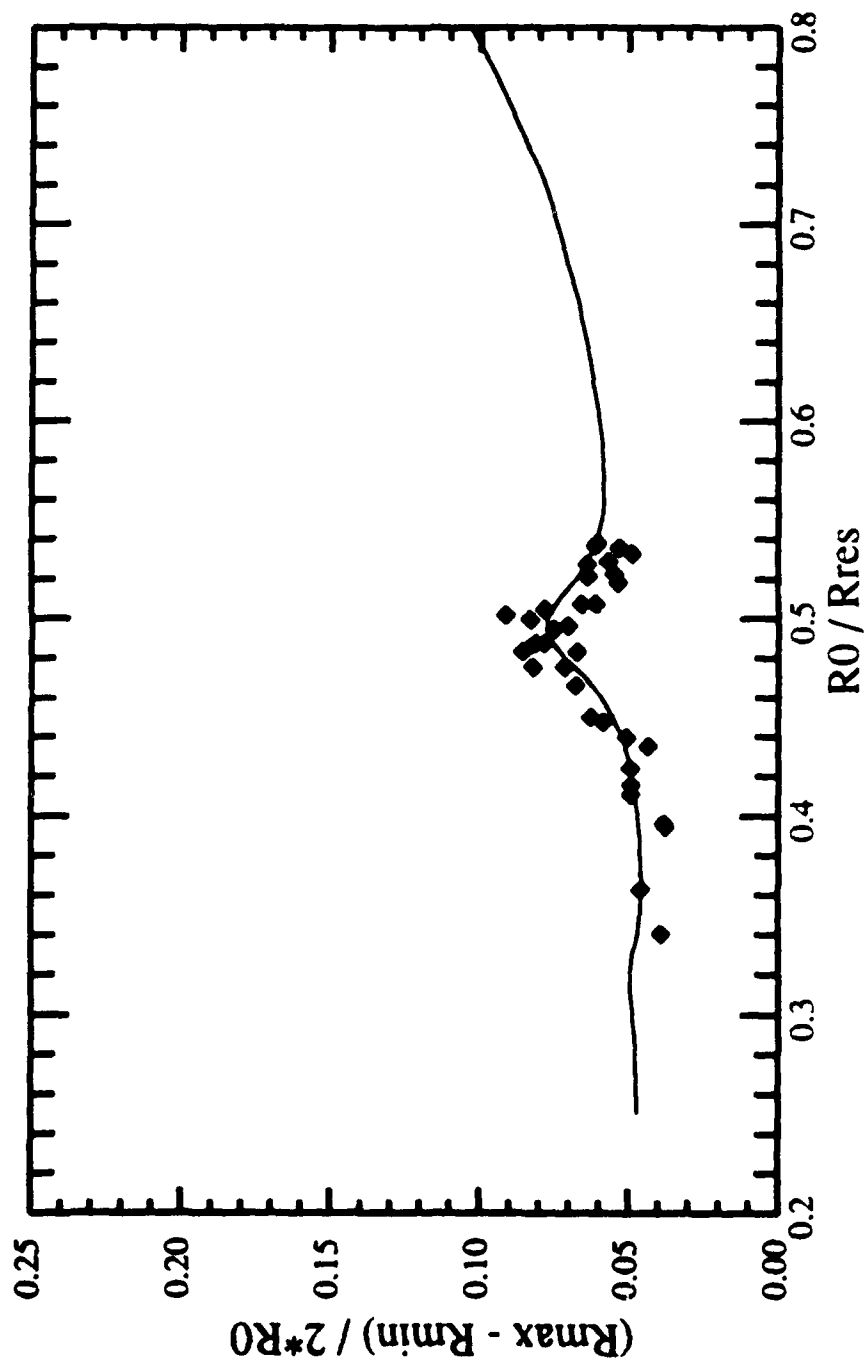


FIGURE 15

Resonance data and theory for $P = 0.14$ atm, $f = 24.4$ kHz.

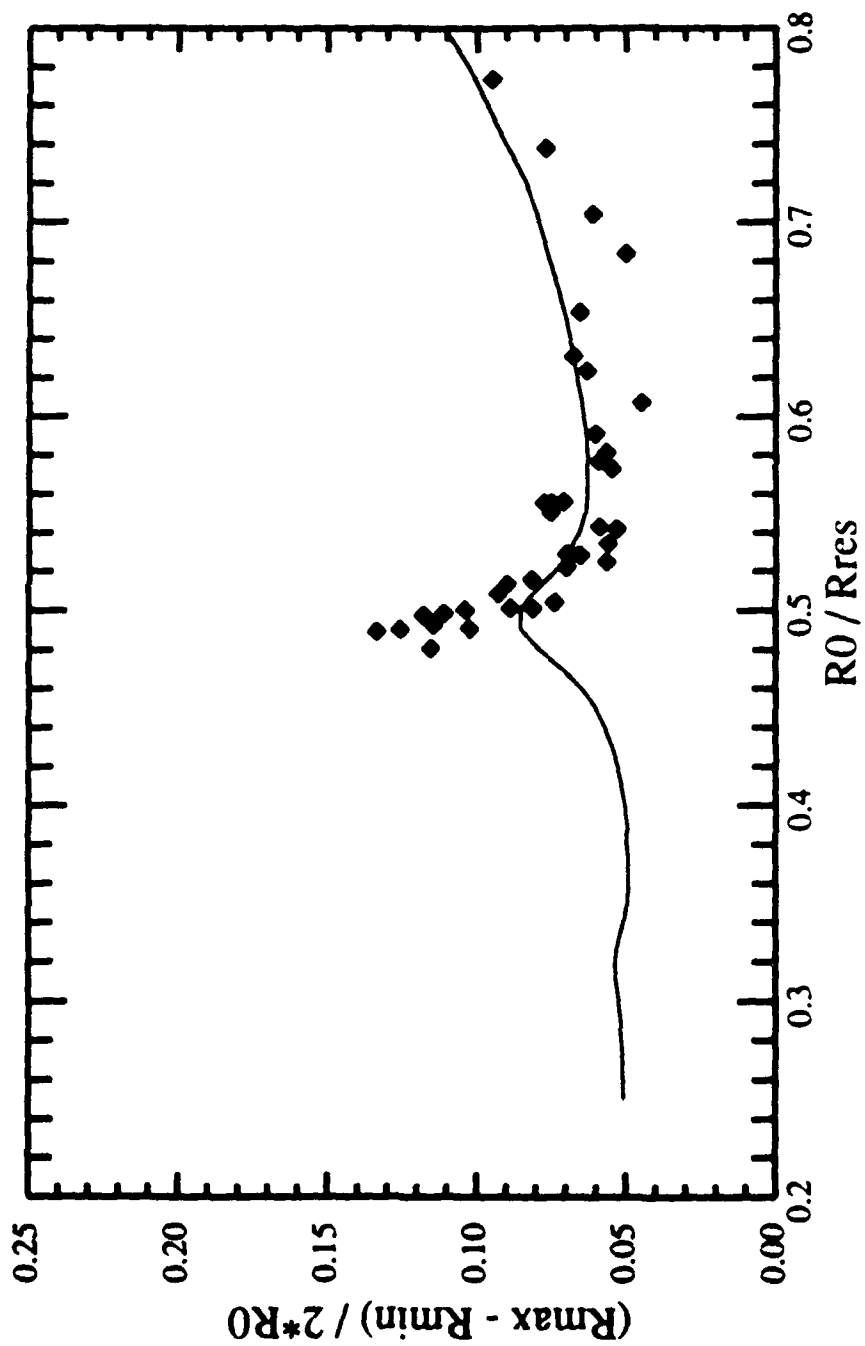


FIGURE 16

Resonance data and theory for $P = 0.15$ atm., $f = 24.4$ kHz.

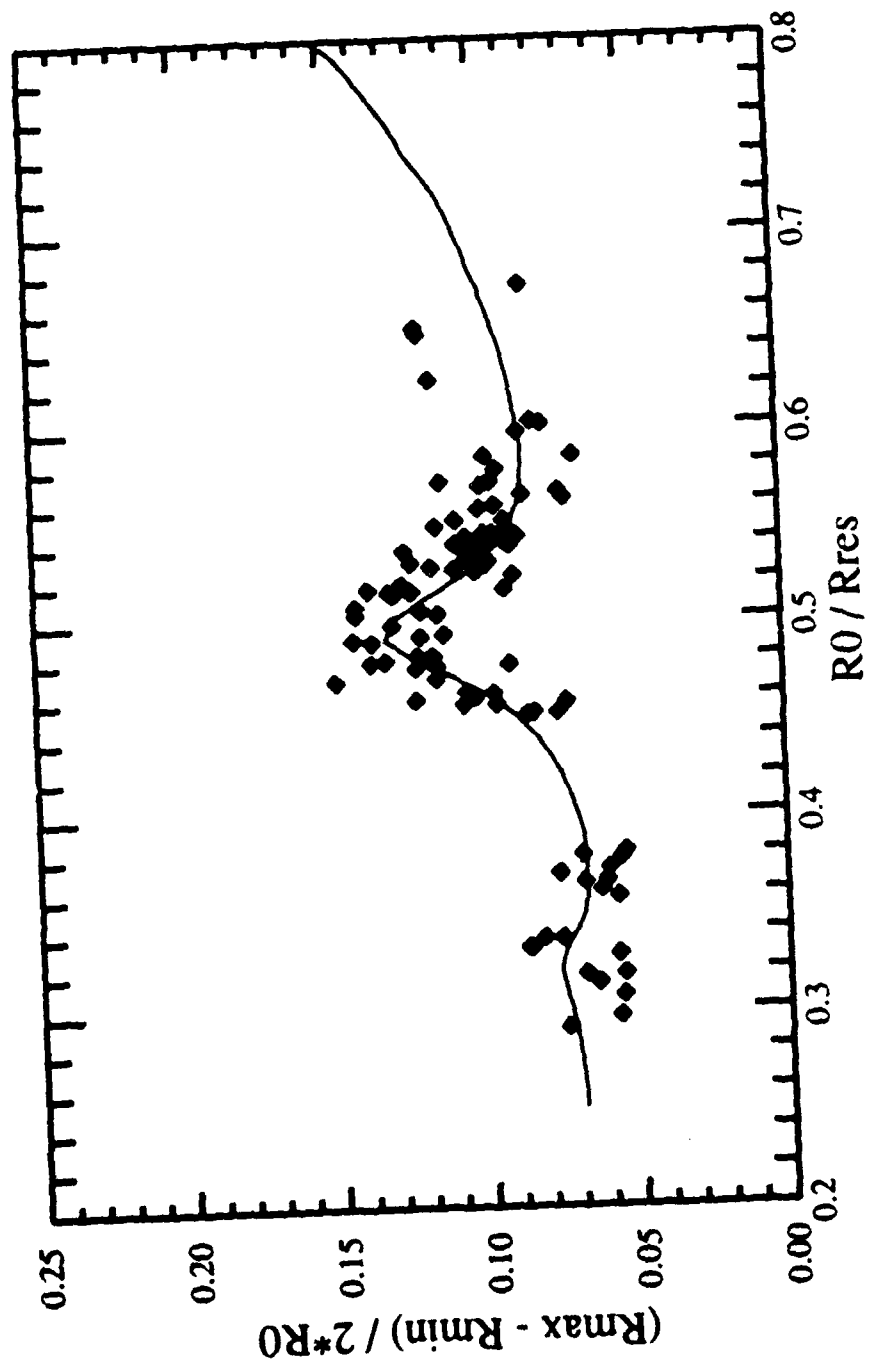


FIGURE 17

Resonance data and theory for $P = 0.20$ atm, $f = 24.4$ kHz.

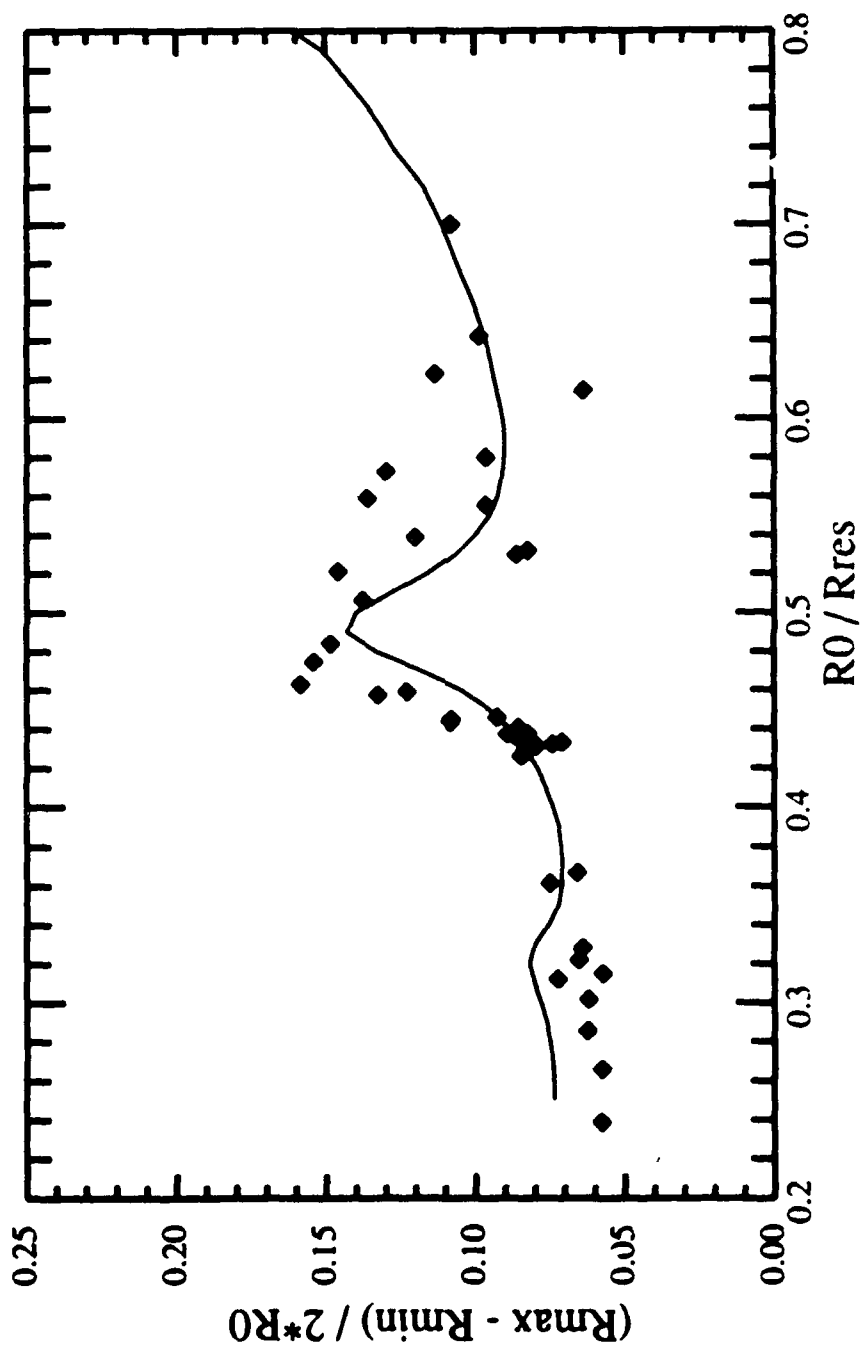


FIGURE 1B

Resonance data and theory for $P = 0.21$ atm, $f = 24.4$ kHz.

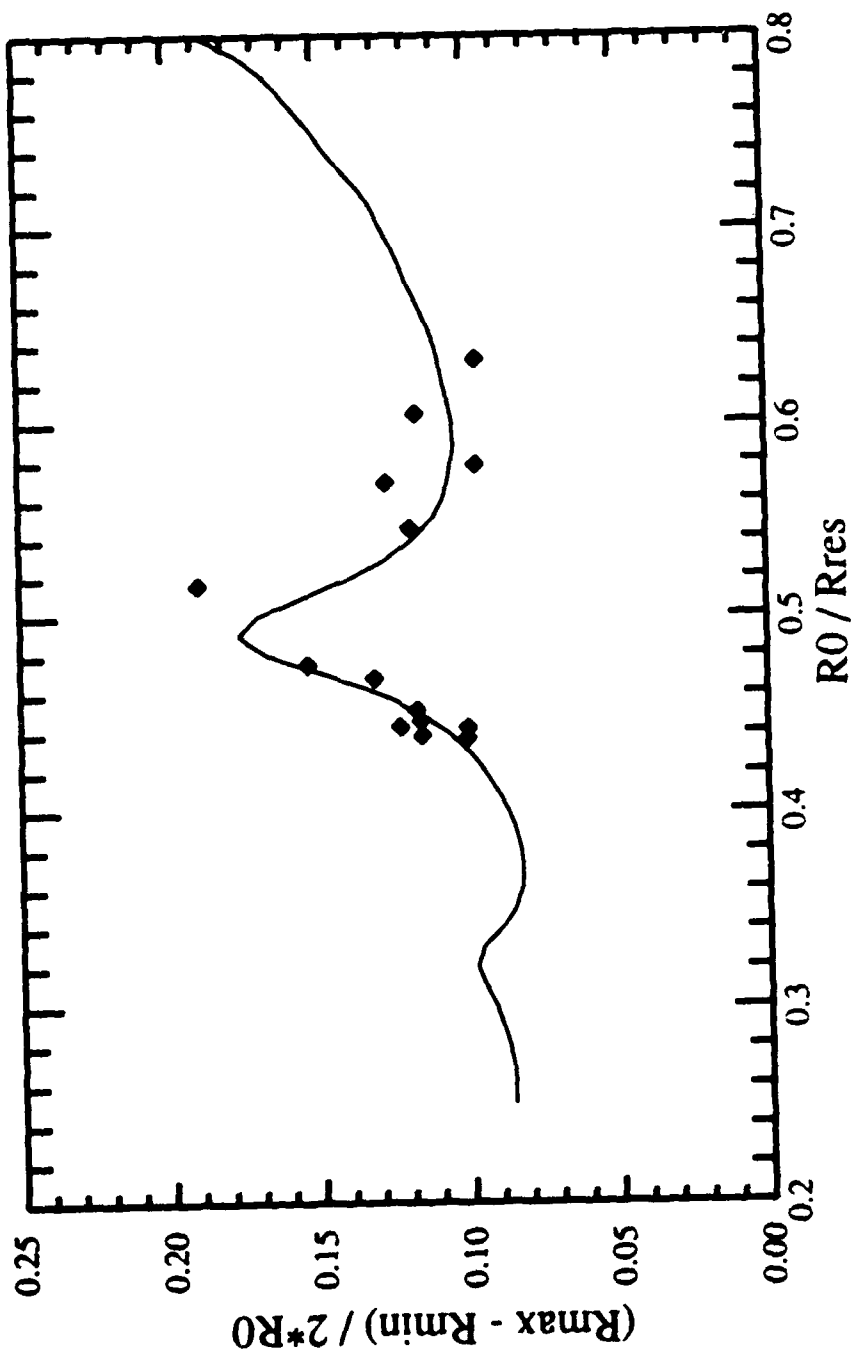


FIGURE J9

Resonance data and theory for $P = 0.24$ atm, $f = 24.4$ kHz.

III. A. 2. $R(t)$ analysis

a. Graphical presentation

The $R(t)$ results are presented in four-part graphs in order to minimize space. The upper left graph plots the driving pressure $P(t)$. The radius $R(t)$ is plotted in the lower left. The normalized Fourier power spectrum of $R(t)$ is plotted in the upper right. The grey-scale curve in the lower right is referred to as the continuous phase portrait. It depicts the motion in the classical mechanical phase space [68], assuming that the motion has only a single degree of freedom, corresponding to the radial coordinate for purely spherical motion. The discrete points in the lower right comprise the surface of section [14], sometimes called the Poincaré section, after the pioneering mathematician. For the particular case of a periodically driven dissipative system, the Poincaré section consists of those points $(R(t = nT), p(t = nT))$ in the R - p plane, where $n = 0, 1, 2, 3, \dots, N$. T is the period of the driving pressure, and N is the number of cycles of the driving pressure for which the operation is to be carried out. Thus, the periodicity of the motion can be deduced by merely counting the number of discrete points in the section, as long as noise and transient oscillations are absent.

III. A. 2. b. Radial oscillations

Figure 20 is the first in a series of five experimental $R(t)$ curves spanning the range $0.4 \leq R_0/R_{res} \leq 0.67$ of the second harmonic resonance for a constant driving pressure and

frequency. Figures 25-29 show $R(t)$ curves calculated numerically for the same parameters in Figs. 20-24 for comparison. Figures 30 and 31 show subharmonic responses.

Figure 20 presents the oscillation of a 51.5 μm bubble, below the second harmonic resonance. The amplitude of its response is only about 4%, and the trace is visibly noisy. This noise is apparent not only in the $R(t)$ curve, but also in the spectrum and the phase portrait. For clarity, the section points in Figs. 20-24 were averaged, since it was known *a priori* that the periodicity would be 1. Note that even away from the resonance there is a 2nd harmonic component in the spectrum. Figure 21 shows a 61 μm bubble, $R_0/R_{res} = 0.47$. The pronounced secondary collapse in the $R(t)$ response gives rise to a secondary loop in the phase portrait, the position of which is sensitive to the relative phase of the 2nd harmonic component.

As the bubble moves through resonance, the loop will rotate clockwise in the $R-p$ plane through approximately 180° . This phase shift is seen by Crum *et al.* in their levitation number studies, and is also predicted theoretically [25,26], where the phase of the component goes from 180° to 0° . Likewise, the section point in this region rotates counterclockwise through approximately 90° . This behavior seems plausible, since linear oscillation theory predicts a phase change from 0° to 180° as the oscillator is caused to go through its resonance [70]. Note also that the signal-noise ratio increases for increasing response.

Figure 22 shows a 64.2 μm bubble, oscillating near the peak of the 2nd harmonic resonance $R_0/R_{res} = 0.5$. Note the oscillation response has reached a maximum, and the $f/f_0 = 2$ spectral line is roughly equal in power to the fundamental. The harmonic loop has shifted further clockwise. Figures 23 and 24 show bubbles with $R_0/R_{res} = 0.54$ and 0.67 respectively. The 2nd harmonic component is decreasing as the bubble approaches the

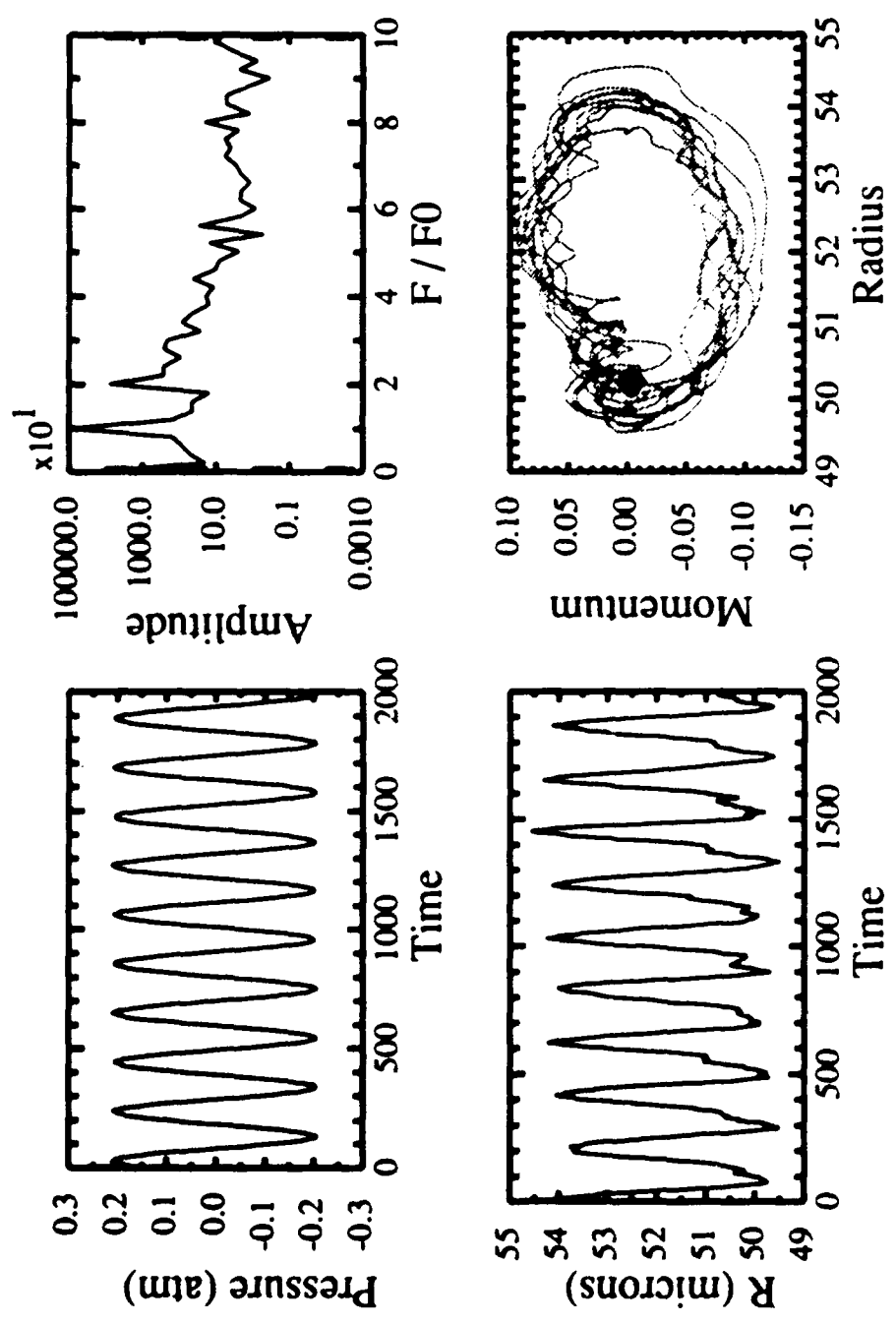


FIGURE 20

First of a series of figures showing radial response of bubbles of different equilibrium radius R_0 at the same pressure ($P = 0.21$ atm) and frequency ($f = 24.2$ kHz). Upper left plots the pressure vs. time, lower left plots radius vs. time, upper right plots the FFT of the R-t curve, and lower right is the continuous phase portrait with averaged Poincaré' section point. Here $R_0 = 51.5$ microns.

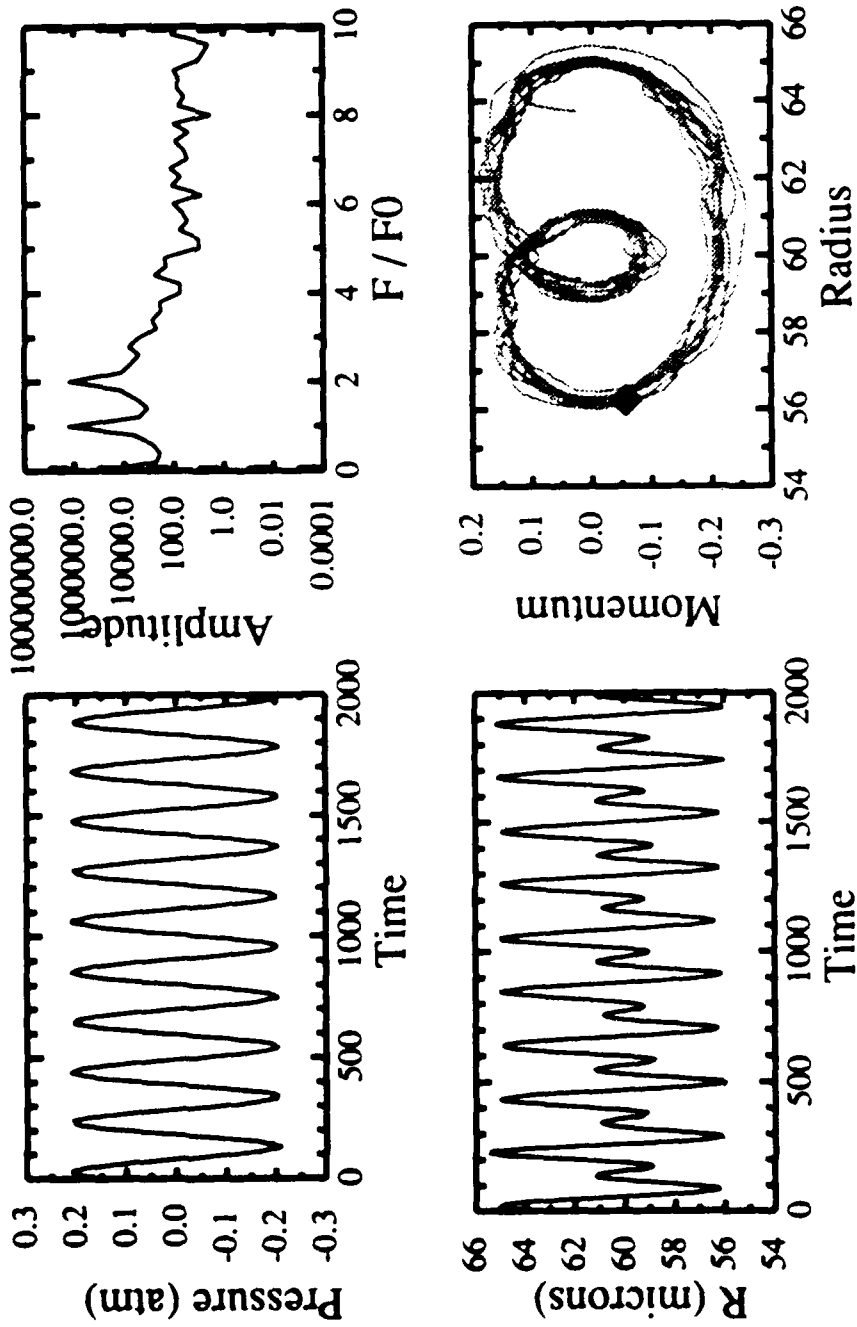


FIGURE 21

$R_0 = 61$ microns.

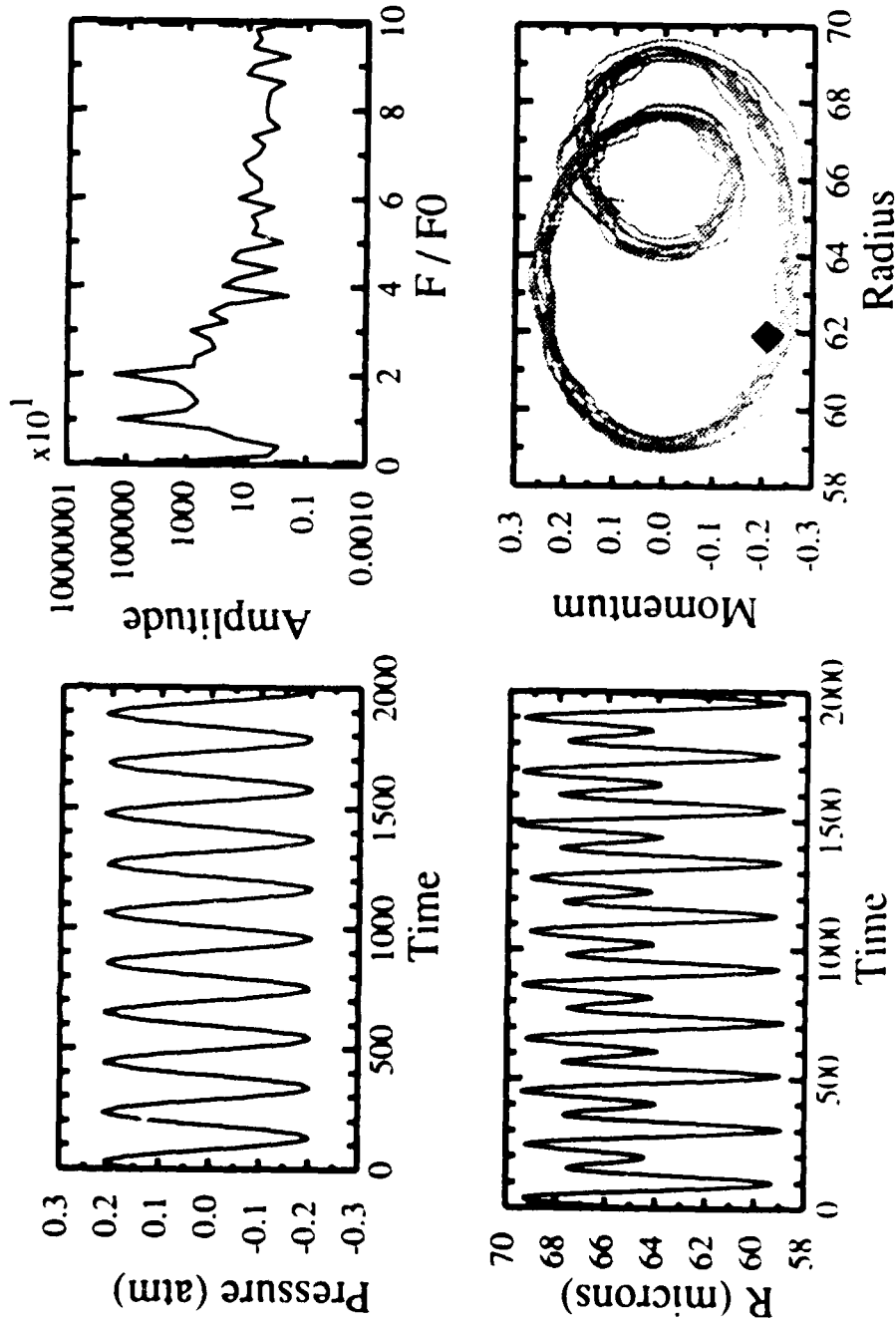


FIGURE 22

$R_0 = 64.2$ microns.

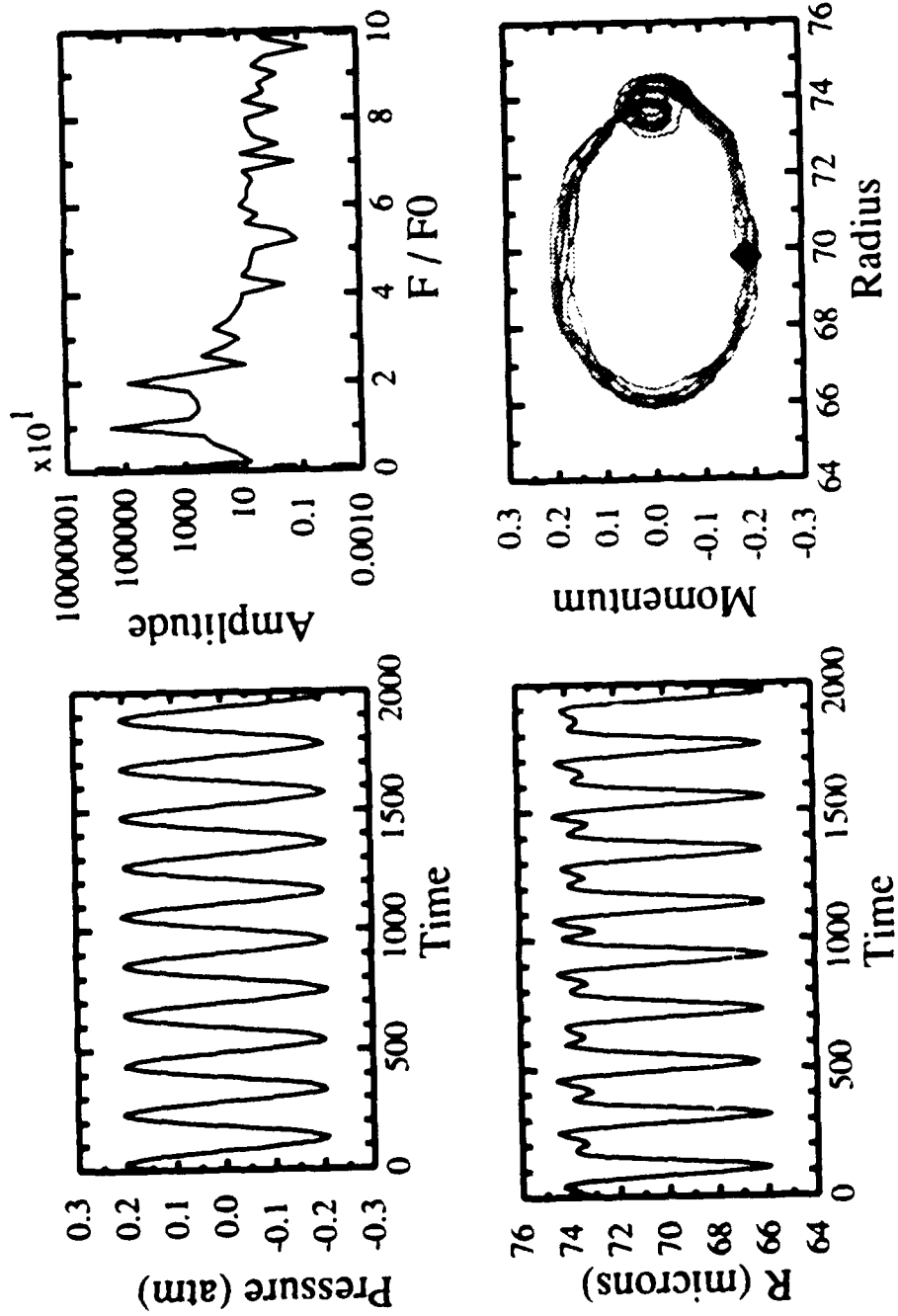


FIGURE 2.3

$R_0 = 70.0$ microns.

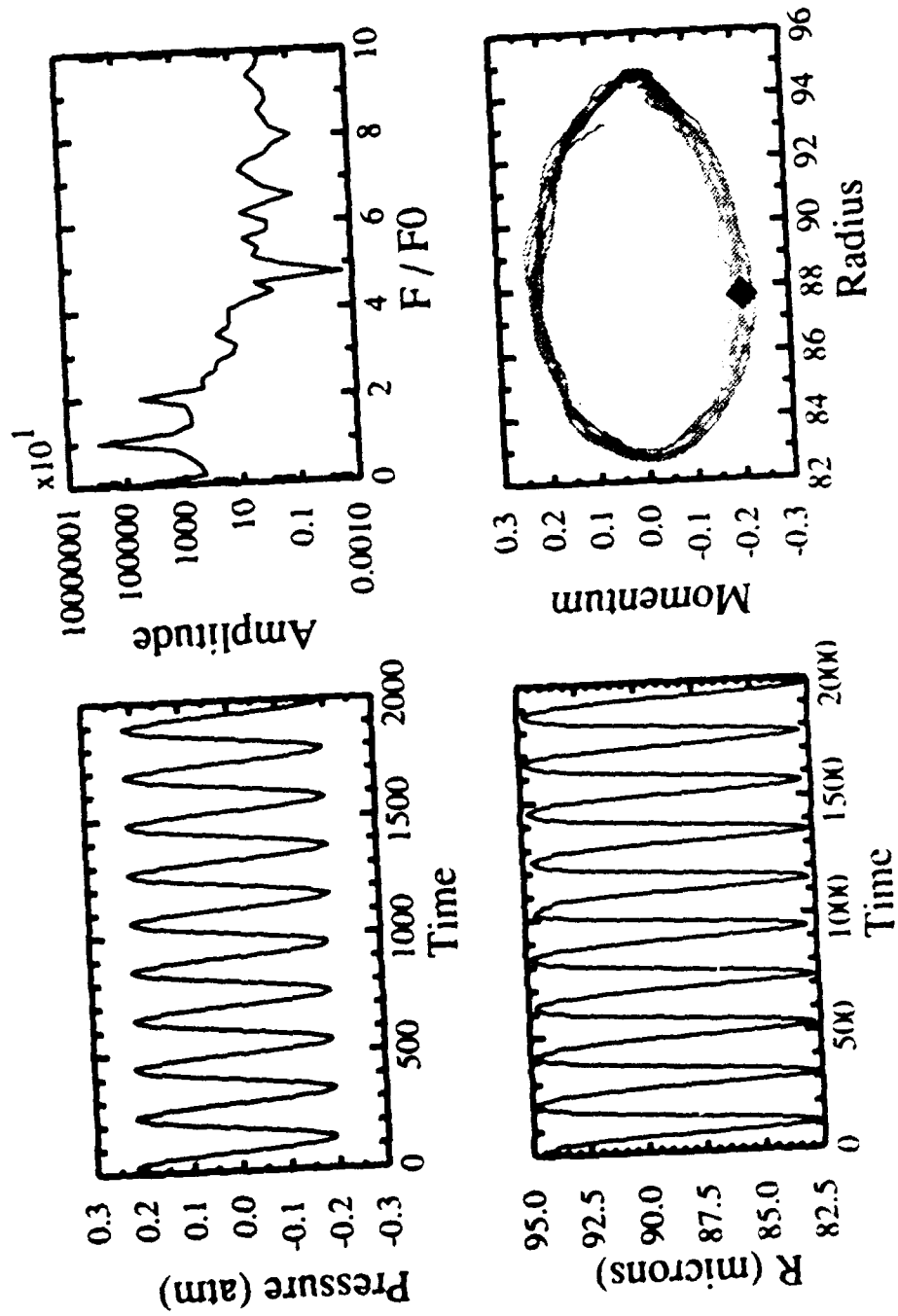


FIGURE 24

$R_0 = 89.0$ microns.

main resonance, and the loop actually disappears in the phase portrait, although there remains a spectral component at $f/f_0 = 2$.

Figures 25-29 are the theoretical analogues of Figs. 20-24. The relevant equations (2), (4), and (5) were integrated to generate $R(t)$. The data sets thus generated were then analyzed using the same algorithms used on the experimental data sets. In general, the same features are seen, such as the appearance of the second harmonic response and the rotation of its loop in the phase plane, and the counterclockwise rotation of the section point (even though the absolute position of the point is different).

Some differences are apparent, however. First, there is obviously no noise on the theoretical curves, and it is easier to resolve higher harmonic components in the spectrum (up to $f/f_0 = 8$). Second, the magnitude of the 2nd harmonic oscillation is noticeably (both in the spectrum and the phase space) smaller than the experimental values. This same phenomenon is seen in a different way in Figs. 14 and 16. There, it was the maximum response at resonance that was underestimated by theory. This is essentially the same problem as that previously encountered for the 2nd harmonic response in comparing the results of an earlier theory with data taken by Crum [69]. The theory overestimated the value of the nonlinear damping in the 2nd harmonic region. It seems apparent that the current theory, though better accounting for the thermodynamics of the bubble interior, also overestimates the nonlinear damping. Certainly, more data of this type need to be taken to quantify the discrepancy.

Figures 30 and 31 present subharmonic radial responses for two bubbles with $R_0 = 88 \mu\text{m}$, with the base frequency of the response being $f/2$. $R_0/R_{res} = 0.66$ for both bubbles, corresponding to a non-resonant solution for steady-state conditions at the pressure of 0.25 atm, according to Fig. 1. These figures are a little more difficult to

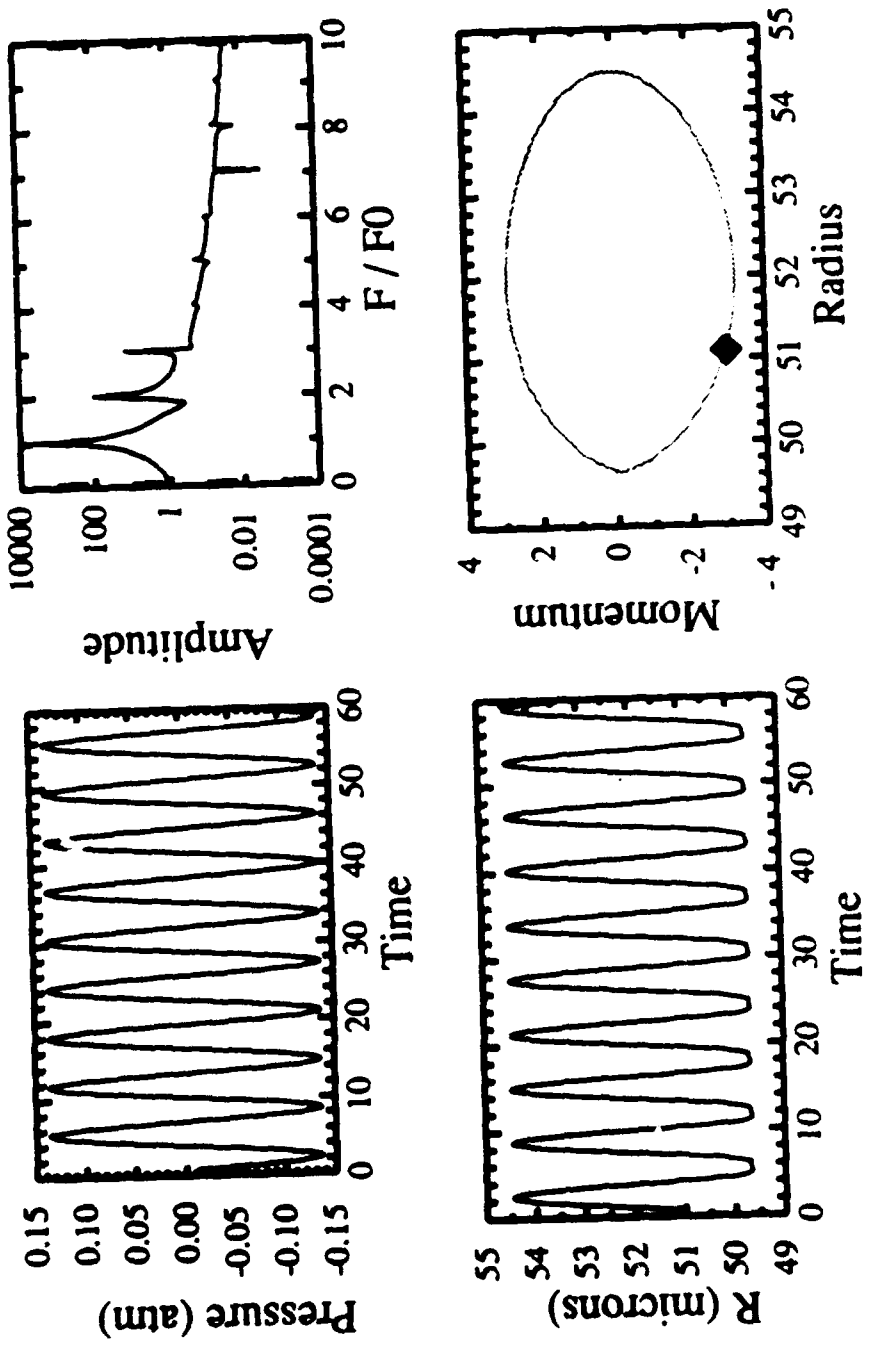


FIGURE 25

First of a series of numerical results showing radial response of bubbles for the same parameters as the experimental results of figures 20 - 24. (The pressure here is a rms value; the peak value is 0.21, the same as the experimental graphs). $R_0 = 51.5$ microns, corresponding to figure 20.

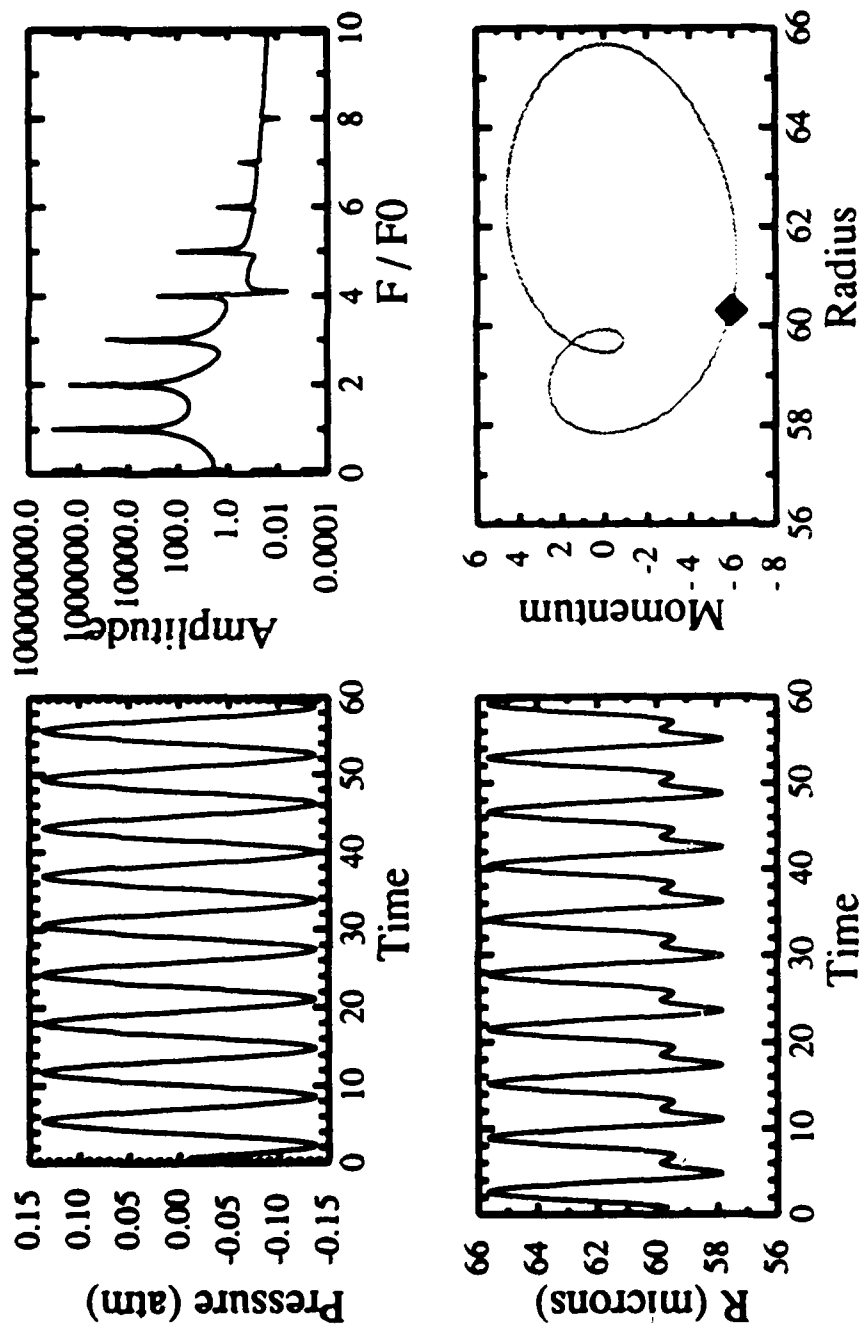


FIGURE 26

Ro = 61 microns, corresponding to figure 21.

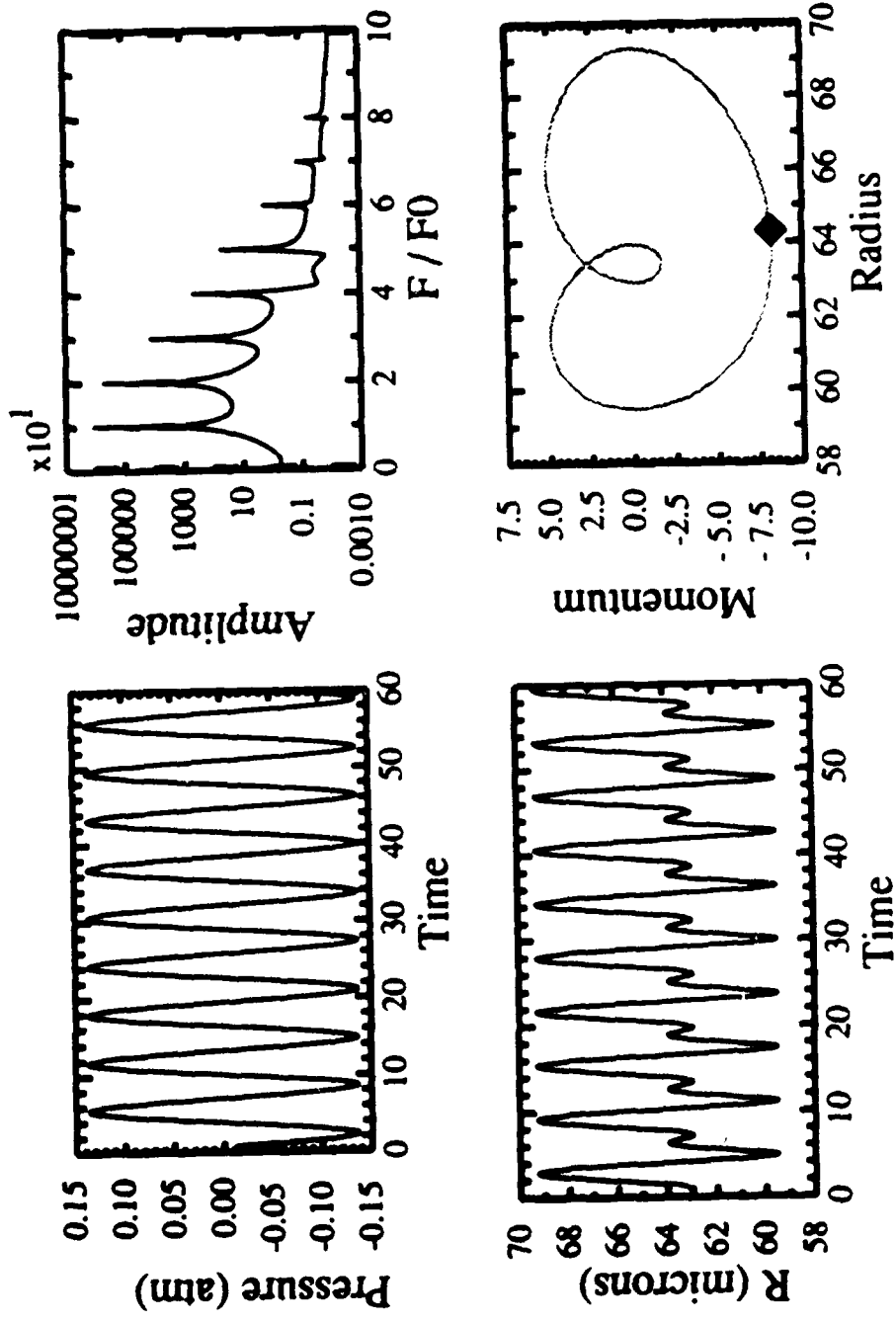


FIGURE 27

$R_0 = 64.2$ microns, corresponding to figure 22.

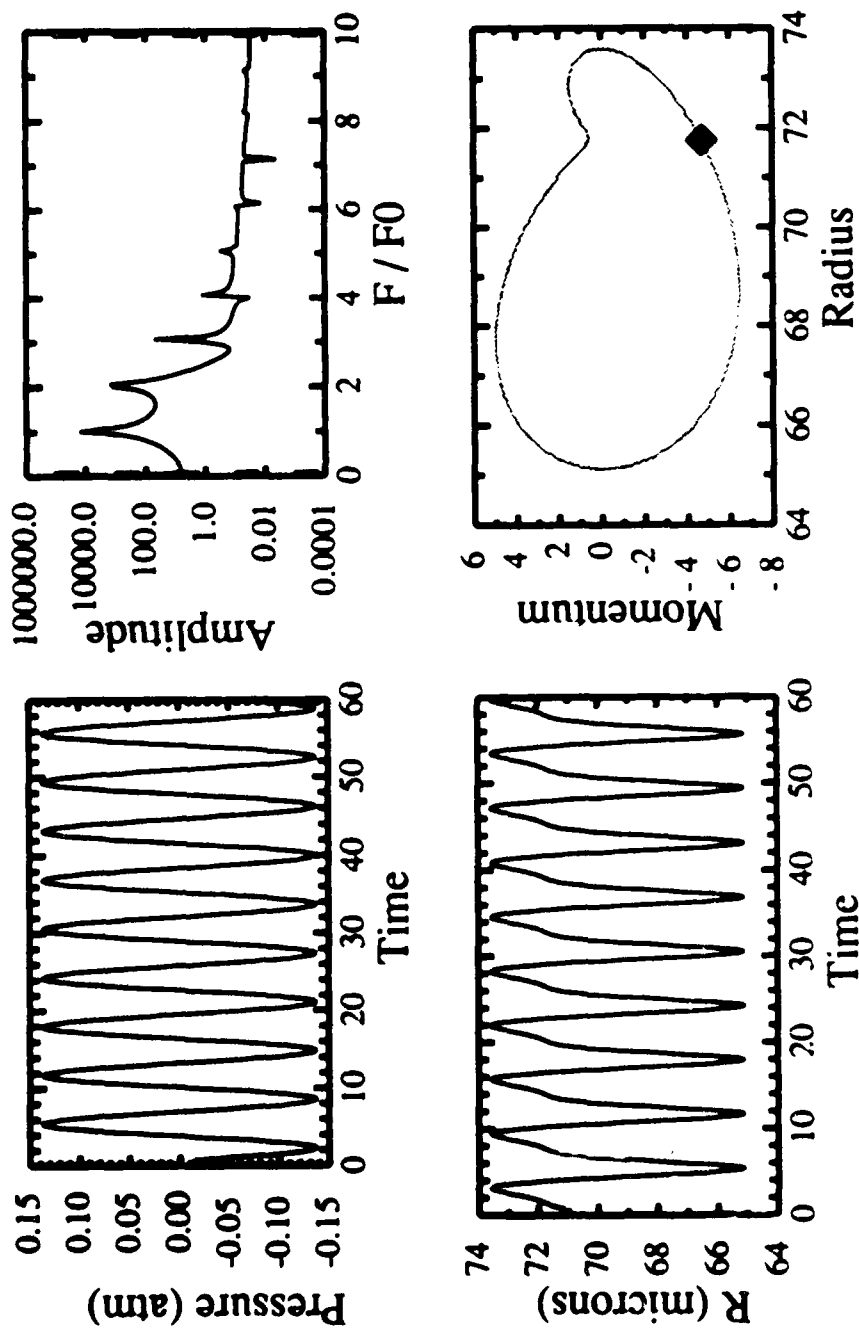


FIGURE 28

$R_0 = 70.0$ microns, corresponding to figure 23

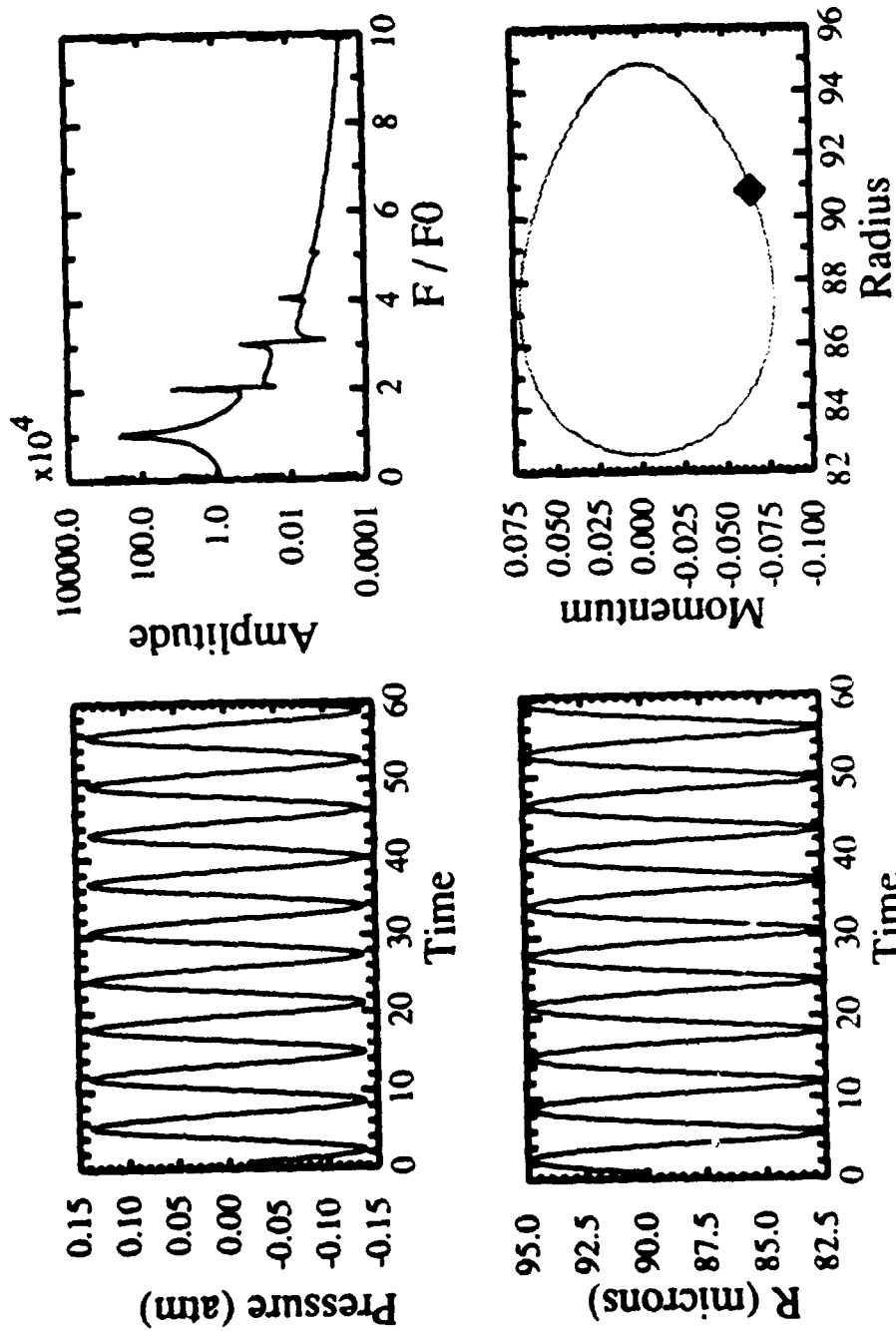


FIGURE 22

$R_0 = 89.0$ microns, corresponding to figure 24

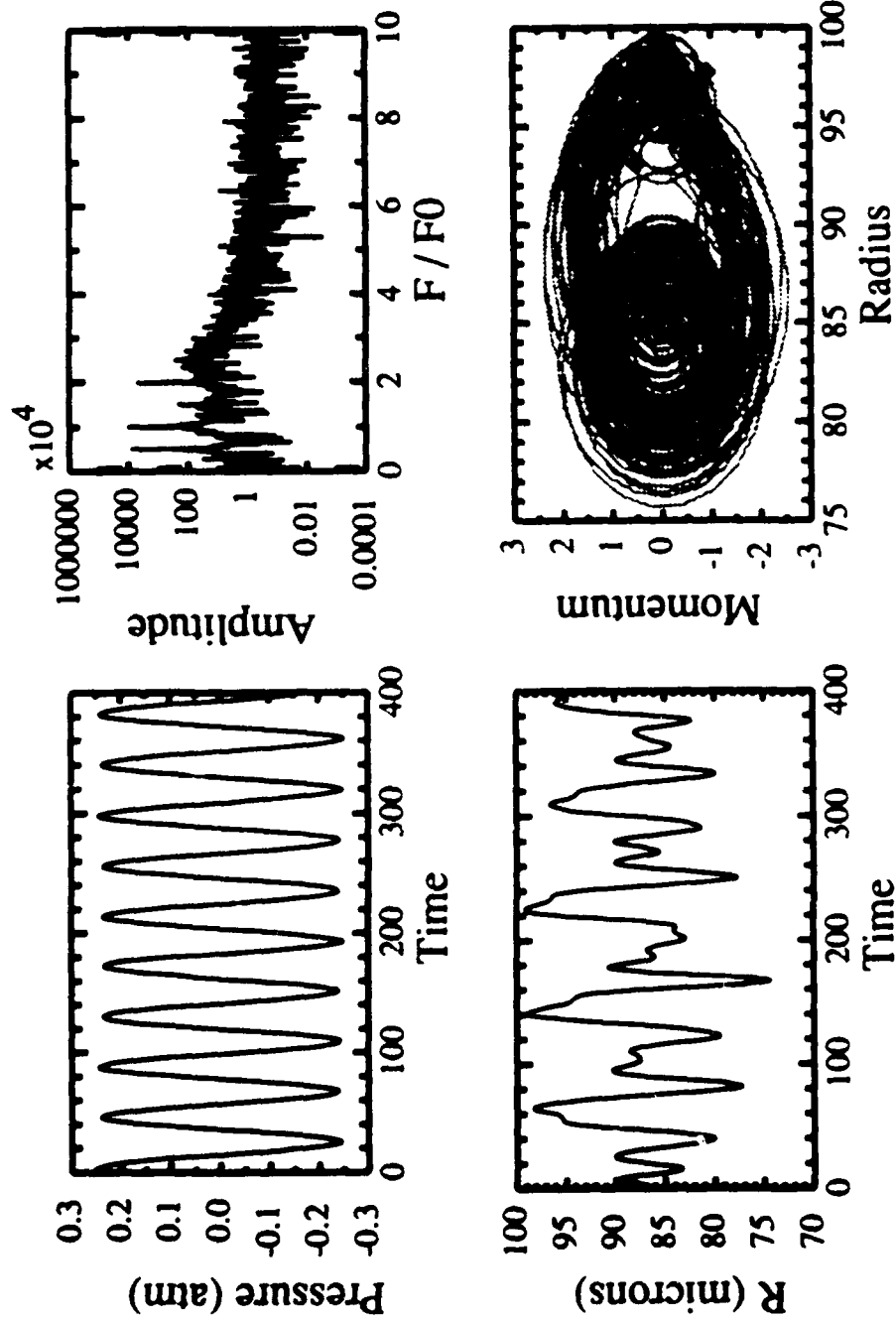


FIGURE 30

Data taken with the Ortel photodiode and the Ar-I 488.0 nm line. $R_0 = 88.5$ microns, $f = 23.8$ kHz.

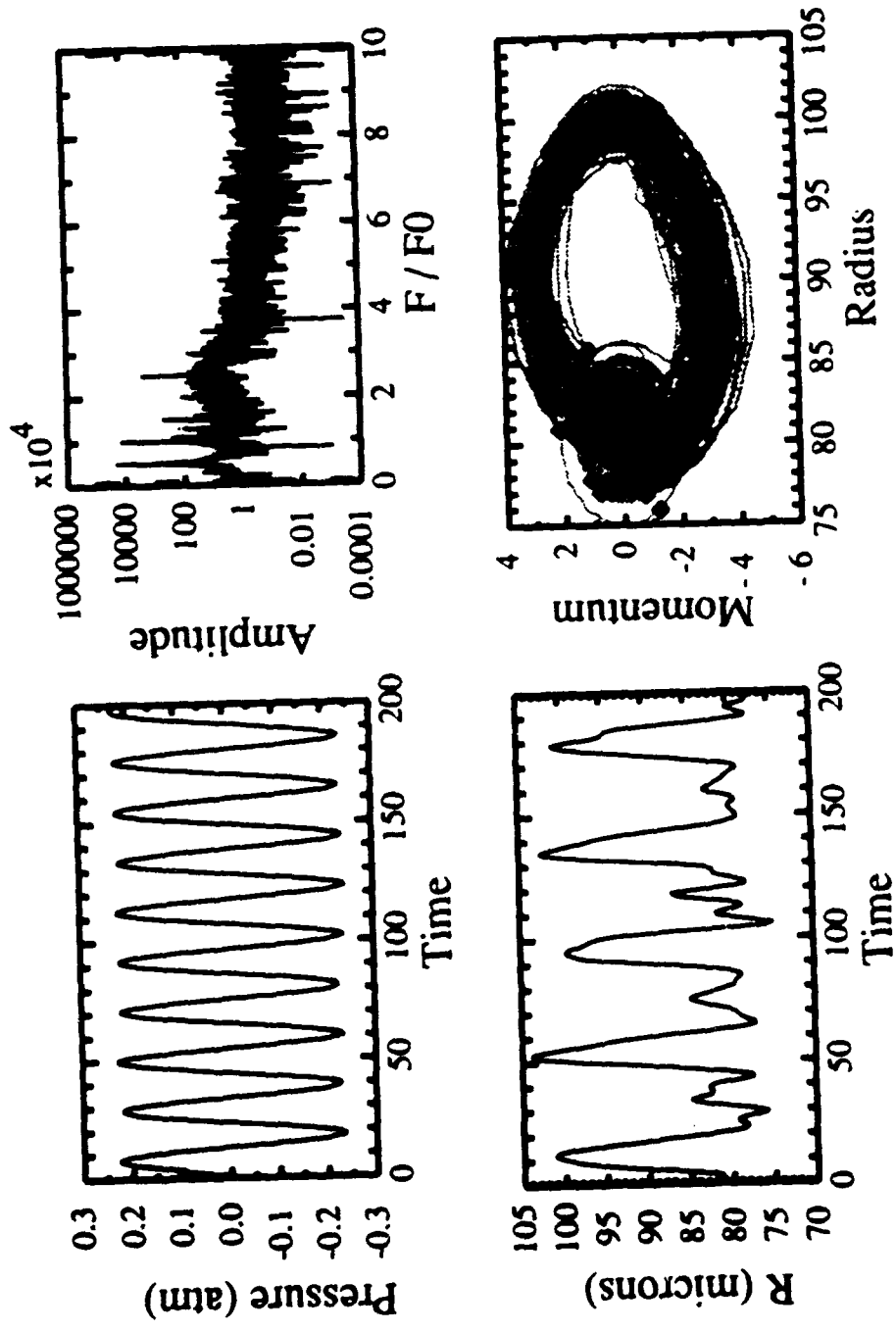


FIGURE 31

Data taken with the Oriol photodiode and the Ar-I 488.0 nm line. $R_0 = 87.5$ microns.
 $f = 23.8$ kHz.

interpret, since the averaging technique was not employed due to the relatively short period of existence of the oscillations. Thus, the presence of noise complicates the analysis. The broad peak at $f/f_0 = 2.5$ is due to electrical noise. This noise was present in every data set taken, but averaging reduced the height of the peak to the noise floor of the spectrum, an indication of the random phase of the origin of the noise peak. The spectral lines at $1/2$, 1 , $3/2$, 2 , and $5/2$ are clearly visible, and relatively sharp, indicating that there is probably nothing chaotic about $R(t)$, regardless of the appearance of the $R(t)$ curves. The phase portraits are smeared over a relatively large region, and the section points also show some scatter, although it is apparent that the periodicity is two. The smear is most likely due to the noise.

The procedure used to obtain these two curves was slightly different than that used for Figs. 20-24, and bears mentioning. A bubble was obtained, oscillating stably at the parameter values indicated. The pressure was then incremented slightly ($<1\%$) upwards until the period-doubling was seen. Typically, the subharmonic oscillation would decay into the previous singly-periodic oscillation within a few seconds, indicating that the period-two oscillation was a transient. The pressure was "bumped" in this fashion until the subharmonic oscillation lasted approximately 30 seconds ($\approx 6 \times 10^5$ cycles, a long-lived transient!), and then $R(t)$ was digitized and stored. Attempts to get the oscillation to remain stable for longer periods of time were thwarted by the onset of noticeable shape oscillations, followed by rapid growth and breakup of the bubble.

III. B. Complex motion

1. Introduction

The observation of complicated $I(t)$ behavior necessitated some rethinking about the best way to analyze and present the data. "Complicated" implies that the $I(t)$ trace exhibits high or no periodicity, multicomponent and/or broadband spectrum, and may not be the result of purely radial motion. This complex motion could be "chaotic", that is, the complexity is generated via certain universal nonlinear mechanisms from only a few (or one) degrees of freedom [76,77], or it could be "stochastic", deriving from the contributions of many degrees of freedom.

The first resort was the FFT calculation to give the power spectrum, some results of which are presented in section 2. The spectrum gives information concerning frequency components, but sheds no light on the source of the spectral lines. Indeed, if interpreted traditionally, the broadband spectra would require the conclusion of stochastic behavior of a bubble, where stochastic is defined above. This is contrary to numerical results for bubble models [29-31,40], which show that just the single radial degree of freedom can give rise to a broadband spectrum.

The problem was, given a single-variable time series, how could more information about the underlying dynamics be extracted? In some cases, the methods of phase space analysis and phase space reconstruction provided some insight into the motion. They are described in section 3, along with the results of the application of the analysis to complex $I(t)$ data sets.

III. B. 2. Fourier analysis

Figure 32 shows a subharmonic shape oscillation with a basic frequency $f/2$, usually referred to as a period-two response. The FFT spectrum looks qualitatively similar to the subharmonic radial results of Figs. 30 and 31. In fact, nothing in this case (other than *a priori* observational knowledge) indicates the presence of shape oscillations. This and the other graphs that follow are uncalibrated results, and hence the units for relative intensity are arbitrary.

Figure 33 shows a period-four ($f/4$ basic frequency) response. Again, since this is a perfectly reasonable result in terms of the universality of period-doubling cascades in single degree of freedom systems [76,77], the visual observation of precession is the only confirmation of the presence of shape oscillations. Interestingly enough, this could belong to the *first* period-doubling of the $f/2$ shape oscillation, although preliminary experiments indicate that simple period-doubling cascades will be difficult to observe in any case.

Figure 34 shows an oscillation with a strong $f/16$ component, but also with numerous intermediate peaks indicating either chaotic motion or higher dimensional (higher degree of freedom) behavior, although the motion is still apparently smooth and near-periodic.

While perhaps not the worst-case scenario, since there was no translational motion, Fig. 35 does serve as an example of the potential of a bubble to exhibit very complex dynamical behavior. Not only does the spectrum show broadband behavior, but also the local maxima discernible seem to bear no relationship to the fundamental. Clearly, more information or better analysis of existing information is needed to determine more about the dynamics.

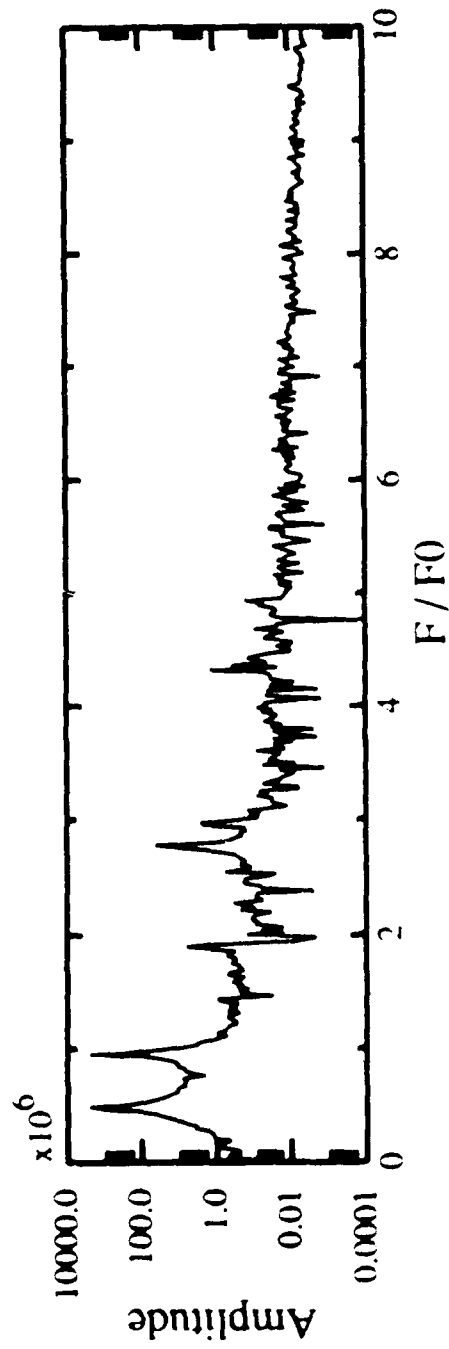
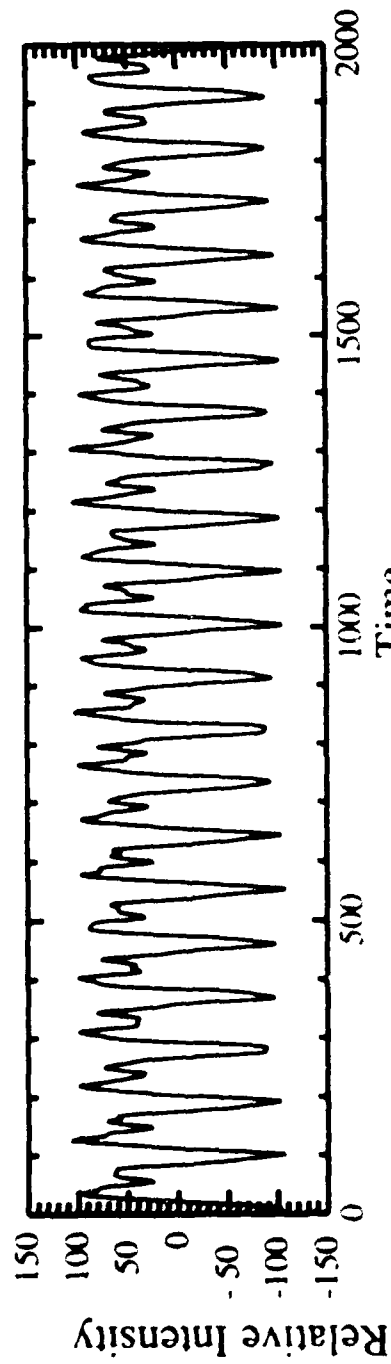


FIGURE 32

Scattered intensity as a function of time for the RCA photodiode/lens combination. The HeNe 632.8 nm line was used, with $f = 24.5$ kHz, P is unknown, and $R_0 = 70$ microns.

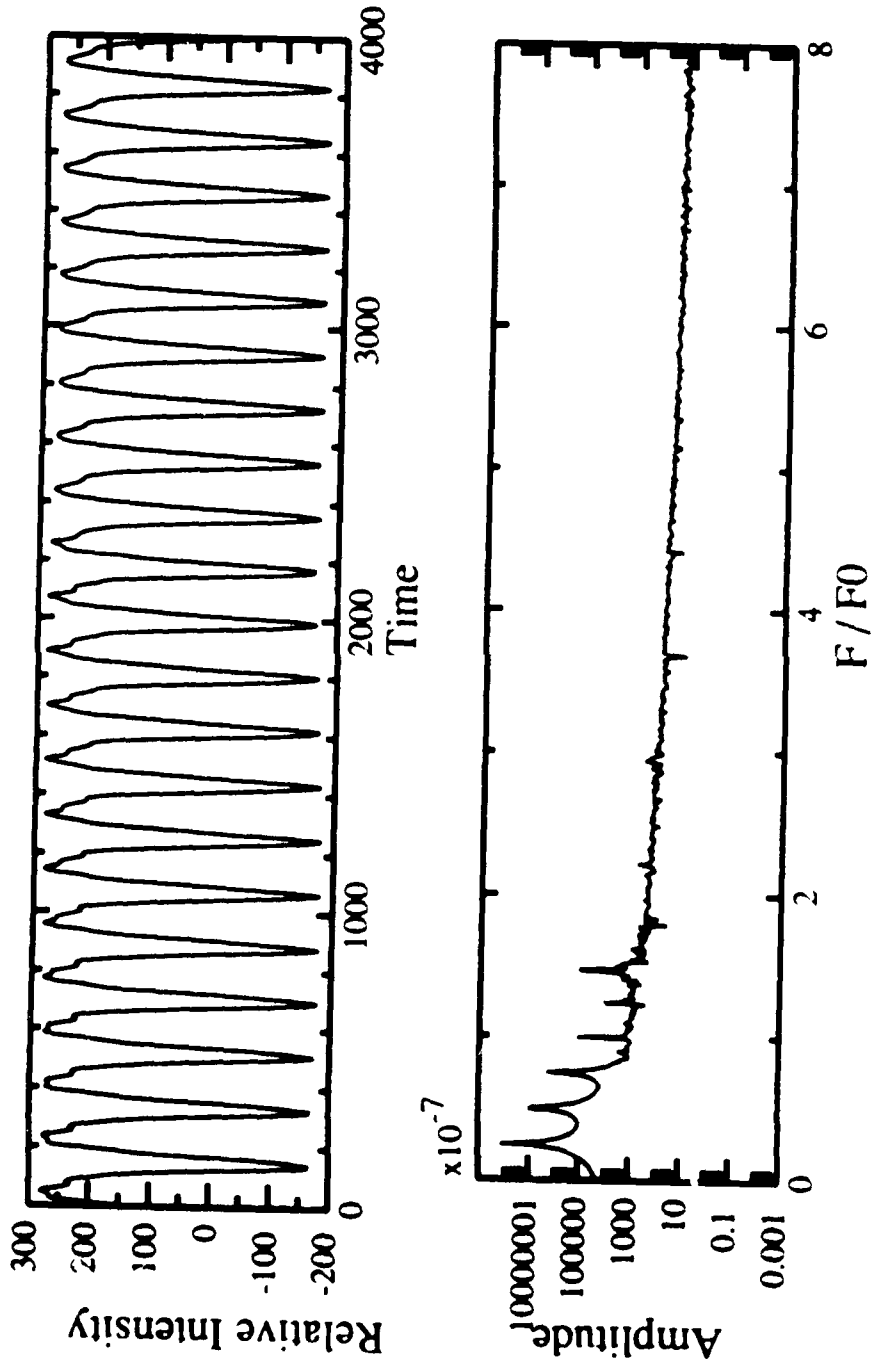


FIGURE 33

Scattered intensity as a function of time for the RCA photodiode/lens combination. The HeNe 632.8 nm line was used, with $f = 24.5$ kHz, P is unknown, and $R_0 = 80$ microns.

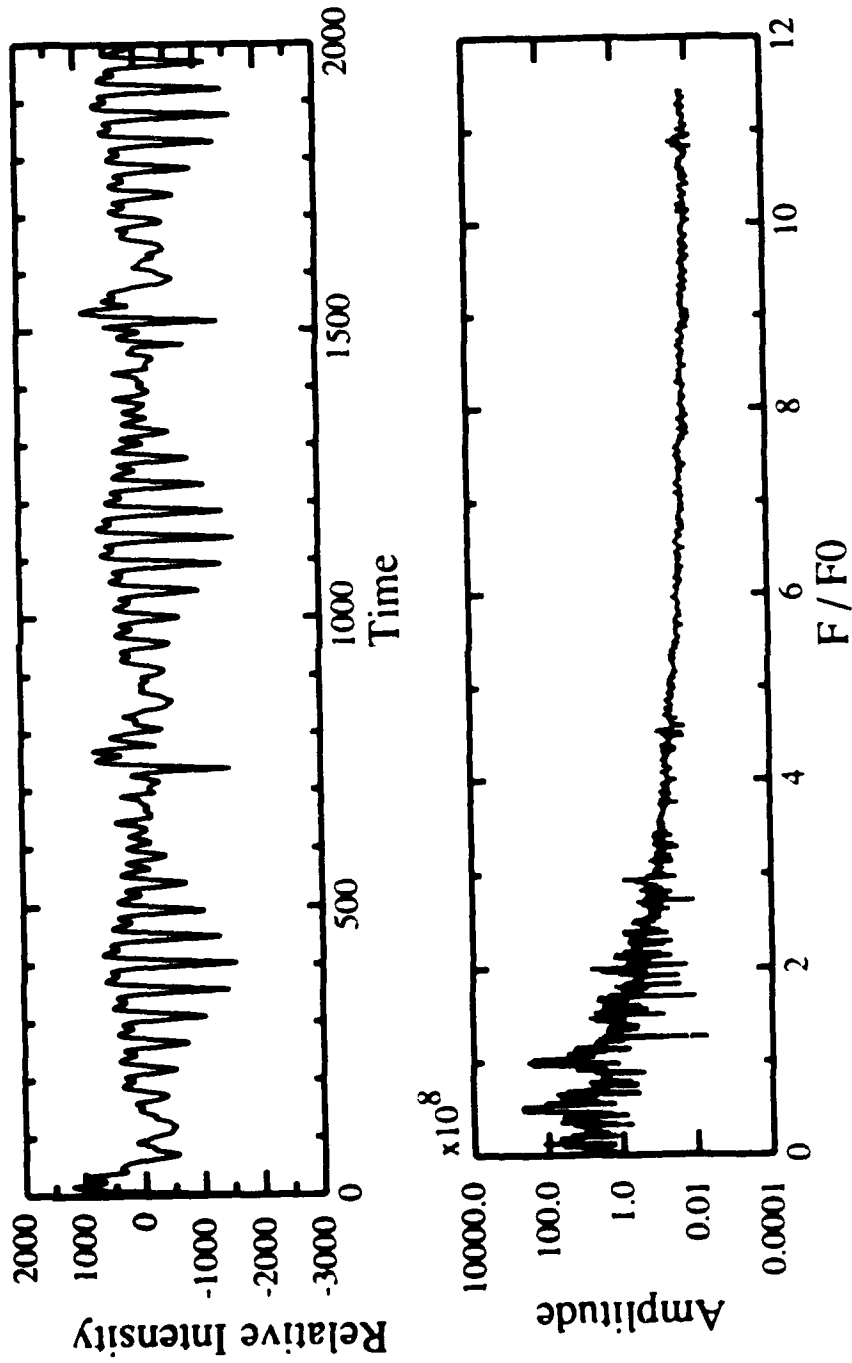


FIGURE 34

Scattered intensity as a function of time for the RCA photodiode/lens combination. Wavelength in the bubble is 632.8 nm, $f = 24.5$ kHz, P is unknown, and R_0 approximately 80 microns.

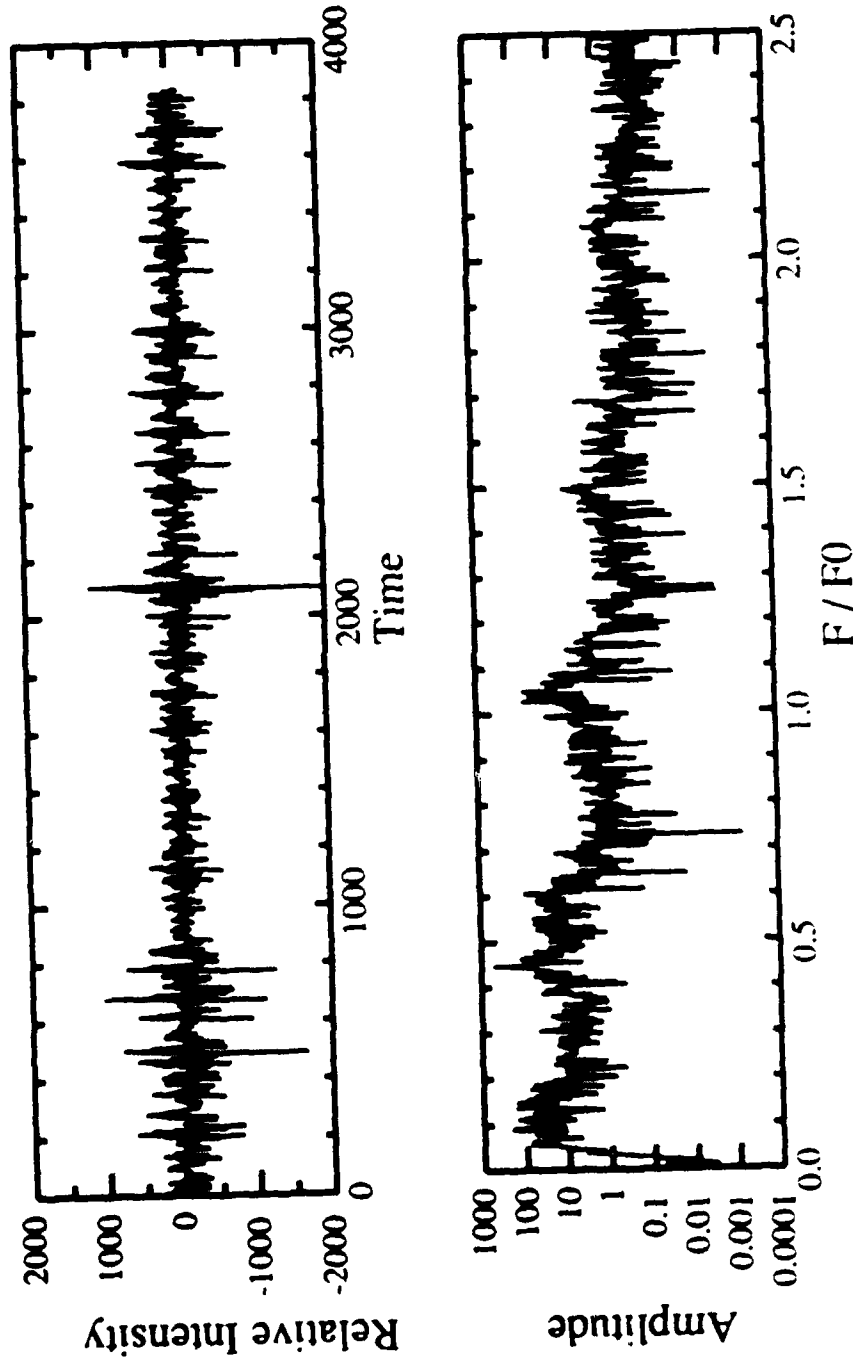


FIGURE 35

Intensity vs. time for the Thorn EMI photomultiplier centered at 66 degrees and the He/Ne laser. Bubble size is approximately 90 microns, $f = 24.6$ kHz, and the pressure is unknown.

As a final spectrum example, Fig. 36 depicts a somewhat less radical departure from simple periodic motion. Observationally, there was no apparent shape oscillation, although the pressure was well beyond the theoretical threshold for the onset of shape oscillations [37]. A dominant $1/2$ line is seen, as well as resolution of peaks as high as $f/f_0 = 5$. For various reasons, not the least of which was a strong hunch, the data in Fig. 36 provided a good test case for application of methods of phase space analysis, as outlined in the next section.

III. B. 3. Phase space analysis

Figure 37 plots the continuous phase portrait in the lower right, and the Poincaré section in the lower left for the data set (same as Fig. 36) shown at the top. The bounded, plane-filling nature of the continuous phase portrait make it a good candidate for a strange attractor [14], but (although there is evidently structure) the plane-filling nature of the section argues for the consideration of higher modes contributing to the motion [78]. The implication is that, for whatever reason, the $2N$ -dimensional (N is the number of degrees of freedom, and the notion of an N -dimensional *state* space is useful here) *phase* space needed to describe the motion of the system point is, in this instance, greater than 2. More to the point, the number of degrees of freedom N needed to describe the motion is at least greater than one, and the graphs in Fig. 37 are merely projections into a plane of the true attractor in the full phase space.

The problem then becomes one of eliciting the other independent coordinates when only one variable has been measured. A powerful method for yielding the intrinsic degrees of freedom has been developed by Grassberger and Procaccia [73] based on a result by

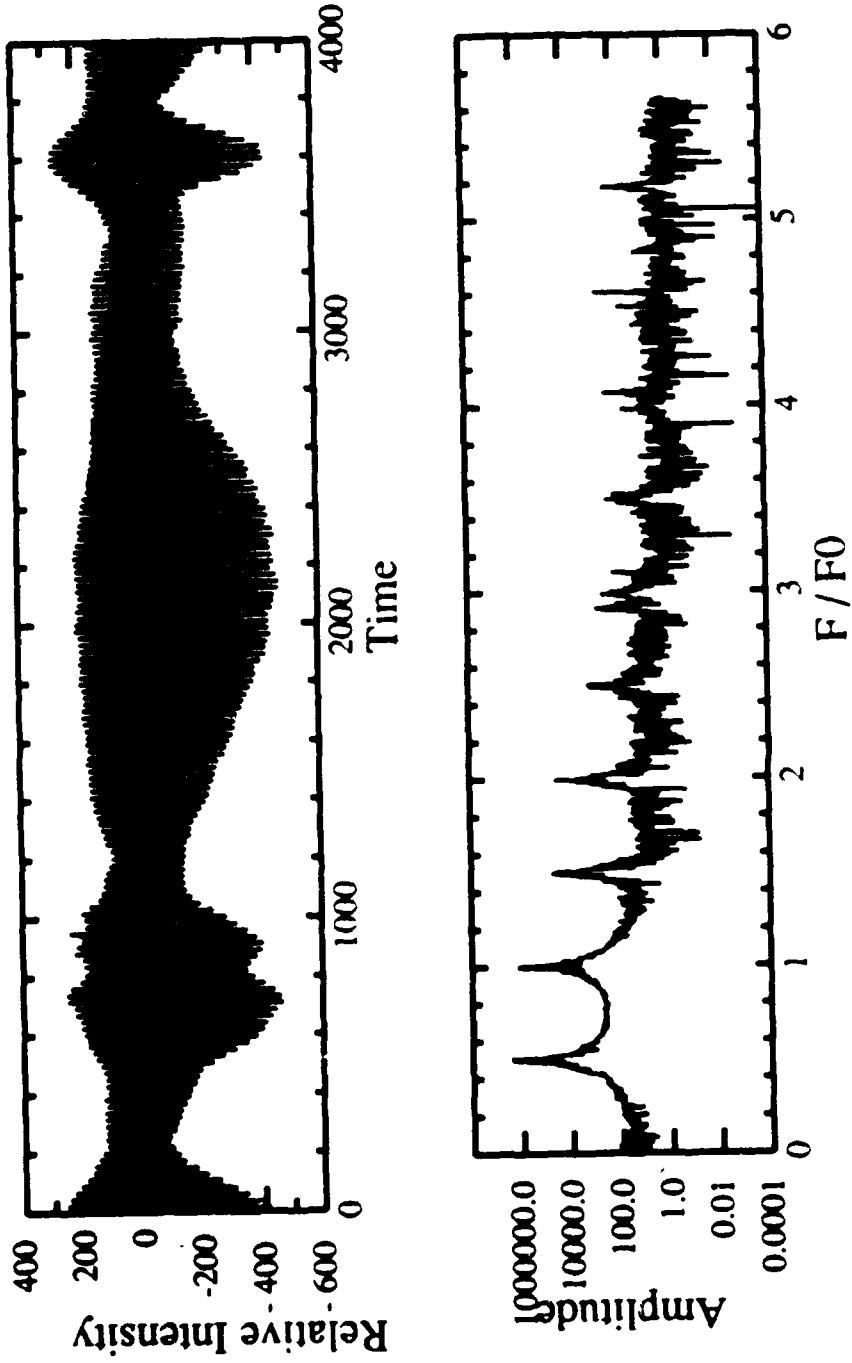


FIGURE 36

Intensity vs. time for the RCA photodiode/lens combination centered at 70 degrees with the He-Ne laser. Bubble size is approximately 90 microns, $f=24.5$ kHz, and the pressure is unknown.

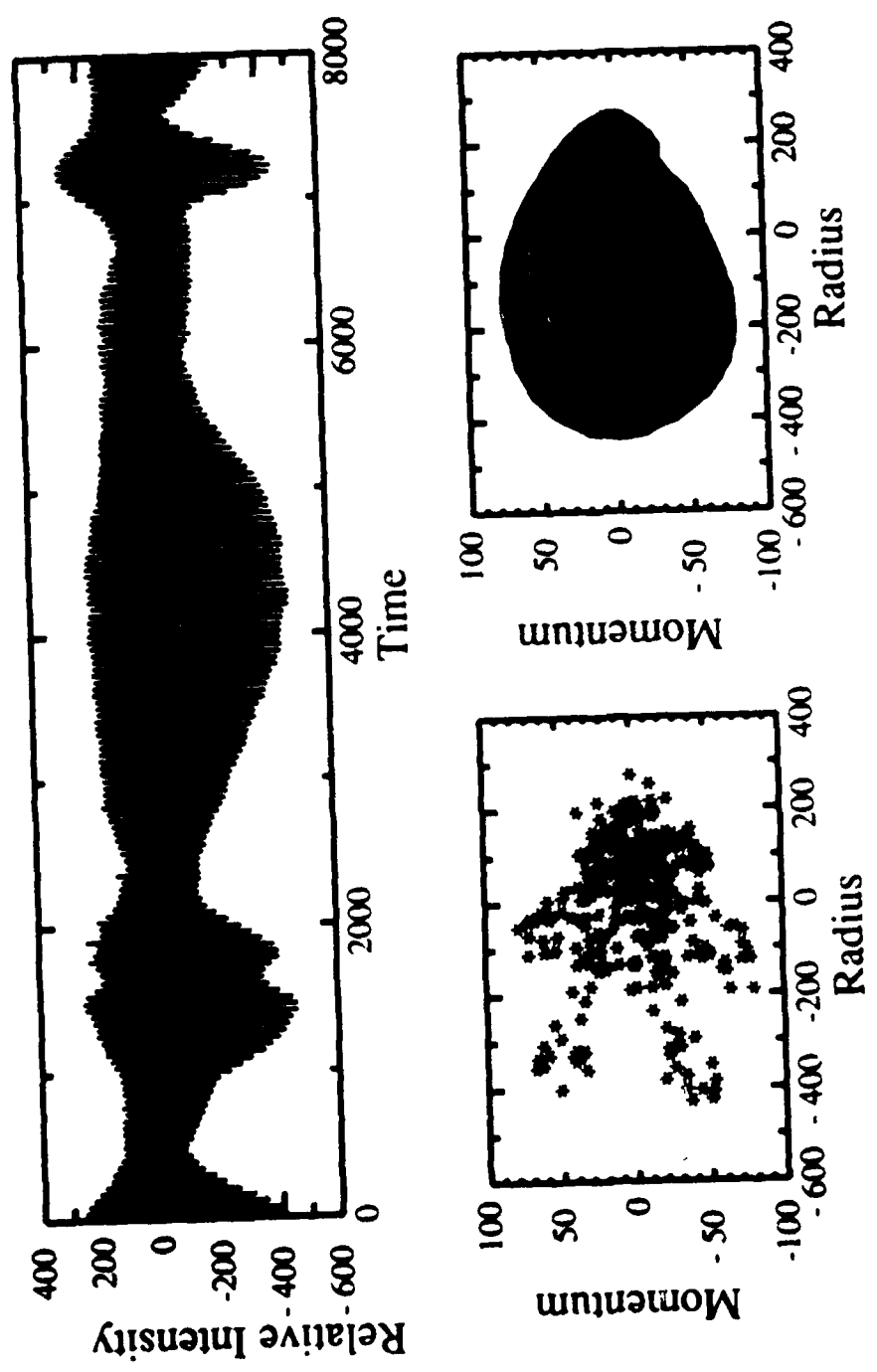


FIGURE 37

Continuous phase portrait and Poincaré section projections for data in figure 36

Takens [74] and Packard *et al.* [75]. It involves calculation of a "spatial correlation integral" whose power-law behavior is used to estimate the "correlation dimension" D_2 of the attractor, which is usually interpreted as a measure of the effective number of degrees of freedom of the system. The particular implementation used is a modification of the method of Grassberger and Procaccia due to Theiler [79], and is better equipped to handle autocorrelated data.

The data to be analyzed are in the form of a time series of relative intensity values $I_{exp}(kt_s)$, $k = 1, \dots, N$, where the sampling time t_s is typically $1 \mu\text{s}$, and the number of data points N varied from a minimum of 8192 to a maximum of 16384. For the reconstruction of the state space, Takens suggested creating a set of m -dimensional vectors v_k whose components are the time-delayed values of the intensity: $v_k = \{I_{exp}(kt_s), I_{exp}(kt_s + T), I_{exp}(kt_s + 2T), \dots, I_{exp}(kt_s + (m-1)T)\}$. An optimal choice for the time delay T is the time t_0 of the first zero of the autocorrelation function of the data. This ensures the independence of the basis (or Takens) vectors v_k .

For $T, m \ll N$, there are almost as many vectors v_k as there are data points. Thus, the temporal dynamical information in the one-dimensional data has been "converted" to spatial information in the m -dimensional set [79]. Takens proved that the metric properties of the reconstruction v_k in the m -dimensional embedding space are the same as the original (unknown) attracting set in the original phase space of the system generating the time series. For m sufficiently large, a system possessing a D_2 -dimensional attractor in its phase space will have its Takens vectors v_k lying on a D_2 -dimensional subset of the embedding space \mathcal{R}^m .

The designation D_2 indicates that the correlation is not the only dimension-type measure available for analyzing complex time series. Indeed, D_2 is but one member of an

infinite-dimensional set D_q of averaged, coordinate-invariant numbers termed "generalized dimensions" [80-82] by which different motions can be distinguished.

To find D_2 , Grassberger and Procaccia [73] introduce the spatial correlation integral $C(r, N) = 1/N^2 \times$ [the number of pairs (i, j) for which $|v_i - v_j| \leq r$], where r is the edge length of an m -dimensional cube. Following Theiler [79], a slightly modified correlation integral was actually calculated

$$C(r, N, W) = \frac{2}{N^2} \sum_{n=W}^N \sum_{k=1}^{N-n} H(r - |v_{k+n} - v_k|) \quad (25)$$

where H is the Heaviside step function, and $W=1$ corresponds to the original Grassberger-Procaccia formulation [73]. This was done in order to avoid problems associated with autocorrelated data. It was necessary because the actual calculations were performed using an optimized algorithm obtained from Theiler [83], where the delay time T was fixed and equal to 1. To "decorrelate" the data, W was chosen to be > 10 .

In the small r limit $C \approx 0$, since there will be a non-zero lower bound for the distances $|v_{k+n} - v_k|$. For r large $C \approx 1$ (normalized to N^2), since all the computed distances will be less than r . For sufficiently large m and N , $C(r, N, W)$ should scale as a power of r for intermediate values of r : i.e.,

$$C(r, N, W) \propto r^{D_2} \quad (26)$$

C in this case can be thought as some generalized volume of the reconstructed attractor, hence the interpretation of D_2 as a dimension.

Numerical calculations for C were carried on a pair of MS-DOS machines, a Tandy 3000 with a 80286 CPU and a Compaq Deskpro 386 running an 80386 CPU. A typical calculation of the array (r,C) for $N = 16,000$, $1 \leq r \leq 1200$, and $m = 20$ took 42 hrs on the Tandy, and 20 hrs on the Compaq. A prototype version is in development for use on the CYBER 205, which should significantly reduce run-time, which has been a bottleneck in the data analysis.

To find the scaling region the following procedure is used: $C(r,N,W)$ is calculated for a large range of r , for some initial guess at m , which is always chosen greater than the suspected dimension of the attractor. Then $\ln(C(r,N,W))$ is plotted vs. $\ln(r)$, and a slope is sought for intermediate r . If C scales as eq. (26) suggests, then there should be an apparent linear region in the log-log plot, with the slope = D_2 . If no scaling region is observed, then m is increased, and the process repeated, until a scaling region is found. If no scaling region is found, then little can be said about the motion, except that it is probably high-dimensional.

Figure 38 plots $\ln(C(r,N,W))$ vs. $\ln(r)$ for the data in Figs. 36 and 37, for embedding dimensions $m = 4, 8, 12, 16$, and 20. An obvious linear scaling region is seen for intermediate r for $m \geq 12$. Figure 39 expands the scaling region of Fig. 38. A best-fit slope was calculated to estimate D_2 for each of the embedding dimensions used, and the results are shown in Fig. 40 as a function of m . D_2 levels off at about 3, indicating that at least 3 independent variables are needed to describe this motion. What these variables could be is discussed in chapter IV.

Figure 41 shows a data set similar to Fig. 35, with a broadband spectrum. Figure 42 is a phase space projection of the data. Things are pretty messy, and not much can be said about the motion. Figure 43 shows $\ln(C(r,N,W))$ vs. $\ln(r)$ for increasing values of

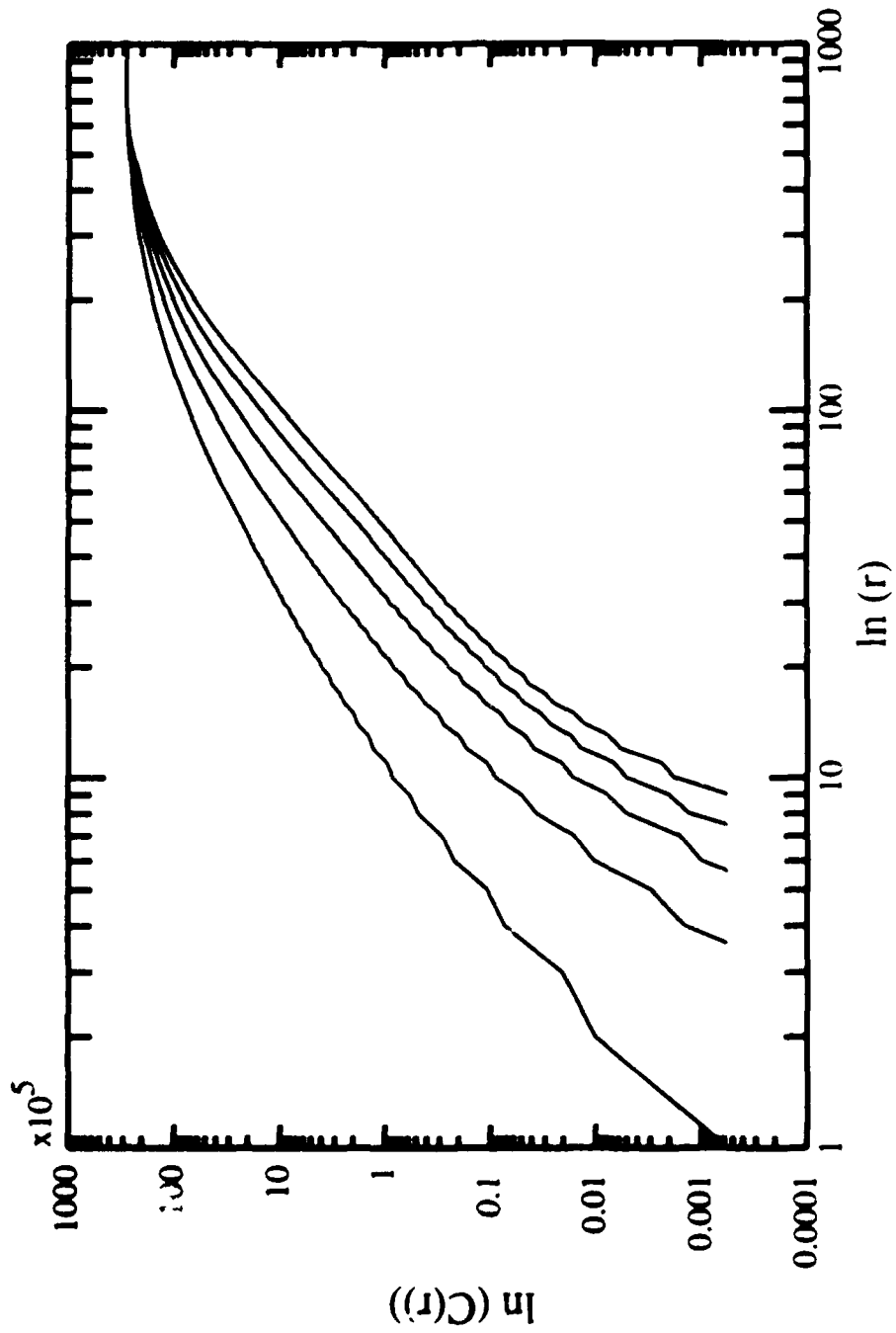


FIGURE 3A

Dimensional analysis for data in figures 36 and 37. Data are plotted left to right for embedding dimension $m = 4, 8, 12, 16, \text{ and } 20$. Number of data points $N = 8,192$.

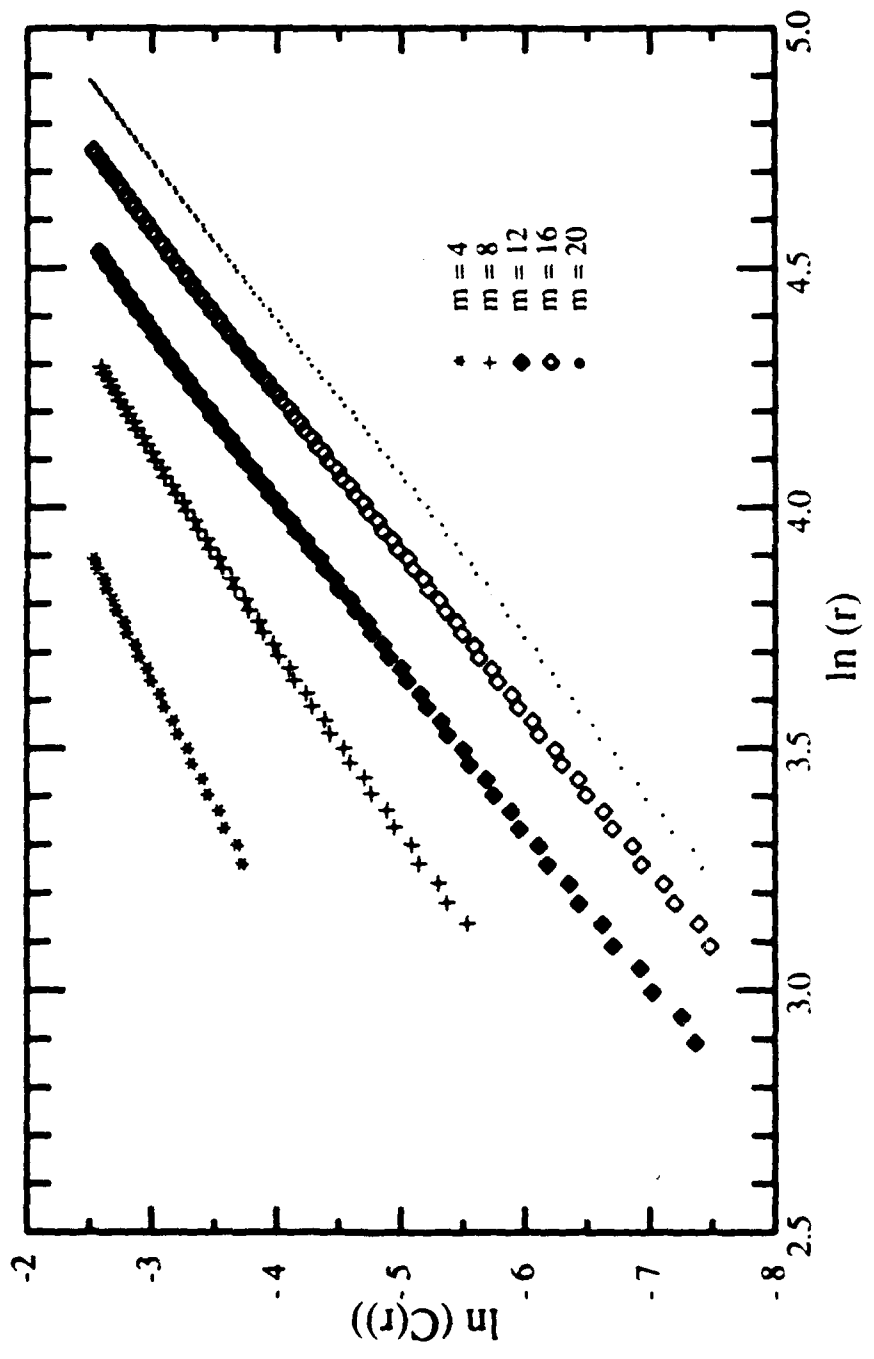


FIGURE 39

Expansion of scaling region in figure 38.

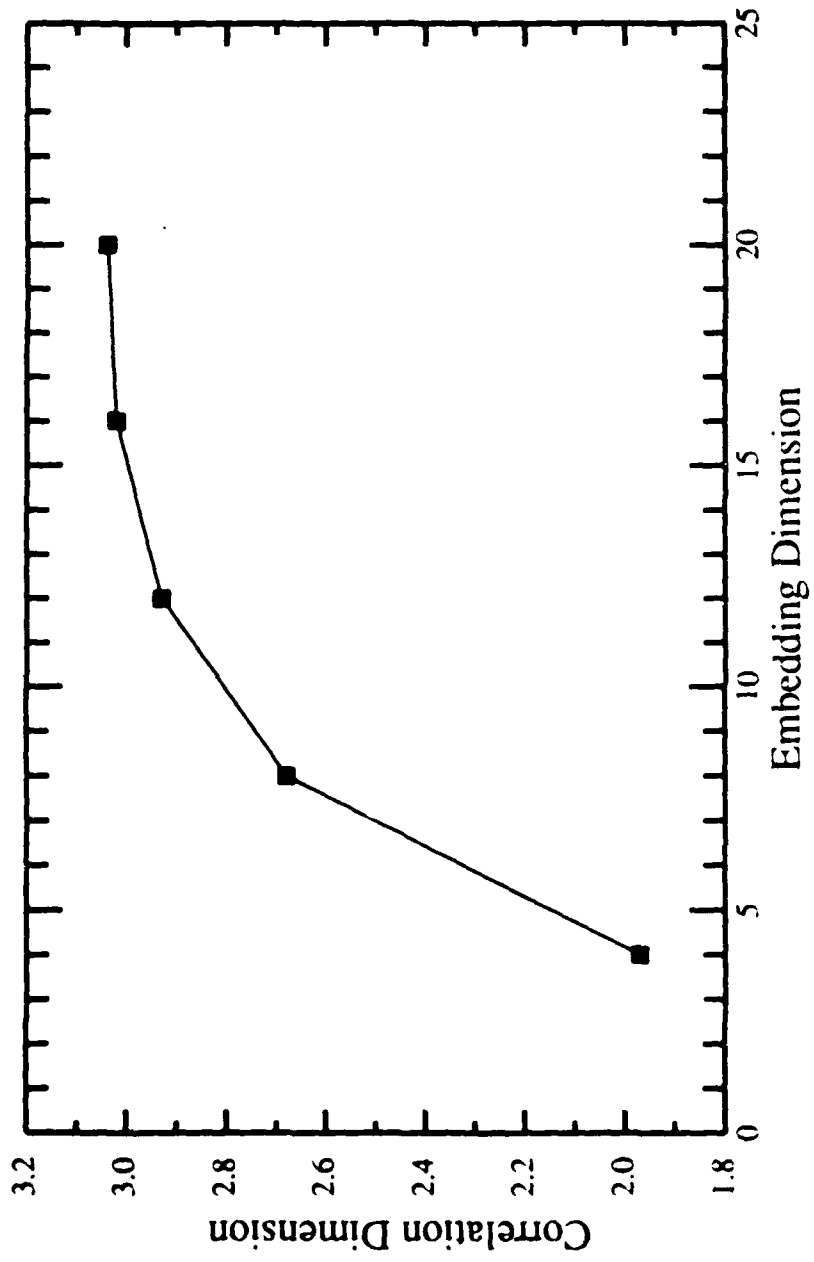


FIGURE 40

Correlation dimension vs. embedding dimension from linear fit to scaling region in figure 39.

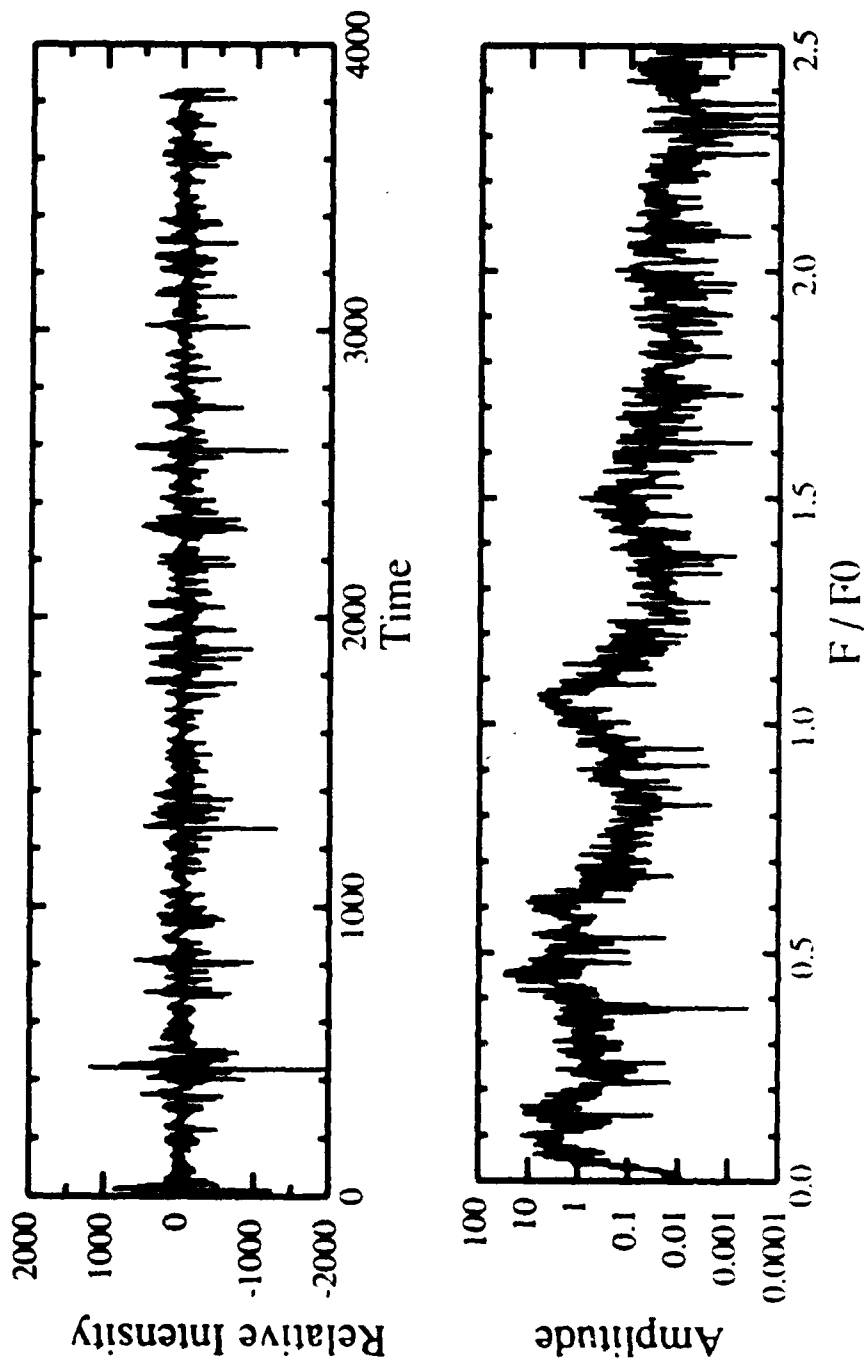


FIGURE 41

Intensity vs. time for the Thom EMI photomultiplier centered at 66 degrees and the He/Ne laser. Bubble size is approximately 90 microns, $f = 24.6$ kHz, and the pressure is unknown.

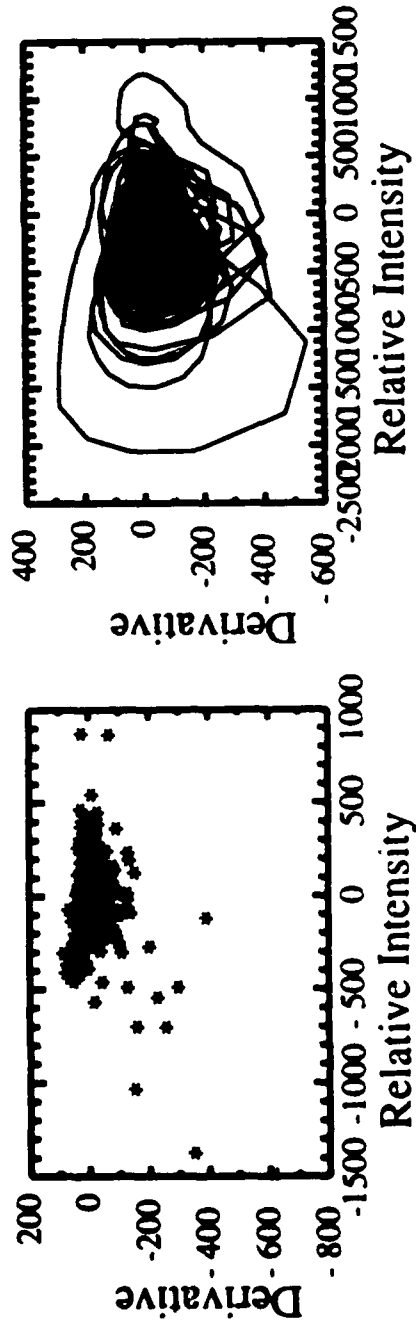
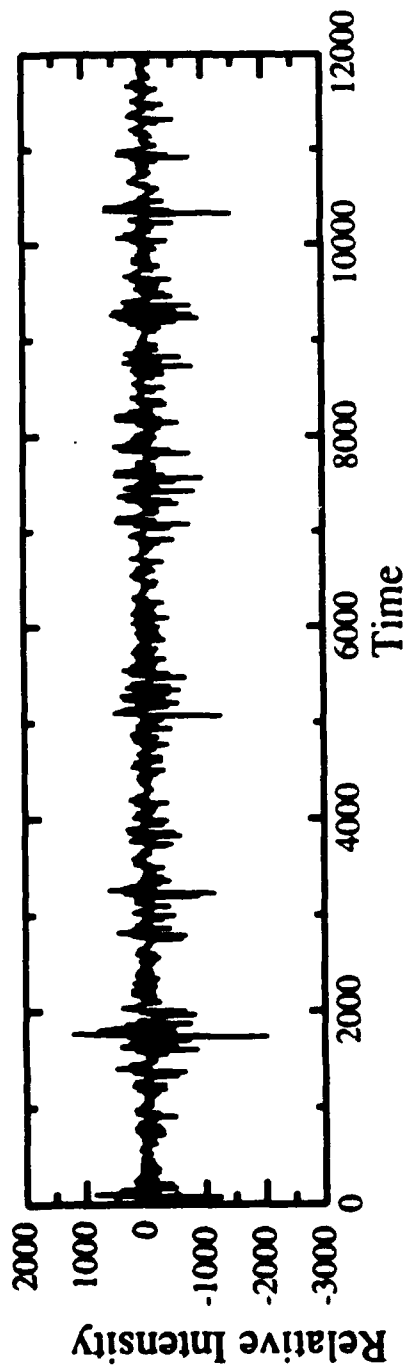


FIGURE 42

Phase-space projection for data from figure 41.

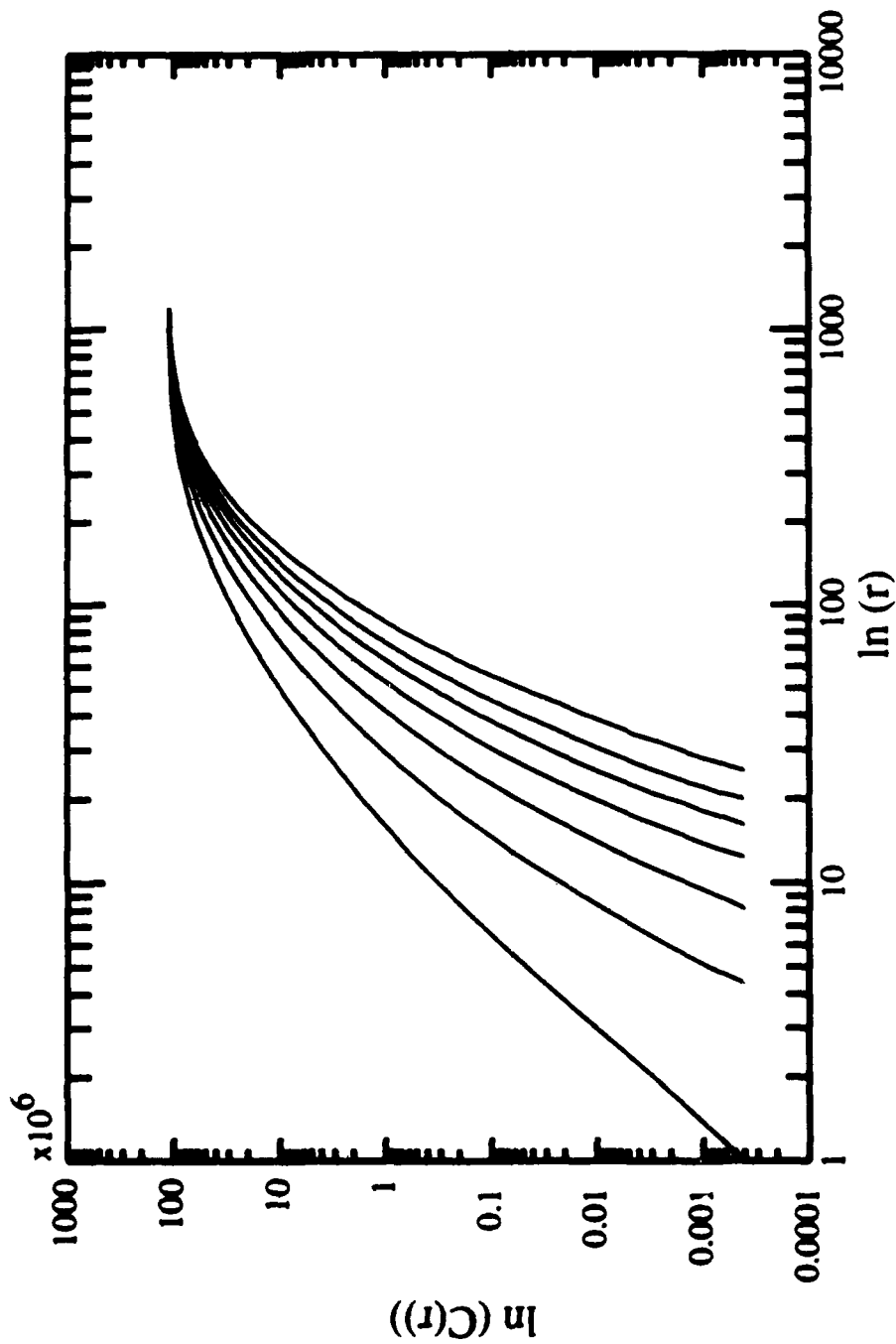


FIGURE 43

Dimensional analysis for data in figures 41 and 42. Data are plotted left to right for embedding dimension $m = 4, 8, 12, 16, 20, 24,$ and 30 . Number of data points $N = 16,000$.

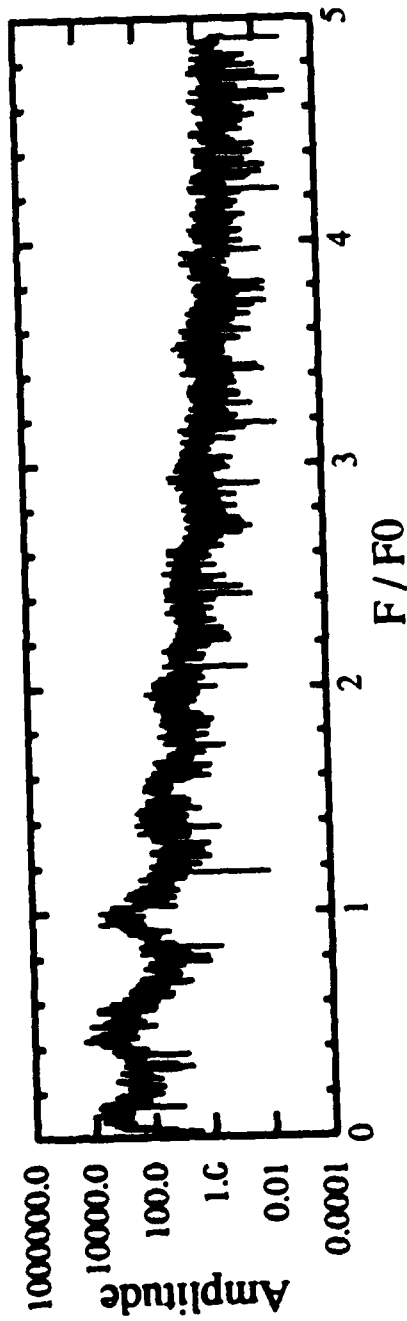
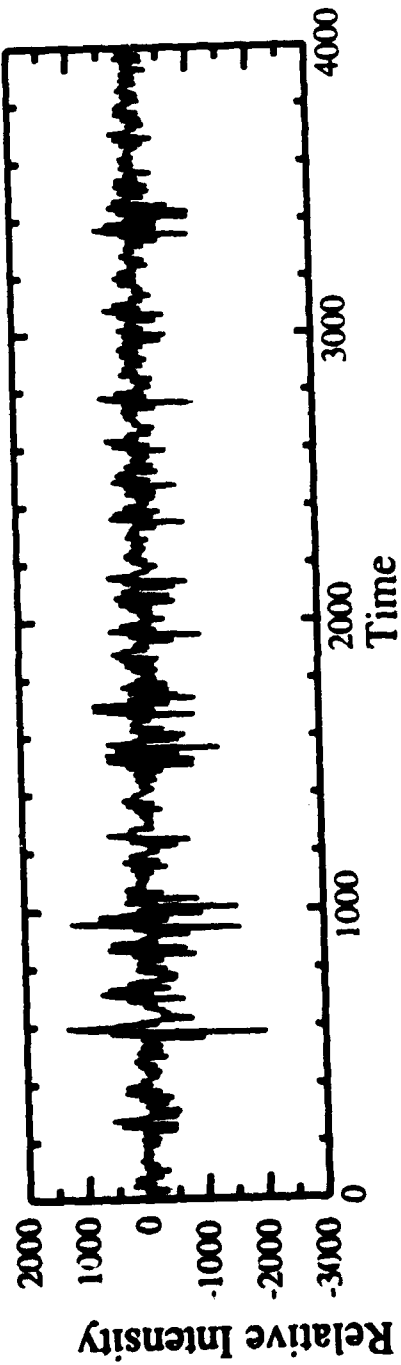


FIGURE 44

Intensity vs. time for the Thorn EMI photomultiplier centered at 66 degrees and the He/Ne laser. Bubble size is approximately 90 microns, $f = 24.6$ kHz, and the pressure is unknown.

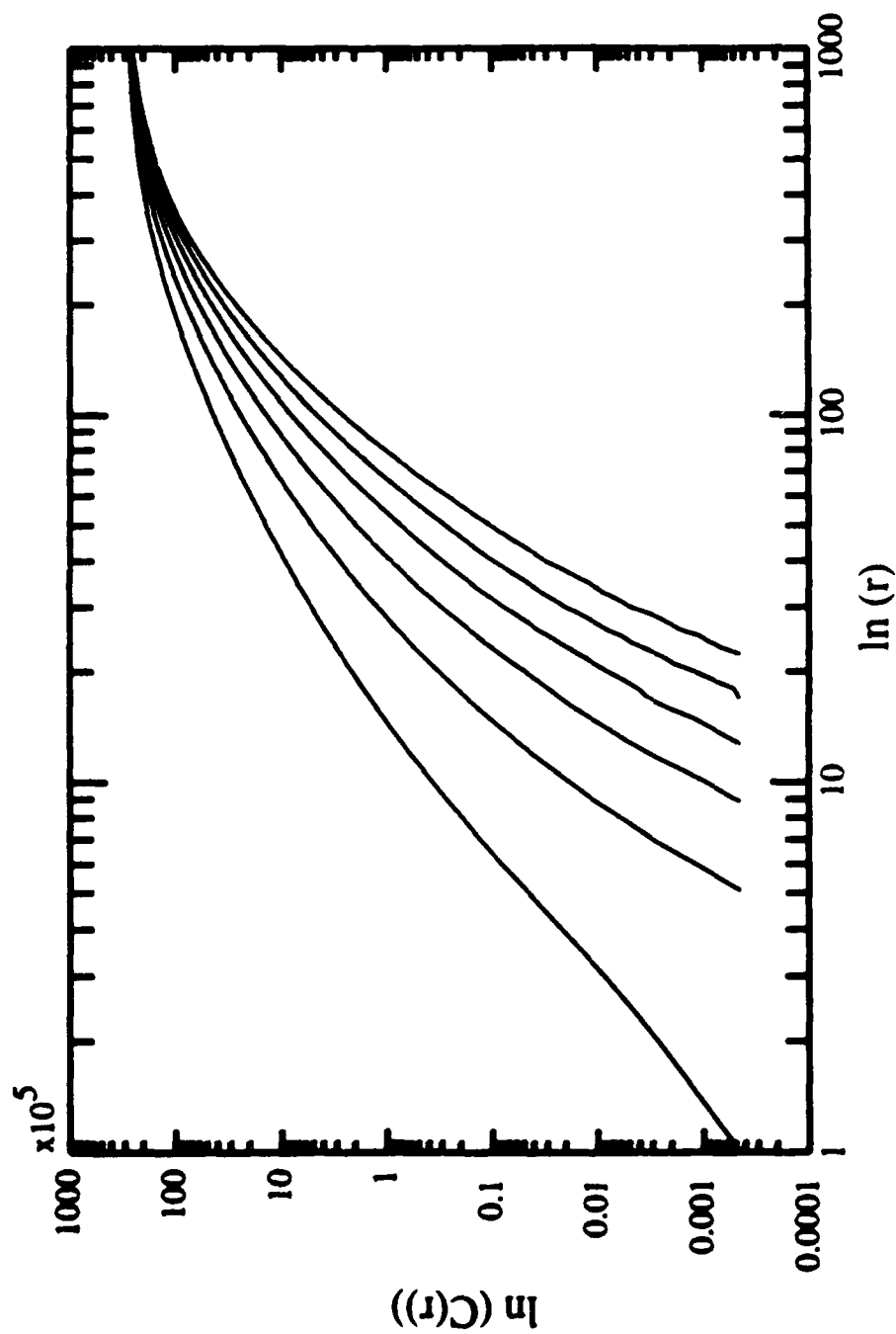


FIGURE 45

Dimensional analysis for data in figure 44. Data are plotted left to right for embedding dimension $m = 4, 8, 12, 16, 20$, and 24. Number of data points $N = 12,000$.

the embedding dimension up to $m = 30$. No scaling region is apparent. From a comparison of the spectra of the data for Fig. 42 with that for Fig. 38 (where $D_2 = 3$), a higher dimension should be expected from Fig. 43, since the motion in Fig. 42 contains more spectral components.

It should be noted that these data sets were not taken with dimension calculations in mind, and they are certainly not optimal. N is relatively small, and t_s is also too small. Theoretically, optimal values of N and t_s are $N = \infty$, and $t_s = \tau$, the period of the driving pressure. Thus it is not necessarily surprising that some of the data should show a null result. Figs. 44 and 45 show a data set, its spectrum, and the dimensional analysis up to embedding dimension $m = 24$. Again, no scaling region appears.

A final phenomenon of interest is the behavior shown in Figs. 46-48. The signal alternates between a relatively smooth (region A, Fig. 47) oscillation and a more violent, irregular motion (region B, Fig. 48). Such bursting, or intermittency [82], has been observed in some other experiments, both numerical and physical [83,84], and is another universal phenomenon associated with driven nonlinear systems. Dynamically, the frequency of the bursting should increase as some parameter (the pressure, for instance) approaches some critical value. The behavior shown is most probably Pomeau-Manneville Type I intermittency, generated by an inverse tangent bifurcation [85], although this is just speculation without more data to analyze.

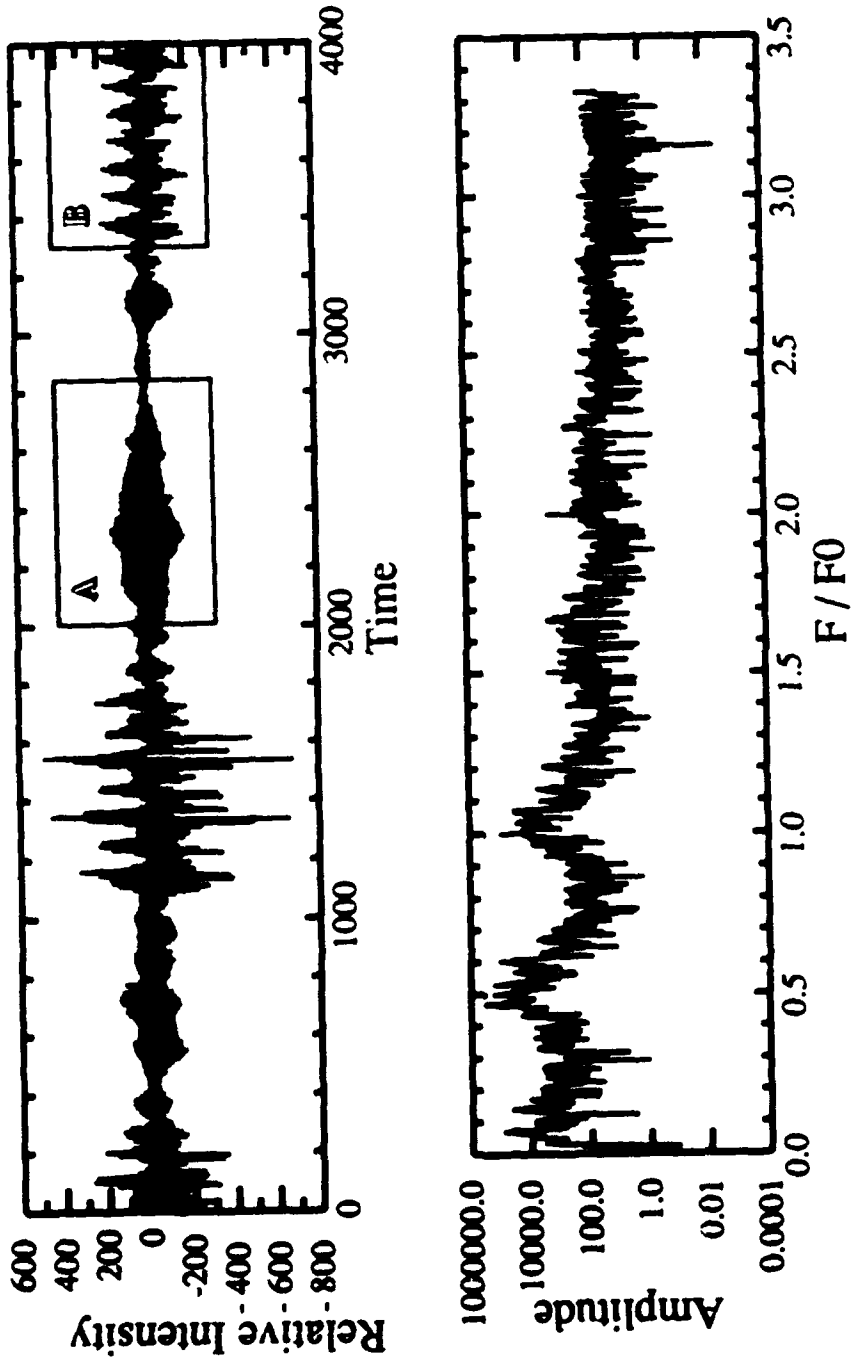


FIGURE 46

Intensity vs. time for the Thorn EMI photomultiplier and the He/Ne laser. Bubble size is approximately 90 microns, $f = 24.6$ kHz, and the pressure is unknown. The boxed regions showing the different types of behavior are blown up and examined in the following two figures.

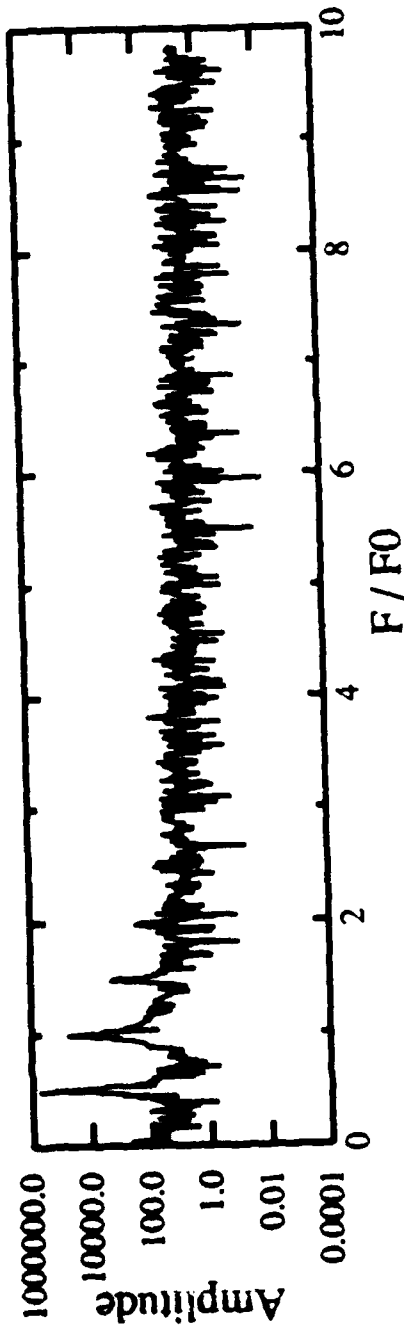
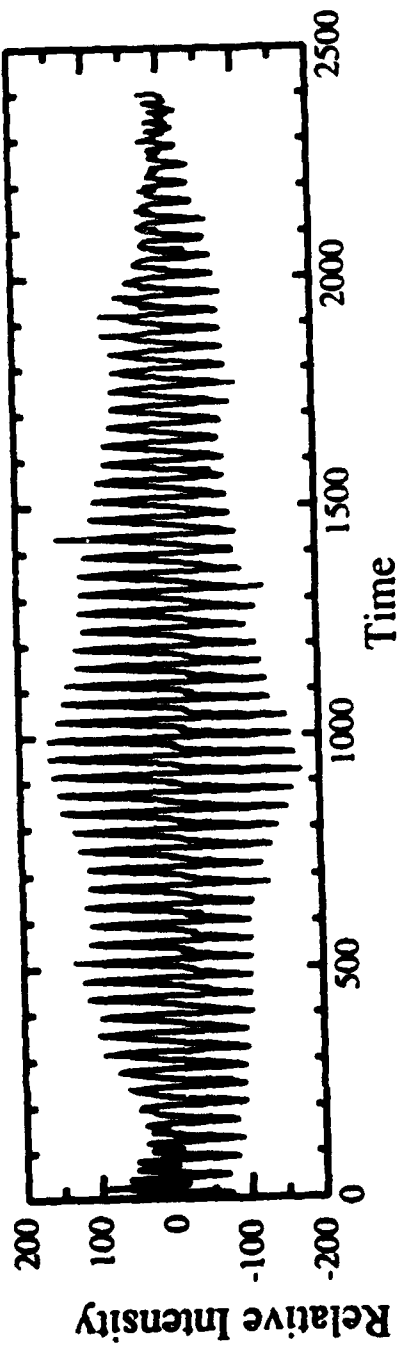


FIGURE 47

Blow-up of region A in figure 46

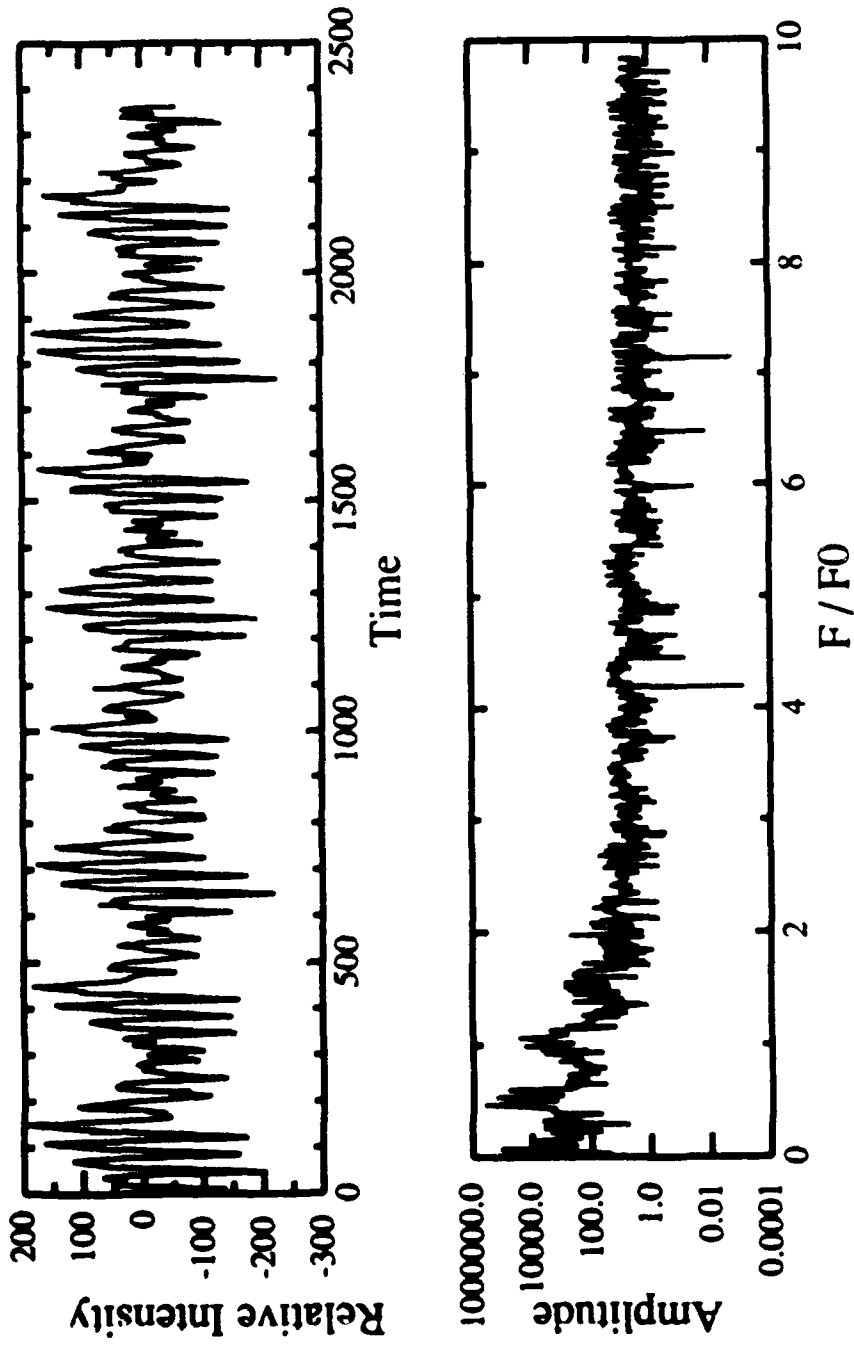


FIGURE 48

Blow-up of region B in figure 46

Chapter IV

Discussion

One of the most striking features of this experiment is the visual appearance of a bubble in a laser beam. Striking in one sense because there is a perhaps sophomoric appeal in being able to discern physical phenomena with the naked eye. Striking in another sense because of the sheer magnitude of the intensity of the scattered light. It is easily visible with the room lights on, and never fails to attract the attention of visitors to the lab, regardless of their scientific interest (if any) in the research. It seemed at the outset a trivial task to detect such copious amounts of light. Such pre-experimental naiveté was soon replaced by three years of frustrating efforts at balancing the trade-off between signal-noise, bandwidth, and ease of calibration.

When, with the third detection system, I finally got all three reasonably well balanced, I was understandably, though perhaps a bit prematurely, proud of the results. In the first blush of excitement, I showed some response curves (Figs. 12-19) to A. Prosperetti, who has struggled with improving the theory of bubble oscillations for almost 20 years. I won't soon forget his words upon seeing the first experimental response data ever collected for a radially oscillating bubble: "Well, that's a bloody mess, isn't it?"

My re-entry was short, and of course the point was well taken: namely, that the data weren't good enough to distinguish between different bubble models. The reasons for this imprecision are largely apparatus related. As already noted, the problems with the

determination of the driving pressure make it difficult to compare the experimental results with theory.

The independent method for determining R_0 for calibration purposes was a rise-time method, and an error due to reaction time and assumptions made to get a drag law easily give rise to a 3 to 5% error in R_0 . However, the fact that the peak response occurred so close to $R_0/R_{res} = 0.5$ lends much credence to the method used. Previous reports of errors as great as 10% [50,54] for a large range of radii were not borne out by the results of this study.

Probably the biggest problem was that of the gain-bandwidth product limitation of the detector. To obtain a bandwidth of ≈ 100 kHz, I had to live with a signal-noise ratio < 1 for small-amplitude, small bubble oscillations. As reported, continuous averaging eliminated the noise to a large extent. However, the presence of bubble dissolution or growth by rectified diffusion could have introduced error in the AC oscillation amplitude as well as the DC component used to determine R_0 .

Nevertheless, I am convinced that the amplitude response difference between theory and experiment, especially near the 2nd harmonic resonance, is real and worth pursuing further with better electronics. Figures 20-29 show clearly that, even when the overall response amplitude is matched, the 2nd harmonic component differs significantly from the theoretical prediction. Absolute and relative phase measurements as a function of R_0/R_{res} could provide more insight into the damping, and future plans call for making such measurements with the aid of a lock-in amplifier.

Somewhat more intriguing are the subharmonic point in Fig. 13, and the subharmonic curves of Figs. 30 and 31. The question is, where do these subharmonic oscillations fit into the resonance scheme? Theoretically, at these amplitudes (see Fig. 1)

there are not yet any subharmonic or ultraharmonic [18] responses in the region of 0.66 or 0.5, and the main resonance does not appear to have leaned over enough for the oscillations to belong to the first period-doubling bifurcation off of the main resonance [71]. Also, there is no large, discrete jump in amplitude, as would be apparent if the pressure perturbation excited the bubble into the main resonance. Shape oscillations are only a remote possibility. From experience, the shape oscillation with a frequency $f/2$ is the first to appear. There is a discrete transition to this type of behavior, much like the jump to the upper branch of the main resonance would exhibit. However, the scattered intensity from the shape oscillation has an amplitude one or two *orders of magnitude* higher than the radial period-one oscillation. Furthermore, it precesses. The visual effect is that of a lighthouse, and is immediately discernable. Videos were made of the oscilloscope trace showing the period-two oscillation appearing and disappearing in a regular fashion, with a definable period of precession over a short enough time. These subharmonic oscillations have a much lower amplitude response, and show none of the symptoms of precession.

The most likely explanation for the behavior in Figs. 30 and 31 is that it is a transient precursor of a subharmonic resonance that will appear (become stable) at higher pressure amplitudes near $R_0/R_{res} \approx 0.66$, namely, the $3/2$ resonance [18]. Roughly speaking, the $3/2$ designation means an oscillation with frequency $1/3$ of the bubble's linear resonance frequency f_0 and $1/2$ of the driving frequency f . In other words, the bubble has three collapses every period T of the driving pressure, and repeats its motion every $2T$. Transient oscillations are governed by the interaction of both the stable (non-resonant, in this case) and unstable (resonant) solutions existing for a given parameter set, and especially by the direction of the unstable manifold associated with the unstable solution, since nearby trajectories in phase space will follow this direction [14]. Eventually, this

unstable manifold becomes the stable manifold of the stable solution, and thus perturbed trajectories eventually settle back into the available stable steady-state motion.

A generic scenario for the time of the transient oscillation for such a threshold-dependent phenomenon is given by $\tau_{tr} \propto (P - P_{th})^{-\alpha}$ [72], where τ_{tr} is the mean transient lifetime, P is, in this case, the instantaneous pressure, P_{th} is the threshold for the stability of the subharmonic resonance, and α is some constant such that $0 < \alpha < 1$. Thus, the mean lifetime of the transient increases as P approaches P_{th} . This occurs because, as P approaches P_{th} , the stable, non-resonant solution becomes more and more weakly stable, whereas the resonant solution approaches stability. At P_{th} the two solutions will, in effect, exchange stability. Mathematically speaking, the absolute value of at least one of the eigenvalues of the linearized Poincaré mapping of the non-resonant solution is approaching unity, while the converse is true for the resonant solution. The stability exchange at $P = P_{th}$ occurs via a simple period-doubling (supercritical flip) bifurcation [14]. These observations also apply to the anomalous point in Fig. 13, though it is less clear in this case which unstable resonance the point belongs to.

An interesting analytical treatment of transient subharmonic solutions for the Rayleigh-Plesset equation of bubble dynamics can be found in Prosperetti [98]. Using the Bogoliubov-Krylov method of averaging [99], he showed that the nature of transients in the region of the first ($f/2$) subharmonic resonance is governed by the stable and unstable singular points in a modified (Amplitude vs. phase of the resonant solution) phase space. The length of the transients and the eventual final solution state were shown to exhibit, in his words, a "sensitive" dependence on initial conditions. A schematic picture of the intertwining of the "domains of attraction" of the different final solutions was presented. It is perhaps unfortunate that these ideas were not pursued further in the context of bubble

oscillations, since it has recently been shown that this intertwining of domains (or "basins", to use the standard nomenclature of nonlinear dynamics) of attraction is a universal feature of all nonlinear dissipative systems possessing multiple stable and unstable solutions [14]. It is precisely this sensitivity to initial conditions which limits the concept of predictability for the final steady-state, since the basin boundaries in the phase space are not smooth curves as Prosperetti indicated, but rather fractals [93]. This implies an uncertainty in the prediction of the steady-state motion which increases exponentially with respect to the finite imprecision in knowledge of the initial conditions [100,101].

This scenario is even further complicated when the effect of rectified diffusion [61], another threshold-dependent phenomenon (whose threshold is slightly exceeded for these parameters), is considered. This results in R_0 being a nonlinearly increasing function of time. Fortunately, the time-scale for rectified diffusion for these pressures and near saturation is relatively long, and an estimate for the growth rate is about $0.05 \mu\text{m/s}$ [61]. As a check for the data in Figs. 30-31, R_0 was measured via the rise-time technique before the pressure was bumped and after the period-2 oscillation had decayed, with no observable difference in R_0 . Thus, the dynamical effects will be small, even though rectified diffusion is a great aid in the experimental procedure, since it allows a more or less passive method of covering a range of values R_0/R_{res} .

Perhaps conspicuous by its absence is the ubiquitous period-doubling (subharmonic) cascade bifurcation culminating in chaos [13,76,77], which has been the paradigm for nonlinear dynamical systems, and has also been observed not only in single bubble numerical models [31], but also in cavitation bubble fields [29,30,48]. One answer is that steady-state phenomena, rather than bifurcation phenomena (which require varying control parameters and involve transient responses), have been emphasized in this

experiment. Period-doubled solutions are observed in Figs. 30, 31, and 32-34, but the latter group contained shape oscillations in the motion, and these observations were made with both P and R_0/R_{res} different for different periodic responses, making the identification of a smooth bifurcation curve impossible.

The other answer is that bifurcation phenomena, even for a single bubble, are going to be very complex, since the simple instabilities leading to period-doubling in a single degree of freedom will be overshadowed by instabilities of the radial shape and decoupling of the internal pressure from the motion of the interface. The decoupling of the pressure will manifest itself as a series of Hopf bifurcations [90], each bifurcation adding a new frequency, and hence a new degree of freedom. One interpretation of the results of such bifurcations is that the bubble will seem to gain one or more "nonlinear resonance frequencies" f_i .

The theoretical evidence for this route to higher dimensionality can be seen in the fact that the modeling of the thermodynamic behavior of the bubble interior (Chapter I) involves a partial differential equation. This makes the system, even ignoring shape oscillations, infinite dimensional by virtue of the spectral theorem [14,82,90,91]. The surface oscillation modes will also appear as Hopf-type bifurcations, but with an extra complication. Since the frequency of the first shape oscillation is $f/2$, its appearance could be phenomenologically mistaken for a simple period-doubling (flip) bifurcation of the radial mode.

Thus, the observation of high dimensional behavior of a single bubble in chapter III is hardly unexpected. The successive addition of new degrees of freedom is similar to the Landau picture of turbulence, whereby the broadband spectrum observed in fluid turbulence was the result of the successive addition of independent degrees of freedom with

their corresponding frequencies [92]. Complicated behavior, according to this view, was the result of a large, perhaps infinite number of degrees of freedom in the system, requiring a doubly-infinite phase space for the description of the state of the system.

Fortunately, one of the great successes of nonlinear dynamical systems theory has been to show that the dynamics of such technically infinite dimensional systems exhibiting complex behavior can be described by a finite (usually small) number of degrees of freedom, contrary to the Landau turbulence scenario. The motion in phase space contracts onto a low dimensional surface, the "center manifold" [14]. Thus, numerical methods such as a Galerkin expansion followed by truncation of the number of expansion modes is guaranteed to yield all physically relevant properties of the true flow. Excellent experimental examples of such "low-dimensional turbulence" can be found in the fluid experiments of Sreenivasan and Meneveau [95], Swinney [96], and Malraison *et al.* [97], as well as the bubble field work of Lauterborn and Holzfuss [33]. For the present experiment, we are assured that the number of surface modes that actually contribute to the dynamics will be small, as will the number of internal pressure modes, because the nonlinear interaction between the modes will prevent the potentially infinite series of Hopf bifurcations from occurring. Although the picture of bifurcations just painted is complex, it is finite and low-dimensional, and therefore tractable.

It is clear, however, that more work needs to be done in the analysis of the complex $I(t)$ motion. An independent method for determining the presence of shape oscillations would greatly aid the analysis. One such method would be to place a second photodetector centered at some angle θ_2 , and then examine the ratio of the two intensities $I(\theta_1) / I(\theta_2)$ in real time. Precessing shape oscillations would be immediately detected. Additionally, if θ_1

and θ_2 were not symmetric with respect to the forward scattering direction, even non-precessing symmetric shape oscillations should be detectable.

In this fashion, the number of modes due to shape oscillations could perhaps be determined, and compared with D_2 obtained from the time series to determine the number of pressure modes active, and thus obtain a useful picture of the full-blown dynamics of single bubbles. Chaotic motion should be unavoidable, since the nonlinear coupling of shape oscillations with the radial mode through surface tension and internal pressure will limit the number of possible independent degrees of freedom, and this mixing is precisely what is needed for the existence of a low-dimensional strange attractor in the phase space.

That being the case, the question naturally arises: "Are the motions depicted in Figs. 34 through 48 chaotic?" Unfortunately, the answer at this stage must be: "I don't know". Two general criteria for chaos are presented here, representing the two easiest measures to calculate for a time series. The appearance of a broadband FFT spectrum is a necessary *but not sufficient* criterion for chaos -- we're batting 1000, so far. A non-integer fractal dimensionality d [93] is, strictly speaking, neither necessary nor sufficient, but merely customary for chaos (one of the most widely studied chaotic attractors, the Lorenz attractor [94], has $d = 2$). The correlation dimension D_2 calculated here is a lower bound on d , and in practice, the two measures are always within 1 or 2% of each other [80]. The only dimension D_2 calculated was $D_2 = 3$, so we are neither helped nor hindered by D_2 in identifying chaotic motion.

There do exist quantitative criteria to categorize and characterize attractors as chaotic [82]. They can be divided into: (a) Metric properties (including the generalized dimensions D_q mentioned in chapter III), which give rise to static, geometric invariants associated with the complex attractor in phase space regardless of its temporal evolution:

and, (b) Dynamical invariants, such as the Kolmogorov entropy and the Lyapunov exponents. I plan to carry out calculations of some of these quantities for bubble oscillations in the near future, to determine whether chaotic motion has been or can be observed in single bubble oscillations.

REFERENCES

1. L. Euler, *Histoire de l'Academie Royale des Sciences et Belles Lettres*, Mem. R. **10**, (Berlin, 1756).
2. Lord Rayleigh, *Phil. Mag.* **34**, 94 (1917).
3. D-Y Hsieh, *J. Basic Engineering* **87D**, 991 (1965).
4. M. S. Plesset, *J. Appl. Mech.* **16**, 277 (1949).
5. B. E. Noltingk and E. A. Neppiras, *Proc. Phys. Soc. B* **63B**, 674 (London, 1950).
6. B. E. Noltingk and E. A. Neppiras, *Proc. Phys. Soc. B* **64B**, 1032 (London, 1951).
7. H. Poritsky, *Proc. 1st U. S. National Congress in Applied Mechanics (A.S.M.E.)* **813**, (1952).
8. R. Hickling and M. S. Plesset, *Phys. Fluids* **7**, 7 (1964).
9. A. Prosperetti, L. A. Crum, K. W. Commander, *J. Acoust. Soc. Am.* **83**, 502 (1988).
10. S. A. Thorpe and P. N. Humphries, *Nature* **283**, 463 (1980).
11. A. Prosperetti, "Bubble dynamics in oceanic ambient noise", *Proceedings of the 1987 NATO Advanced Research Workshop Natural Mechanisms of Surface Generated Noise in the Ocean* (in press).
12. L. A. Crum, S. Daniels, M. Dyson, G. R. ter Haar, and A. J. Walton, *Proc. of Inst. of Acoust. (UK)* **8**, 137 (1986).
13. P. Cvitanovic, *Universality in Chaos* (Adam Hilger, Bristol, 1984).
14. J. M. T. Thompson and H. B. Stewart, *Nonlinear Dynamics and Chaos* (John Wiley and Sons, New York, 1986).
15. G. Mie, *Ann Phys.* **25**, 377 (1908).
16. H. G. Flynn, "Physics of acoustic cavitation in liquids", in *Physical Acoustics*, edited by W. P. Mason (Academic, New York, 1964).
17. R. E. Apfel, *J. Acoust. Soc. Am.* **69**, 1624 (1981).

18. W. Lauterborn, *J. Acoust. Soc. Am.* **59**, 283 (1976).
19. Y. A. Akulichev, *Sov. Phys. Acoust.* **13**, 149 (1967).
20. J. B. Keller and I. Kolodner, *J. Appl. Phys.* **27**, 1152 (1956).
21. A. Prosperetti, *J. Acoust. Soc. Am.* **56**, 878 (1974).
22. J. B. Keller and M. Miksis, *J. Acoust. Soc. Am.* **68**, 628 (1980).
23. R. E. Apfel, *Br. J. Cancer Suppl. V* **45**, 140 (1982).
24. A. Prosperetti, *J. Acoust. Soc. Am.* **61**, 17 (1977).
25. L. A. Crum, *J. Acoust. Soc. Am.* **73**, 116 (1983).
26. L. A. Crum and A. Prosperetti, *J. Acoust. Soc. Am.* **73**, 121 (1983).
27. H. G. Flynn, *J. Acoust. Soc. Am.* **57**, 1379 (1975).
28. R. Hickling, *J. Acoust. Soc. Am.* **35**, 967 (1963).
29. W. Lauterborn, *Appl. Scient. Res.* **38**, 165 (1982).
30. W. Lauterborn and E. Cramer, *Phys. Rev. Lett.* **47**, 1445 (1984).
31. W. Lauterborn and E. Suchla, *Phys. Rev. Lett.* **53**, 2304 (1984).
32. P. Smereka, B. Birnir, and S. Banerjee, *Phys. Fluids* **30**, 3342 (1987).
33. W. Lauterborn and J. Holzfuß, *Phys. Lett.* **115A**, 369 (1986).
34. M. S. Plesset, *J. Appl. Phys.* **25**, 96 (1954).
35. A. Prosperetti, *Q. Appl. Math.* **35**, 339 (1977).
36. A. Prosperetti and G. Seminara, *Phys. Fluids* **21**, 1465 (1978).
37. A. I. Eller and L. A. Crum, *J. Acoust. Soc. Am.* **47**, 762 (1970).
38. A. Francescutto and R. Nabergoj, *Acustica* **41**, 215 (1978).
39. P. Hall and G. Seminara, *J. Fluid Mech.* **101**, 423 (1980).
40. V. Kamath and A. Prosperetti, *J. Acoust. Soc. Am.* (in press).
41. D. F. Gaitan, private communication.

42. W. Lauterborn, *Acustica* **31**, 51 (1974).
43. W. Lauterborn, *Opt. Comm.* **21**, 67 (1977).
44. G. Haussmann, and W. Lauterborn, *Appl. Opt.* **19**, 3529 (1980).
45. W. Lauterborn and A. Vogel, *Ann. Rev. Fluid Mech.* **16**, 223 (1984).
46. W. Hentschel and W. Lauterborn, *Opt. Eng.* **24**, 687 (1985).
47. W. Hentschel, H. Zarschizky, and W. Lauterborn, *Opt. Comm.* **53**, 69 (1985).
48. W. Lauterborn and A. Koch, *Phys. Rev.* **35A**, 1974 (1987).
49. A. Vogel and W. Lauterborn, *Appl. Opt.* **27**, 1869 (1988).
50. G. M. Hansen, *Appl. Opt.* **24**, 3214 (1985).
51. P. L. Marston, *J. Opt. Soc. Am.* **69**, 1205 (1979).
52. D. S. Langley and P. L. Marston, *Appl. Opt.* **23**, 1044 (1984).
53. M. Kerker, *The Scattering of Light and Other Electromagnetic Radiation* (Academic, New York, 1969).
54. G. M. Hansen, "Mie scattering as a technique for the sizing of air bubbles", PhD dissertation, University of Mississippi, Oxford, MS (1983).
55. W. J. Wiscombe, *Appl. Opt.* **19**, 1505 (1980).
56. D. L. Kingsbury and P. L. Marston, *J. Opt. Soc. Am.* **71**, 358 (1981).
57. W. Lauterborn, J. Holzfluss, and A. Koch, "Recent advances in cavitation research at Göttingen University", Proceedings of the 1986 International Symposium on Cavitation, H. Murai, ed., Sendai, Japan (1986).
58. P. L. Marston, private communication
59. M. Strasberg, *J. Acoust. Soc. Am.* **31**, 163 (1959).
60. A. I. Eller, *J. Acoust. Am.* **43**, 170 (1968).
61. L. A. Crum, *J. Acoust. Soc. Am.* **68**, 203 (1980).
62. D. A. Young, "An acoustic levitation technique for the study of nonlinear oscillations of gas bubbles in liquids", MS thesis, University of Mississippi, Oxford, MS (1983).

63. S. D. Horsburgh, proprietary unpublished software package providing menu-driven scientific graphical and numerical analysis for arbitrarily formatted data.
64. H. W. Wyld, *Mathematical Methods for Physics* (Addison-Wesley, Reading, MA, 1976).
65. J. H. Moore, C. C. Davis, M. A. Coplan, *Building Scientific Apparatus* (Addison-Wesley, Reading, MA, 1983).
66. R. K. Gould, *J. Acoust. Soc. Am.* **43**, 1185 (1968).
67. A. I. Eller, *J. Acoust. Soc. Am.* **47**, 1469 (1970).
68. H. Goldstein, *Classical Mechanics* (Addison-Wesley, Reading, MA, 1981).
69. L. A. Crum and A. Prosperetti, *J. Acoust. Soc. Am.* **75**, 1910 (1984).
70. P. M. Morse and K. U. Ingard, *Theoretical Acoustics* (Princeton University Press, Princeton, NJ, 1986).
71. W. L. Lauterborn, "Acoustic turbulence", Proceedings of the 1984 International School of Physics "Enrico Fermi": *Frontiers in Physical Acoustics*, D. Sette, ed. (North-Holland, Amsterdam, 1986).
72. C. Grebogi, E. Ott and J. Yorke, *Phys. Rev. Lett.* **57**, 1284 (1986).
73. P. Grassberger and I. Procaccia, *Phys. Rev. Lett.* **50**, 346 (1983).
74. F. Takens, Springer Lecture Notes in Mathematics 898, *Dynamical Systems and Turbulence* (Springer, Berlin, 1981).
75. N. H. Packard *et al.*, *Phys. Rev. Lett.* **45**, 712 (1980).
76. M. J. Feigenbaum, *J. Stat. Phys.* **19**, 25 (1978).
77. M. J. Feigenbaum, *Phys. Lett.* **74A**, 375 (1979).
78. F. C. Moon, *Chaotic Vibrations* (John Wiley & Sons, New York, 1987).
79. J. Theiler, *Phys. Rev.* **34A**, 2427 (1986).
80. A. Ben-Mizrachi, I. Procaccia, and P. Grassberger, *Phys. Rev.* **29A**, 975 (1984).
81. J. P. Eckmann and I. Procaccia, *Phys. Rev.* **34A**, 659 (1986).
82. H. G. Schuster, *Deterministic Chaos* (VCH, Weinheim, Federal Republic of Germany, 1988).

83. J. Theiler, "Box-assisted correlation", package of routines for computing correlation dimension from a time series, private communication.
84. M. Dubois, M. A. Rubio, and P. Bergé, *Phys. Rev. Lett.* **51**, 1446 (1983).
85. C. Jeffries and J. Pérez, *Phys. Rev.* **26A**, 2117 (1982).
86. Y. Pomeau and P. Manneville, *Comm. Math. Phys.* **74**, 189 (1980).
87. L. A. Crum and J. B. Fowlkes, *Nature* **319**, 52 (1986).
88. C. C. Church, *J. Acoust. Soc. Am.* **83**, 2210 (1988).
89. W. P. Arnott and P. L. Marston, "Backscattering of laser light from freely rising spherical and spheroidal air bubbles in water", to appear in *Ocean Optics IX*, proc. SPIE, (1988).
90. A. J. Lichtenberg and M. A. Lieberman, Springer Series in Applied Mathematical Sciences **38**, *Regular and Stochastic Motion* (Springer, New York, 1983).
91. G. Iooss and D. D. Joseph, *Elementary Stability and Bifurcation Theory* (Springer, New York, 1980).
92. L. D. Landau and E. M. Lifshitz, *Fluid Mechanics* (Pergamon, London, 1959).
93. B. Mandelbrot, *The Fractal Geometry of Nature* (W. H. Freeman, New York, 1983).
94. C. Sparrow, Springer Series in Applied Mathematical Sciences **41**, *The Lorenz Equations: Bifurcations, Chaos, and Strange Attractors* (Springer, New York, 1982).
95. K. R. Sreenivasan and C. Meneveau, *J. Fluid Mech.* **173**, 357 (1986).
96. H. L. Swinney, *Physica* **7D**, 3 (1983).
97. B. Malraison, P. Atten, P. Bergé, and M. Dubois, *J. Phys. Lett.* **44**, L897 (1983).
98. A. Prosperetti, *J. Acoust. Soc. Am.* **57**, 810 (1975).
99. N. N. Bogoliubov and N. M. Krylov, *Introduction to Nonlinear Mechanics* (Princeton University Press, Princeton, 1943).
100. C. Grebogi, E. Ott, and J. Yorke, *Physica* **7D**, 181 (1983).
101. R. G. Holt and I. B. Schwartz, *Phys. Lett.* **105A**, 327 (1984).

December 1988

DISTRIBUTION LIST FOR
NCPA LC.2 1988
TECHNICAL REPORT UNDER CONTRACT N00014-86-K-0134

COPY NO.

1	Chief of Naval Research Office of Naval Research Department of the Navy Arlington, VA 22219 Attn: R. Fitzgerald (Code 1125UA)
2-7	Director Naval Research Laboratory Washington, D.C. 20375 Attn: Library
8	Commander Space and Naval Warfare Systems Command Washington, D.C. 20363-5101 Attn: CAPT. L. Wardle (Code PDW-106-6)
9	Commander David Taylor Naval Ship Research and Development Center Target Physics Branch Bethesda, MD 20084 Attn: S. Schreppler (Code 1965)
10	Superintendent Naval Postgraduate School Department of Physics Monterey, CA 93940 Attn: Steve Garrett
11-22	Commanding Officer and Director Defense Technical Information Center Bldg. 5, Cameron Station 5010 Duke Street Alexandria, VA 22314
23-33	Dr. L.A. Crum Associate Director for Basic Research National Center for Physical Acoustics University, MS 38677
34-41	Dr. R. Glynn Holt National Center for Physical Acoustics University, MS 38677
42	Jane E. Crum Senior Marketing Specialist National Center for Physical Acoustics University, MS 38677